FACULTY OF ENGINEERING
AND ARCHITECTURE

Patient-Specific Computational Fluid Dynamics Models of the Human Left Heart Using the Chimera Technique

Federico Canè

Doctoral dissertation submitted to obtain the academic degree of
Doctor of Biomedical Engineering

Supervisors
Prof. Patrick Segers, PhD* - Prof. Joris Degroote, PhD**

* Department of Electronics and Information Systems
Faculty of Engineering and Architecture, Ghent University
** Department of Electromechanical, Systems and Metal Engineering
Faculty of Engineering and Architecture, Ghent University

April 2021

GHENT
UNIVERSITY

ISBN 978-94-6355-480-0
NUR 954
Wettelijk depot: D/2021/10.500/28

Members of the Examination Board

Chair

Honorary Prof. Ronny Verhoeven, PhD, Ghent University

Other members entitled to vote

Prof. Tom De Mulder, PhD, Ghent University
Prof. Charlotte Debbaut, PhD, Ghent University
Prof. Franck Nicoud, PhD, Université de Montpellier, France
Prof. Alberto Redaelli, PhD, Politecnico di Milano, Italy

Supervisors

Prof. Patrick Segers, PhD, Ghent University
Prof. Joris Degroote, PhD, Ghent University

Here is my secret,
a very simple secret:
it is only with the heart
that one can see rightly;
what is essential
is invisible to the eye.

Antoine de Saint-Exupéry
The Little Prince

Preface

It feels really good to see the finish line and think about how everything started. The evening of the 30^{th} of April 2015 (the day after my graduation) I was yelling at my internet connection for being incredibly slow in sending the documents required to start a PhD at the BioMMeda group in Ghent. Of course, I was sending the documents the last available hour before the deadline. Now I have learned that yelling doesn't help to solve the problems and that submitting important documents few days before the deadline helps to prevent stressful situations. The recipient of that email was, of course, Prof. Patrick Segers, and the person that seeded in me the idea of starting a PhD was Prof. Alberto Redaelli, the supervisor of my master thesis project. I have met Patrick a few months later in Milan when he assured me that he would have hired me for the PhD position that I applied for or another one, for which I sponsored a talented close colleague of mine. Guess who?

First of all, a big thanks go to my supervisors, Patrick and Joris, that guided me towards this important goal. Patrick supported me in steering the rudder over unpaved paths without losing sight of the final goal, keeping always an optimistic mindset, but also being honest in difficult times to help my growth. I appreciated your efficient and educative feedback on papers, posters, presentations. I would be glad if I would have developed even a small fraction of your abilities in producing high-quality scientific materials. I am really glad that Joris joined the supervisor's team. Fluent errors were more clear and less scary when approached during our side-by-side brainstorming meetings. You are the best human encyclopedia on numerical methods that I have ever met and the authentic proof that every problem can be solved with logical thinking. Thank you for not judging my stupid questions and for helping me in training my problem-solving skills. The only regret that I have is that you were not part of the supervisor team from the beginning. Thank you to Gianluca and Benedict for teaching me the potential of PyFormex, which at first glance resembled a mixture between Sanskrit and Farsi, and to all the people at FEops that enriched my internship with pleasant coffee breaks. Special thanks to Prof. Redaelli (and the organizers) for the coordination of the MUSICARE consortium that allowed me to meet a lot of interesting

people, to spend great time during the summer school, and rediscover my roots at the Biomechs group during my secondment in Milan. Thank you to all the partners of the MUSICARE project for their valuable suggestions, and the members of the jury for reviewing my thesis and providing interesting inputs and questions.

Many thanks to Jurgen and Saskia for solving administrative and technical problems, to all my colleagues and friends at the BioMMeda, Medisip, and Joris' groups that made this journey more enjoyable even in the darker days. From the old guard, I would like to thank especially Danilo, Alessandra, Nic, and Daime for the amazing dinners. Matthias, Annette, and Viviana for the unforgettable american hikes, for the Gentenaar boat trip, the brunch, and the everyday useful hints. Hicham, Daniela, Giorgia for the italian chats. Carlos for being one of the few honest Juventus supporter. Shengda for inviting us to the celebration of the Chinese new year. Lise for believing that I was not the mole during the team-building, and Sarah for being patient while I was still using the drawer in your office. For the good atmosphere in the office, I am pleased to thank the good giant Mathias (the belgian bike tour is still in my to-do list), the always-smiling and never-worried Tim, and the loud Eduardo and Dariel. Thanks for the 'Persian' lessons to the Iranian gang (Ghazal, Mohamed, Samaneh, Hooman), and Mariele and Amith to have helped me with my last relocation in Gent. Thank you to for the wonderful games to all the FC Campus players. We won the minor league cup and were really close to win the top-teams one! Special thanks goes to Alvaro for pleasing my eyes with wonderful football dribblings and for leading us in most of our wins. Thank you to the mooi dutch-learning fellowship composed over the years by Vish, Jacky, Joseka, Bart, Nuno, Maria and for other highlights that I will always remember. Last but definitely not least, Amith, thanks for everything, but more importantly for being a real friend. I am glad that the extra-year experience in Ghent allowed me to meet you.

Un grazie di cuore a Lorenzo, Annalu e Gabriella per averci fatto sentire a casa anche in Belgio. A Luca e Mattia per esserci sempre stati, in tutto e per tutto nonostante la lontananza. A Welo e Isa per avermi accolto come un figlio. Alla Zia Franchina e allo Zio Giorgio che mi hanno supportato da lassù con preghiere e i versi alla Tarana, insieme ai nonni. Agli/alle zii/zie, cugini/cugine, parenti, amici di scuola/di una vita. Grazie ad Emi e Gio per la vostra gentilezza e per tutto. Un grazie speciale alla Mamma al Babbo che mi amano più di nient'altro al mondo, per i consigli, e per spingermi a dare sempre il meglio. Infine, grazie a Viviana per essermi stata accanto, per avermi dimostrato cos'è l'amore e per aver sempre creduto in me.

Federico, April 2021

Table of contents

List of Figures

List of Tables

Abbreviations and symbols

The following list summarizes the most commonly used abbreviations and symbols in this thesis.

Abbreviations

3D	Three Dimensional
4D	Four Dimensional
AL	Anterior Leaflet
ALE	Arbitrary Lagrangian-Eulerian
CFD	Computational Fluid Dynamics
CPU	Central Processing Unit
CVD	Cardiovascular Disease
CVS	Cardiovascular System
FDA	Food & Drug Administration
FSI	Fluid Structure Interaction
IBM	Immersed Boundary Method
LV	Left Ventricle
MV	Mitral Valve
PDE	Partial Differential Equation
PL	Posterior Leaflet
UDF	User-Defined Function

Symbols

μ	Dynamic Viscosity	[kg/m/s]
$\overrightarrow{v}$	Velocity Vector	[m/s]
ρ	Density	[kg/m^3]
EL	Energy Loss	[J]
HR	Heart Rate	[1/min]
P	Pressure	[Pa]
P	Residence Time	[s]

Q	Volumetric Flow rate	[m^3/s]
Re	Reynolds number	[-]
SJ	Scaled Jacobian	[-]
SK	Skewnewss	[-]
SV	Stroke Volume	[ml]
v	Velocity Magnitude	[m/s]
WSS	Wall Shear Stress	[Pa]
CPs	Control Points	

Summary

Introduction

Cardiovascular diseases are the leading cause of death worldwide. They often lead to slow and subtle changes in the blood flow in the heart that, if left untreated, can be the start of a chronic pathological condition. The current clinical standard for the detection of cardiac pathology is medical imaging, but the available modalities lack the necessary spatial and temporal resolution to fully analyze the small-scale details of the flow patterns in the ventricles. The integration of medical images with Computational Fluid Dynamics (CFD) allows to compensate for the limited temporal and spatial resolution of medical images, and opens the way to patient-specific CFD modeling of the blood flow in the heart. This method offers the possibility to (i) calculate different relevant flow-related variables in (ii) a predetermined 4D (time + space) region of interest with (iii) the possibility to test different conditions in a virtual environment (parametric study).

First of all, the technique could aid the earlier detection of altered flow conditions which, without intervention, often result in a chronic pathological condition (heart failure, pulmonary hypertension, aortic and cerebral aneurysms, aortic dissection, heart valve pathologies). In addition, the method is extremely suitable for comparing the conditions before and after an intervention, for example to quantitatively evaluate the benefits of surgical treatments or therapies. In this way, a tool is obtained that allows to simulate the outcome of various available surgical procedures and to assist clinicians in the delicate selection of the most appropriate therapy. However, such a clinical use of patient-specific CFD modeling is not yet readily feasible, and requires a level of development of the technique not yet achieved for applications specifically focusing on the flow in the heart chambers. Flow calculations in the heart are intrinsically subject to highly complex technical challenges caused by, among others, the great movement of the endocardium (the inner wall of the heart), the trabecular endocardial surface of the ventricles, the kinematics of the heart valves and the transition-to-turbulent flow regime.

The work in this PhD dissertation was performed within the context of the Horizon-2020 MUltiSectoral Integrative approaches to CArdiac caRE (MUSICARE) program, within the work package n.2, aimed to develop image-processing tools with three aims: integrating different information from multi-modal imaging; creating tools for the real time 3D reconstruction of cardiac structures; developing image-based models for patient-specific prediction of the biomechanical effects of different procedures (http://www.musicare-2020.eu). Specifically, this research focused on the development of a patient-specific CFD model of the Left Ventricle (LV) with the aim to propose flow-derived biomarkers useful for the early detection of cardiac pathologies (project number 642458).

This PhD dissertation consists of three main parts. Part I provides the basic knowledge needed to comprehend the context of this dissertation, both from a clinical and a computational perspective. The challenges related to the patient-specific CFD modeling of the LV are addressed on the basis of a literature overview. Part II forms the essence of this dissertation: it presents the developed workflow, starting from the patient-specific mesh generation until the definition of the CFD set-up, successively used to evaluate the effects induced by torsion and the mitral valve on the intra-ventricular flow. Part III summarizes an overview of the main findings and provides suggestions for further developments.

Part I - Background

The left ventricle: anatomy, physiology and pathophysiology

This chapter depicts the anatomical components of the left heart that interplay to maintain the intra-ventricular flow dynamics, focusing mainly on the Left Ventricle (LV). Successively, the events that occur in the LV during the cardiac cycle are described, followed by a brief section on the developed physiological intra-ventricular flow patterns, and on functional cardiac indices. Finally, the most common cardiac pathologies are briefly addressed, highlighting the impact on the LV fluid dynamics and the LV torsional motion.

Numerical methods for cardiac CFD applications

To provide some background on computational fluid dynamics, this chapter begins with a brief summary of the fundamental equations that govern a typical CFD simulation. Successively, a description of the main numerical approaches to handle mesh motion is provided, highlighting the working principles, the different implementations, the advantages and the disadvantages. Subsequently, a literature review is given on patient-specific CFD modeling of the left heart, focusing on the specific challenges associated with this application: how to impose the LV endocardial movement, the incorporation

of the mitral valve and annulus, the trabeculae carnae, the regimen of the flow (transition-to-turbulent) and the rheological model of blood. Particular attention is given to the patient-specific CFD model of the LV by Bavo et al. ([1], [2]), which was developed within our research group and whose limitations define the starting point of the conducted study.

Part II - CFD model of the contracting LV using the Chimera technique: impact of torsion on intraventricular hemodynamics

Patient-specific boundary layer meshes of the 4D LV endocardium

The main limitation of the model developed by Bavo et al. [1], [2], based on the Arbitrary Lagrangian-Eulerian (ALE) approach, is that the CFD simulations were limited to one cardiac cycle or even the diastolic phase, due to excessive mesh distortion. To solve this problem, we developed a semi-automatic meshing tool to build high quality 4D structured meshes of the LV endocardium starting from 4D segmented surfaces. The 4D boundary layer meshes with 1-to-1 vertex correspondence are then provided as input to a CFD solver to simulate intraventricular hemodynamics, as component grid embedded in a Cartesian one (Chimera technique). The meshing tool relies on isoparametric transformations to project the desired meshing patch on the 4D segmented LV surfaces. After describing the steps performed by the meshing tool, it is applied to three datasets obtained with the three most common imaging modalities (MRI, CT, US) to evaluate the accuracy and the efficiency.

The accuracy can be tuned by varying the number of control points to project onto the segmented surfaces, whereas the number of mesh elements can be increased after the mesh generation by subdividing the 4D meshes. In our implementation, the computational time did not depend on the number of mesh elements but on the number of control points that define the isoparametric transformations.

This algorithm allowed us to generate high-quality 4D structured meshes with a maximum Skewness of 0.9 and a minimum Scaled Jacobian of 0.25 and 0.02 for the surface and boundary layer meshes, respectively. Furthermore, it includes a temporal interpolation tool of the 4D meshes, that allows the user to choose both the number of intermediate configurations and the type of spline (Natural or Bezier) to fulfill the temporal resolution requirements of a CFD calculation.

Influence of torsion on intraventricular hemodynamics in a patient-specific CFD model of the LV based on the Chimera technique

In this chapter, we describe a new workflow based on the Chimera technique with the aim to avoid the negative volume errors induced by excessive mesh

distortion using the ALE approach. The Chimera (or overset mesh) technique, rarely adopted in biomedical CFD models, is particularly suited to handle cases that involve large and impulsive mesh motion, and therefore seems most appropriate for the study of intraventricular hemodynamics. In this study, we showcase the method to investigate the impact of the LV torsion on the intra-ventricular hemodynamics, within a patient-specific CFD model.

The comparison of the three CFD cases with no, physiological (13°) and exaggerated torsion (26°) relied on the assessment of velocity, vorticity, wall shear stress (WSS), energy loss, and residence time of particles released from the inlet. Six cardiac cycles were simulated to minimize the transitional effects. The energy loss and the residence time were evaluated during the 5^{th} and 6^{th} cycle, whereas the remaining variables were compared at the end systole of the 6^{th} cycle, when the maximal difference in the torsional angle occurs.

The new workflow based on the semi-automatic meshing algorithm and the Chimera technique allowed to successfully implement the large deformation of the LV endocardium without resulting in an excessively distorted mesh. We observed a slight cycle-to-cycle variation that was still present after six cycles, probably related to the high dynamicity of the case. The impact of torsion was marginal on velocity, vorticity, WSS, and null on energy loss. We found a dual effect of torsion on residence time: on the one hand, torsion decreased the direct flow (i.e. particles ejected in the first beat); on the other hand, supra-physiological torsion enhanced the motility of the particles residing in the LV after two beats. Even though the study is limited by the absence of the mitral valve, the papillary muscles, and the trabeculae in the simulations, these results suggest that physiological levels of torsion have marginal impact on intraventricular hemodynamics and can be discarded in CFD models. However, given the crucial impact of the Mitral Valve (MV) on the LV hemodynamics, torsion is best investigated in a model that also includes the mitral valve.

A CFD study on the interplay of torsion and vortex guidance by the mitral valve on LV wash-out

It is well known that the mitral valve has a large impact on intraventricular flow dynamics. This chapter therefore builds on the previous chapter and describes the implementation of a patient-inspired MV model into the previously defined patient-specific CFD model of the LV, again making use of the Chimera technique to handle mesh motion. The patient-inspired MV model is based on MRI data segmented at the diastolic A-peak and the kinematics at other time instants are defined by assigning specific rotational angle profiles to four different parts composing the MV mesh (anterior and

posterior leaflets, two commissures). The impact of torsional motion on the LV hemodynamics was assessed comparing a case with and without physiological torsion, again simulating six cardiac cycles. The velocity, vorticity, and WSS were evaluated at the E-peak, A-peak and end systole of the 6^{th} cycle, whereas the energy loss and the residence time were calculated during the 5^{th} and the 6^{th} cardiac cycles. Furthermore, we evaluated the influence of the MV on the LV fluid dynamics by comparing the physiological torsion case with and without the MV, focusing on the diastolic patterns and on the apical washout.

We now observed important cycle-to-cycle variations after six cardiac cycles in all the simulated cases. Torsion marginally affected velocity, vorticity and WSS, whereas it increased the energy loss by +14%. Torsion positively impacted the direct flow (i.e. the particles ejected within the first beat, +9.8%), and had a marginal effect on the number of particles ejected within two beats (+2%). At the same time, torsion decreased the motility of the particles residing in the LV chamber after two beats. Overall, these results obtained in a model that includes the mitral valve indicate a role of torsion on intraventricular hemodynamics that is considerable. We therefore recommend to include torsion in patient-specific CFD models especially when focusing on predisposition to stasis (residence time) and altered energetic conditions (energy loss).

The presence of the mitral valve increased the magnitude of the velocity and vorticity peak, as a consequence of a more pronounced narrowing of the mitral orifice area. Moreover, the formation of the vortex ring occurred at the free edge of the valve instead of the annulus. Lastly, the valve had a favorable effect on the direct flow (+23.5%), and on the particles ejected in two beats (+17.3%). It is concluded that the mitral valve facilitates the penetration of the jet and the vortical ring towards the apex, promoting the apical washout.

Part III - Conclusions

Conclusions

We successfully developed a workflow to set up patient-specific CFD simulations for the study of intraventricular flow dynamics, and applied the workflow to quantify the role of torsion on intraventricular hemodynamics. Torsion was significant only in a model that also incorporated the mitral valve, and we found effects that are important enough to recommend to consider torsion when studying intraventricular flow dynamics, particularly when studying blood stasis.

Future developments should focus on the meshing tool that is best directly applied to medical images and furtherly automated, whereas the Chimera

technique should be further investigated (in direct comparison with the ALE approach) and the compatibility with the CFD solver should be improved.

Samenvatting

Inleiding

Hart- en vaatziekten vormen wereldwijd de belangrijkste doodsoorzaak. Ze leiden vaak tot langzame en subtiele veranderingen van de bloedstroming in het hart die, indien onbehandeld, het begin kunnen vormen van een chronische pathologische aandoening. De huidige klinische standaard voor de detectie van hartpathologie is medische beeldvorming, maar de beschikbare modaliteiten missen de nodige ruimtelijke en temporele resolutie om de kleinschalige details van de stromingspatronen in de hartkamer volledig te kunnen analyseren. De integratie van medische beelden met numerieke stromingsmechanica (Computational Fluid Dynamics of CFD) laat toe om de beperkte temporele en ruimtelijke resolutie van medische beelden te compenseren, en opent de weg naar patiënt-specifieke CFD-modellering van de bloedstroming in het hart. Deze werkwijze biedt de mogelijkheid om (i) verschillende relevante stromings-gerelateerde variabelen te berekenen in (ii) een vooropgesteld 4D (tijd + ruimte) interessegebied met (iii) de mogelijkheid om verschillende condities te testen in een virtuele omgeving (parametrische studie).

Patiënt-specifieke CFD-modellering kan meerwaarde genereren voor verschillende klinische toepassingen. Vooreerst laat de techniek toe om de stromingsomstandigheden te onderzoeken die, zonder tussenkomst, vaak resulteren in een chronische pathologische aandoening (hartfalen, pulmonale hypertensie, aorta- en cerebrale aneurysma's, aortadissectie, hartklep pathologieën) wat kan helpen bij een vroegere detectie van de pathologie. Daarnaast is de methode uitermate geschikt voor de vergelijking van de condities voor en na een interventie, om bijvoorbeeld de voordelen van chirurgische behandelingen of therapieën kwantitatief te evalueren. Op die manier wordt een hulpmiddel verkregen dat toelaat om de uitkomst van verschillende beschikbare chirurgische procedures te simuleren, en de clinici te helpen bij de delicate keuze van de meest geschikte therapie. Een dergelijk klinisch gebruik van patiënt-specifieke CFD-modellering is echter nog niet meteen haalbaar, en vereist een niveau van ontwikkeling van de techniek dat nog

niet is bereikt voor toepassingen die specifiek focussen op de stroming in de hartkamers. Stromingsberekeningen in het hart zijn intrinsiek onderhevig aan zeer complexe technische uitdagingen veroorzaakt door , o.a. de grote beweging van het endocardium (de binnenwand van het hart), het trabeculaire endocardiale oppervlak van de ventrikels, de kinematica van de hartkleppen en het overgangs-naar-turbulente stromingsregime.

Het onderzoek dat aan de basis ligt van deze doctoraatsthesis werd uitgevoerd binnen het Horizon-2020 MUltiSectoral Integrative approaches to CArdiac caRE (MUSICARE) programma, en meer bepaald binnen het werkpakket nr. 2, gericht op het ontwikkelen van beeldverwerkingshulpmiddelen met drie doelstellingen: het integreren van verschillende informatiebronnen uit multimodale beeldvorming; het creëren van hulpmiddelen voor de real-time 3D-reconstructie van hartstructuren; het ontwikkelen van beeld-gebaseerde modellen voor patiënt-specifieke voorspelling van de biomechanische effecten van verschillende procedures (http://www.musicare-2020.eu). Specifiek richtte dit onderzoek zich op de ontwikkeling van een patiënt-specifiek CFD-model van het linkerventrikel (LV) met als doel om stromings-gerelateerde biomerkers voor te stellen die bruikbaar zijn bij de vroege detectie van cardiale pathologie (projectnummer 642458).

Dit proefschrift bestaat uit drie grote onderdelen. Deel I verschaft de basiskennis die nodig is om de context van dit proefschrift te begrijpen, zowel vanuit een klinisch perspectief als vanuit de numerieke stromingsmechanica. De uitdagingen verbonden aan patiënt-specifieke CFD-modellering van het LV worden geschetst aan de hand van een literatuuroverzicht. Deel II bevat de essentie van dit proefschrift: de ontwikkelde workflow wordt voorgesteld, vanaf de creatie van een patiënt-specifiek (bewegend) rekenrooster tot het opzetten van het CFD probleem. Als toepassing wordt onderzocht welk effect de aanwezigheid van de mitralisklep heeft op de stroming in het linker ventrikel, evenals het effect van een torsiebeweging van de hartkamer op de stroming (en afgeleide parameters). Deel III geeft een kort overzicht van de belangrijkste bevindingen, samen met een aantal suggesties voor verdere ontwikkelingen.

Deel I – Achtergrond

Het linkerventrikel: anatomie, fysiologie en pathofysiologie

Dit hoofdstuk bespreekt beknopt de anatomie, fysiologie en pathofysiologie van het linkerventrikel met aandacht voor de anatomische componenten die relevant zijn voor de intra-ventriculaire stromingsdynamiek. Vervolgens worden de gebeurtenissen beschreven die optreden in het LV tijdens de hartcyclus met een focus op de ontwikkelde fysiologische intra-ventriculaire

stromingspatronen, en worden kort functionele cardiale indices toegelicht. Ten slotte biedt het hoofdstuk een kort overzicht van de meest voorkomende cardiale pathologieën, waarbij vooral de impact van de ziekte op de LV-vloeistofdynamica en de LV-torsiebeweging wordt benadrukt.

Numerieke methoden voor cardiale toepassingen

Teneinde enig inzicht te verschaffen in numerieke stromingsmechanica wordt gestart met de fundamentele vergelijkingen die een typische CFD-simulatie omvatten. Achtereenvolgens worden de meest courante numerieke methoden voor het omgaan met bewegende rekenrooster toegelicht, waarbij de werkingsprincipes, de verschillende implementaties en de voor- en nadelen worden benadrukt. Vervolgens wordt een literatuuroverzicht gegeven omtrent patiënt-specifieke CFD-modellering in het linkerhart, gericht op de specifieke uitdagingen verbonden aan deze applicatie: opleggen van de LV endocardiale beweging, incorporeren van de mitraalklep en de annulus, de trabeculae carnae, de regimetoestand van de stroming (overgang-tot-turbulent) en het rheologisch model van bloed. Ten slotte wordt ingegaan op de beperkingen van eerder binnen de onderzoeksgroep uitgevoerde onderzoek naar patiënt-specifieke CFD-modellering van het linkerventrikel ([1], [2]), wat het startpunt vormt van het uitgevoerde onderzoek.

Deel II - CFD-modellering van het contraherende LV gebaseerd op de Chimera-techniek: invloed van torsie op de intraventriculaire hemodynamica

4D patiënt-specifieke rekenroosters van het linker ventrikel

Het eerder door Bavo et al. [1], [2] ontwikkelde model van het linkerventrikel was gebaseerd op een Arbitraire Lagrangiaanse-Euleriaanse (ALE) implementatie van de roosterbeweging, en had als belangrijk nadeel dat de CFD-simulaties beperkt waren tot één hartcyclus of zelfs de diastolische fase, vanwege overmatige vervorming van het rekenrooster. Om deze beperking op te lossen werd een semi-automatisch hulpmiddel ontwikkeld voor de creatie van hoogwaardige 4D-gestructureerde rekenroosters van het LV-endocardium met als vertrekpunt uit medische beelden gesegmenteerde 4D-oppervlakken (3D volume dat verandert in de tijd). Deze 4D-roosters met 1-op-1 hoekpuntcorrespondentie worden dan gebruikt als input voor een CFD-oplosser. De applicatie is gebaseerd op isoparametrische transformaties waarbij een gewenste roosterpatch op de 4D gesegmenteerde LV-oppervlakken wordt geprojecteerd.

Na een beschrijving van de stappen die binnen de applicatie worden doorlopen, wordt deze toegepast op drie verschillende datasets, bekomen via

de drie meest courante beeldvormingsmodaliteiten (MRI, CT, US) teneinde de nauwkeurigheid en efficiëntie te evalueren. De gewenste nauwkeurigheid kan worden bekomen door het aantal controlepunten te variëren dat op de gesegmenteerde oppervlakken wordt geprojecteerd, terwijl het aantal rooster-elementen achteraf eenvoudig en kosteloos kan worden verhoogd via een verdere onderverdeling van de 4D-meshes. In onze implementatie was de nodige rekentijd voor de creatie van de rekenroosters niet afhankelijk van het aantal roosterelementen, maar van het aantal controlepunten dat de isoparametrische transformaties definieert. Het ontwikkelde algoritme liet toe om hoogwaardige 4D-gestructureerde rekenroosters te genereren met een maximale scheefheid van 0.9 en een minimale geschaalde Jacobiaan van 0.25 en 0.02 voor respectievelijk de roosters op het oppervlak en de grenslaag. De applicatie omvat tevens de temporele interpolatie van de 4D-roosters, waarbij de gebruiker zowel het aantal tussenliggende configuraties als het type interpolatie (volgens een natuurlijke of Bezier kromme) kan kiezen om te voldoen aan de temporele resolutie eisen van een CFD-berekening.

De ontwikkelde applicatie kan verder worden geoptimaliseerd op het vlak van gebruikersinteractie; hoewel deze minimaal is, is een volledige automatisering van het algoritme een waardevolle verdere ontwikkeling. Verder zou de projectie van de patches rechtstreeks kunnen worden geïntegreerd in de bewerking van de 4D-beeldvormingsdatasets (waardoor de noodzaak om de 4D-oppervlakken of puntenwolken te segmenteren wordt vermeden). Het algoritme heeft ook het nadeel dat de knooppunten van de gereconstrueerde 4D-roosters niet overeenstemmen met materiële anatomische punten van het ventrikel, waardoor bijvoorbeeld torsiebewegingen op een wat artificiële manier binnen de rooster-applicatie dienen te worden geïmplementeerd.

Invloed van torsie op de intra-ventriculaire hemodynamica in een patiënt-specifiek CFD-model van het LV gebaseerd op de Chimera-techniek

In dit hoofdstuk beschrijven we de ontwikkeling van een nieuwe methodiek voor het opzetten van patiënt-specifieke CFD modellen van het linker ventrikel. De methode is gebaseerd op de zogenaamde Chimera-techniek (overlappende rekenroosters) om fouten, te wijten aan negatieve volumes ten gevolge van een te grote vervorming van het rekenrooster bij een ALE-benadering, te vermijden. De Chimera-techniek, die zelden wordt toegepast in biomedische CFD-modellen, is vooral interessant bij het oplossen van problemen waarbij sprake is van grote en impulsieve beweging van het rekenrooster. De methode lijkt dan ook uitermate geschikt voor de studie van de intra-ventriculaire hemodynamica, waarbij we in deze studie specifiek de impact van de torsiebeweging van het ventrikel wensen te onderzoeken

op het stromingsveld in het ventrikel. De studie is gebaseerd op een patiënt-specifiek CFD-model, waarbij drie verschillende niveaus van torsie wordt opgelegd: geen torsie, fysiologische waarden (13°), en overdreven torsie (26°). We vergelijken snelheid, vorticiteit, de wandschuifspanning, het energieverlies en de verblijftijd van partikels voor de 3 bestudeerde gevallen. Er werden telkens zes hartcycli gesimuleerd om de overgangseffecten te minimaliseren, en evalueerden het energieverlies en de partikelverblijftijd tijdens de 5e en 6e cyclus, terwijl de resterende variabelen werden vergeleken aan het einde van de systole van de 6e cyclus (maximale verschil in de torsiehoek).

De ontwikkelde methode, gebaseerd op het semi-automatische meshing-algoritme en de Chimera-techniek, liet voor de 3 bestudeerde gevallen toe om de grote vervorming van het LV-endocardium te implementeren zonder dat dit resulteerde in een te vervormd rekenrooster. We observeerden kleine variaties van cyclus tot cyclus voor de bestudeerde variabelen, die nog steeds aanwezig waren na zes cycli, waarschijnlijk als gevolg van de hoge dynamiek van de casus. De impact van torsie was marginaal op snelheid, vorticiteit en wandschuifspanning, en niet te detecteren voor het energieverlies.

Het effect van torsie op de residentietijd van partikels was dubbel: enerzijds verminderde torsie het aantal partikels die in de eerste hartslag werden uitgepompt; anderzijds leidt supra-fysiologische torsie tot een verhoogde beweeglijkheid van de deeltjes die nog steeds in het LV aanwezig zijn na twee hartslagen. Hoewel de resultaten van het model sterk beperkt zijn door de afwezigheid van de mitralisklep, de papillaire spieren en de trabeculae in de simulaties, lijken ze toch te suggereren dat fysiologische waarden van torsie een verwaarloosbaar effect hebben op de LV hemodynamica. Gezien de cruciale impact van de mitralisklep (MV) op de LV hemodynamica, kan torsie het beste worden onderzocht in een model dat ook de mitralisklep omvat.

Een CFD-studie over de interactie tussen torsie en vortex-geleiding door de mitralisklep bij de spoeling van het linkerventrikel

Het is bekend dat de mitralisklepbladen een grote impact hebben op de ontwikkelde intraventriculaire stroming. Dit hoofdstuk bouwt dan ook voort op het eerder gedefinieerde patiënt-specifieke CFD-model van het LV, met de implementatie van een patiënt-geïnspireerd model van de mitralisklep, waarbij opnieuw de Chimera-techniek wordt gehanteerd. Het model van de mitralisklep werd opgebouwd uit MRI-beeldvormings data op de diastolische A-piek; de kinematica van de klepbladen op andere tijdstippen wordt gedefinieerd door specifieke rotatiehoekprofielen toe te wijzen aan vier verschillende delen die de klep vormen (anterieure en posterieure bladen, twee commissuren). De impact van torsiebeweging op de LV hemodynamica werd geëvalueerd door een casus met en zonder fysiologische torsie te

vergelijken, waarbij telkens zes hartcycli werden gesimuleerd. De snelheid, vorticiteit en wandschuifspanning werden geëvalueerd op de E-piek, A-piek, en einde systole van de 6e cyclus, terwijl het energieverlies en de partikel-verblijftijd tijdens de 5e en 6e hartcyclus werden berekend. De invloed van de mitralisklep op de LV-vloeistofdynamica werd geëvalueerd door de simulatie met fysiologische torsie, maar met en zonder klep te vergelijken.

In dit geval vertonen alle simulaties na zes hartcycli belangrijke variaties van cyclus tot cyclus. Torsie had een marginale invloed op snelheid, vorticiteit, en de wandschuifspanning, terwijl het energieverlies met + 14% toenam. Torsie had een positieve invloed op het aantal partikels dat na één hartslag het ventrikel verlaten had (+ 9,8%), en een marginaal effect op de deeltjes die binnen twee slagen werden geëjecteerd (+ 2%). Tegelijk verminderde torsie de beweeglijkheid van de deeltjes die zich in de LV-kamer bevinden na twee hartslagen. Al bij al lijken deze effecten belangrijk genoeg om aan te bevelen om torsie mee op te nemen in patiënt-specifieke CFD-modellen van het linkerhart, vooral wanneer de studie zich focust op stagnatie van bloed (verblijftijd van partikels) en veranderde energetische omstandigheden (energieverlies). Het onderzoek naar de effecten van de mitralisklep op de intra-ventriculaire stroming toonde aan dat de aanwezigheid van de klep tot een toename van de snelheid en vorticiteitspiek leidt als gevolg van een meer uitgesproken vernauwing van de mitralis-opening. Bovendien vindt de vorming van de wervelring plaats aan de vrije rand van de klep in plaats van aan de ring. De aanwezigheid van de klep had een gunstig effect op de directe uitstroom uit het ventrikel (+ 23,5%), en op het aantal partikels dat in twee hartslagen werd uitgestoten (+ 17.3%). Samenvattend kan worden gesteld dat de mitralisklep de penetratie van de jetstroming en de vortexring in het ventrikel naar de apex vergemakkelijkt, waardoor de apicale uitspoeling wordt bevorderd.

Desalniettemin kent de studie enkele belangrijke beperkingen die de resultaten van de studie beïnvloeden. Het gesimuleerde slagvolume valt iets buiten het fysiologische bereik (109 ml versus 55-100 ml), waardoor hogere maximale snelheden (pieksnelheid = 2 m/s) worden bereikt dan voor een typisch fysiologisch geval. Mogelijk speelt de beperkte axiale resolutie (8 mm) van de gebruikte MRI scan hierin een rol, met ongetwijfeld een impact op de nauwkeurigheid van de segmentatie. Het is raadzaam om de workflow te testen op een gegevensset met hogere resolutie (bvb. 1 mm). Het is ook aan te bevelen om modellen te ontwikkelen die ook de trabeculae carneae includeren; de aanwezigheid van deze structuren kan mogelijk de rol van torsie versterken. Ten slotte ondervonden we enkele technische moeilijkheden bij het opzetten van het CFD-model, wat suggereert dat de Chimera-techniek (o.a. meer geavanceerde functies op de cut-control) en

vooral ook de compatibiliteit met de oplosser van het stromingsprobleem verder kan worden verbeterd (bv. een 2e orde temporele discretisatie).

Deel III - conclusies

Conclusies

Er werd met succes een workflow ontwikkeld die toelaat om patiënt-specifieke CFD-simulaties op te zetten voor de studie van intraventriculaire stromingsdynamica, en deze werd toegepast op een casus waarbij de rol van torsie op intraventriculaire hemodynamica werd gekwantificeerd. Torsie bleek enkel een significante rol te spelen in een model waarin ook de mitralisklep was opgenomen. De effecten van torsie lijken belangrijk genoeg om algemeen aan te bevelen om torsie mee te includeren in CFD modellen die de intraventriculaire stromingsdynamica analyseren, in het bijzonder bij studie van stase van bloed. Verdere technische ontwikkelingen kunnen best focussen op de creatie van bewegende rekenroosters, waarbij de verder geautomatiseerde applicatie best direct op medische beelden (in plaats van op gesegmenteerde beelden) kan worden toegepast. De Chimera-techniek kan ook verder worden verfijnd, met meer controle op een aantal technische operaties en betere integratie met de oplosser van het stromingsprobleem.

Introduction

Context of the work

Since the last decades, cardiovascular disease (CVD) has been the global leading cause of death, accounting for 17.8 million deaths worldwide in 2019 (one-third of the global deaths), expected to be 23.6 million by 2030 [3]. Several CVDs - such as hypertension, atherosclerosis, valvular heart disease, arrhythmias, and heart failure - affect the function of the heart resulting often in subtle but progressive alteration of the blood flow until reaching conditions whereby the subject develops symptoms and becomes a patient. Consequently, research has focused on the development of flow-derived biomarkers and algorithms to investigate pathophysiological conditions, to support early detection, and to plan surgical procedures [4]. In this regard, Computational Fluid Dynamics (CFD) modeling is a powerful tool particularly suited to evaluate variations in procedures or devices, to examine three-dimensionally the region of interest, and to investigate the effects induced by different conditions in a parametric study. Moreover, the reduction of computational time and cost every year makes CFD even more attractive as a clinical tool [5]. Taking advantage of the continuous improvement of computational power, the integration of CFD models with medical imaging paved the way for a research branch that tailors computational models to every individual patient, i.e. patient-specific modeling.

In vascular applications, patient-specific CFD models are being progressively approved for clinical use as diagnostic tool to evaluate the fractional flow reserve [6] and as surgical planning tool for Transcatheter Aortic Valve Implantation [7]. Conversely, the clinical integration of cardiac modeling is being delayed due to the complexity induced by some challenges, a.o.: the considerable motion of the endocardium, the fast-moving kinematics of the valve leaflets, the rugged endocardial surface induced by the trabeculae and papillary muscles, and the transitional-to-turbulent state of the cardiac flow. Therefore, these challenges must be addressed to allow patient-specific cardiac modeling to be integrated into cardiac clinical applications. In this context, this PhD thesis aimed to develop a workflow to build patient-specific

CFD models of the Left Ventricle (LV), allowing to evaluate meaningful flow biomarkers for the early detection of pathologies that cannot be derived from medical images.

MUSICARE program and partners

This research was part of the MUltiSectoral Integrative approaches to CArdiac caRE (MUSICARE) program supported by the European Horizon 2020 Framework through the Marie Sklodowska-Curie Action International Training Network (MSCA-ITN) European training Networks, project number 642458 (http://www.musicare-2020.eu). The MUSICARE program is a European trans-sectoral and multidisciplinary network composed of medical professionals, academia, and industry that aimed to shape PhD students for a career in research and technology focused on cardiac applications to deliver more effective treatments for patients. The partners of the MUSICARE consortium consisted of four universities (Universiteit Gent, Politecnico di Milano, Imperial College London, Technische Universiteit Eindhoven) and six industrial partners (FEops, Philips, Sorin, Materialise, Bel, Lifetec).

The projects can be divided into three main work packages related to: (i) Simulations of minimally invasive surgery and percutaneous valve therapies to quantify the biomechanical impact of new devices; (ii) Optimization of imaging modalities and definition of patient-specific computational cardiac models useful in the diagnosis and treatment; (iii) Development of new prognostic tools based on in vitro and *in silico* tissue models. The specific aim of this project (Task 2.4) was to propose a computer simulation framework for the quantitative assessment of intra-cardiac flow fields. Within the MUSICARE network, the PhD candidate of the bioMMeda research group was able to benefit from the collaboration with FEops, during a three-month internship, and with Politecnico di Milano, during a one-month secondment. Outside the MUSICARE network, the strong collaboration with the Fluid Mechanics team of Ghent University had a great impact on the outcome of the work.

Research Goals

The aim of this research was to develop a workflow to build patient-specific CFD models of the left ventricle able to provide meaningful intra-ventricular flow biomarkers that could be potentially used in the early detection of cardiac pathologies. This aim is reflected in the research goals:

Goal 1 *- Implementation of a semi-automatic algorithm to model the patient-specific moving left ventricular endocardium;*

Goal 2 *- Development of a patient-specific CFD model of the left ventricle based on the Chimera technique.*

Dissertation Structure Overview

This dissertation consists of three main parts.

Part I provides the clinical and computational background (Chapter 1 and Chapter 2, respectively) to understand the basics of the work. Chapter 1 describes the anatomical details, the physiology and pathophysiology of the left heart. Chapter 2 discloses the numerical fundamentals focusing on the main approaches to model the LV, then reports the challenges and the state of the art related to the patient-specific CFD models of the LV.

Part II represents the core of this dissertation. Chapter 3 describes the semi-automatic algorithm used to generate 4D multi-block structured grids of the left ventricle with nodal correspondence starting from medical images. Chapter 4 reports the workflow used to build a Chimera-based patient-specific model of the left ventricle, which is used to address the impact of the torsional motion on the left ventricular hemodynamics. In Chapter 5, a kinematic model of the mitral valve is implemented into the workflow to evaluate the effect of torsion on the intraventricular flow field in presence of the mitral valve.

Finally, Part III recapitulates the main findings and concludes with the future perspective of the work.

List of Publications

First-author peer-reviewed papers

- Canè F., Delcour L., Redaelli A., Segers P., Degroote J., A CFD study on the interplay of torsion and vortex guidance by the mitral valve on

LV wash-out (in preparation).

- Canè F., Selmi M., De Santis G., Redaelli A., Segers P., Degroote J., Mixed Impact of Torsion on LV Hemodynamics: A CFD Study Based on the Chimera Technique, *Computers in Biology and Medicine*, vol. 112, no. 103363, 2019.

- Canè F., Verhegghe B., De Beule M., Bertrand P.B., Van Der Geest R.J., Segers P., De Santis G., From 4D Medical Images (CT, MRI, and Ultrasound) to 4D Structured Mesh Models of the Left Ventricular Endocardium for Patient-Specific Simulations, *BioMed Research International*, Special Issue 2018, no. 7030718.

Conference contributions

- Canè F. , De Santis G., Redaelli A., Segers P. and Degroote J., Influence of Ventricular Torsion on Left Ventricular Hemodynamics : a Patient-Specific Model using the Chimera Technique, oral presentation at the *16^{th} International Symposium on Computer Methods in Biomechanics and Biomedical Engineering 2019*, Columbia University, New York, New York, USA.

- Canè F. , Selmi M., De Santis G., Redaelli A., Segers P. and Degroote J., Patient-Specific Modeling of the Left Ventricular Hemodynamics using the Chimera (or Overset Mesh) Technique, oral presentation at the *Summer Biomechanics, Bioengineering and Biotransport Conference Proceedings 2019*, Seven Spring, Pennsylvania, USA.

- Canè F. , Selmi M., De Santis G., Redaelli A., Segers P. and Degroote J., Does left ventricular torsion affect intraventricular fluid dynamics?, poster presentation at the *17^{th} National Day on Biomedical Engineering 2018*, Brussels, Belgium.

- Canè F. , De Santis G., Segers P. and Degroote J., Impact of Left Ventricular Torsion on Flow Dynamics: a CFD Modeling Study using the Overset Mesh Method., poster presentation at the *World Congress of Biomechanics 2018*, Dublin, Ireland.

- Canè F., Verhegghe B., De Beule M., Bertrand P.B., Van der Geest R. J., Segers P., De Santis G, From 4D medical images (CT, MRI, US) to 4D Structured Mesh Models for Patient-Specific Flow Simulations in the Human Heart, poster presentation at the *16^{th} National Day on Biomedical Engineering 2017*, Brussels, Belgium.

- Canè F., Verhegghe B., De Beule M., Bertrand P.B., Van der Geest R. J., Segers P., De Santis G, Mapping mesh tool for left ventricle modeling, poster presentation at the 15^{th} *National Day on Biomedical Engineering*, Brussels, Belgium.

- Canè F., De Santis G., Bavo A., Segers P., Quantification of intracardiac flow, poster presentation at the *Virtual Physiological Human 2016 Conference*, Amsterdam, The Netherlands.

I

Background

Chapters

Chapter 1

Anatomy, physiology and patho-physiology of the left heart

This chapter provides the needed background in terms of cardiac anatomy, physiology and patho-physiology of this dissertation of the Left Ventricle (LV).

1.1 Anatomy

1.1.1 The heart

The heart is the pumping muscle, located in the middle-left part of the thoracic cavity, which provides energy to the blood to flow through the circulatory system. It has a flattened cone shape with the base-apex direction going from the upper-right-back towards the bottom-left-anterior side, with an inclination of 60 degrees towards the left. Together with the roots of the great vessels, the heart is wrapped within the pericardium, a double layer sac composed of an inner serous layer and an outer fibrous one. The former lubricates the heart to prevent friction, whereas the latter anchors it to the surrounding tissues and prevents it from overfilling with blood.

The heart is a hollow organ composed of the right and left cavities, which act simultaneously as two pumps in series (see Figure 1.1). Each day it beats roughly 100 000 times, pumping cumulatively around 8 000 liters of blood.

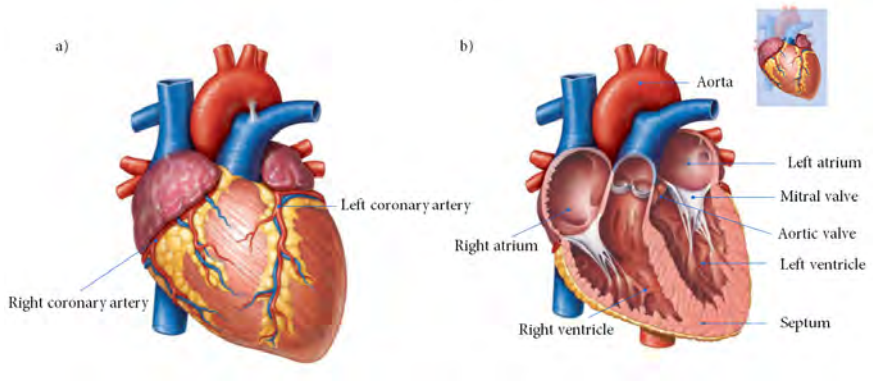

Figure 1.1: Anatomy of the heart. Adapted from [8].

The right heart pumps the venous blood towards the lungs through the pulmonary circulation, ensuring the exchange of oxygen and carbon dioxide. The left heart pumps the oxygen-rich blood to several body districts through the systemic circulation. See Figure 1.2 for a graphical representation of the systemic and pulmonary circulation. The left and right cavities are separated by the septum, which ensures absolute isolation of the deoxygenated (or "venous" blood) present in the right cavity from the oxygenated (or "arterial") blood in the left cavity. In turn, the left and right cavities are split into two chambers: the atrium and the ventricle in the upper and lower region, respectively.

The unidirectionality of the blood flow is maintained by the four cardiac valves, which open passively driven by the transvalvular pressure gradient. The venous blood flows from the right atrium to the right ventricle through the tricuspid valve; similarly, the arterial blood passes from the left atrium to the left ventricle through the mitral (or bicuspid) valve. The flow from each ventricle to the pulmonary and systemic circulation is controlled by two semilunar valves, named pulmonary valve and aortic valve on the right and left side, respectively. The pressure reached in the left ventricle is on average ten times larger than the one in the right ventricle [9]. This difference is needed to overcome the resistance of the systemic peripheral circulation, which is higher than the pulmonary circulation. The different pressure regimes structurally result in a thicker muscular wall in the left ventricle (12 mm) in comparison with the wall of the right ventricle (4 mm). Given the focus of this study on the left ventricle, the anatomy and physiology of the left heart are reported more in detail in the following sections.

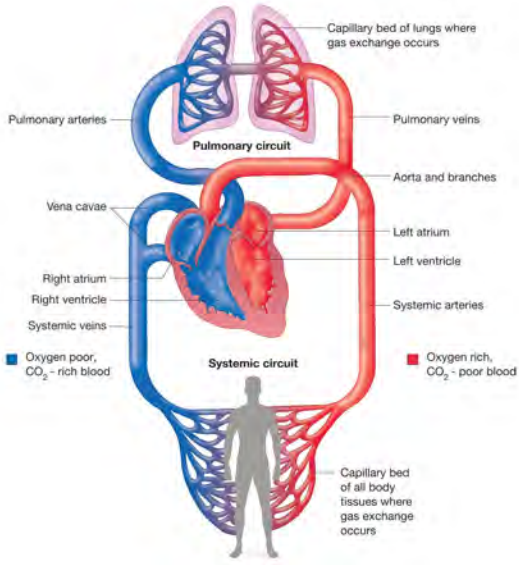

Figure 1.2: Schematic of the systemic and pulmonary circulation originating from the left and right ventricle, respectively. Adapted from [8].

1.1.2 Left atrium

The left atrium is the oval-shaped chamber that receives oxygenated blood from the four pulmonary veins. An appendage (a small tube-like structure) is commonly found on the left atrium which allows for decompression. The left atrium (Figure 1.3) supplies blood to the left ventricle through the atrioventricular orifice, better known as the mitral valve.

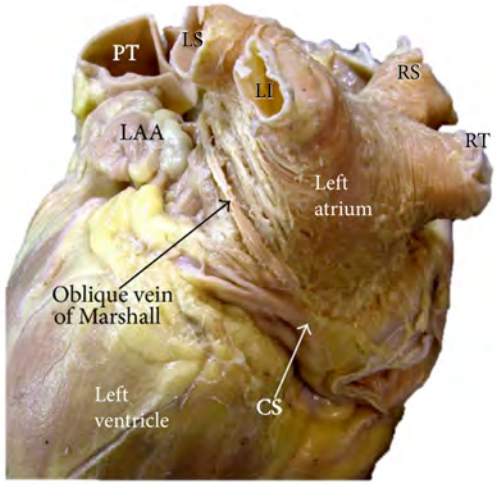

Figure 1.3: Posterolateral view of the left atrium and left ventricle in a human heart. LAA = left atrial appendage, PT = pulmonary trunk, CS = coronary sinus, LI = left inferior pulmonary vein, LS = left superior pulmonary vein, RI = right inferior pulmonary vein, RS = right superior pulmonary vein. Adapted from [10].

1.1.3 Mitral valve

The mitral valve (MV) is a complex structure composed of several elements whose mutual interaction guarantees its normal function: the annulus, the leaflets, the chordae tendinae, and the papillary muscles.

The annulus is a flexible saddle shape structure composed of fibrous and muscular tissue, by which the leaflets anchor to the endocardial wall. It supports the contractility of the ventricle thanks to the synergic kinematics with the myocardium.

From a strictly anatomical perspective, the mitral valve is monocuspid because of the tissue continuity along the circumference of the annulus. However, two large incisions named "commissures" divide the valvular connective tissue into two leaflets (see Figure 1.4 a): (i) the anterior leaflet, which extends over one-third of the circumference of the annulus in the proximity of the aortic valve, with a trapezoidal shape; (ii) the posterior leaflet, which occupies the remaining two-thirds of the annular circumference and is located on the ventricular wall side, with a rectangular shape [11].

The surface of each leaflet is composed of one regular and clear proximal zone, and one rough, irregular, and thicker distal zone, to which the chordae tendinae are attached (see Figure 1.4 b). A ridge marks the superior margin of the rough zone and corresponds to the coaptation line of the leaflet. During

systole, the rough zones of the leaflets overlap forming a coaptation along the apposition zone, which prevents the blood regurgitation from the ventricle to the atrium. Both leaflets are divided into three lobes or scallops (the anterolateral, the central, and the posterior-medial) by two indentations.

The valvular leaflets are connected to the left ventricle endocardium through the chordae tendinae and the papillary muscles, which together prevent the prolapse of the mitral valve leaflets into the atrium during systoles. The chordae tendinae are strands of fibrous-connective tissue that connect the heads of the papillary muscles (origin) to the rough zone of the valve leaflets (insertion). Between their origin and their insertion, they split into numerous branches distributing the mechanical load. The chordae can be classified into marginal, strut, or basal, with the insertion in the free margins of leaflets, in the border separating the rough and clear zones of the anterior leaflet, or limited to the posterior leaflet, respectively. The spatial distribution of the chordae is highly subject-specific [12]. The papillary muscles are two protruding muscle bundles (one anterolateral and one posteromedial) located close to the ventricular apex, whose contraction exerts a tensile action on the chordae tendinae that prevents the leaflets from prolapse during systole. The anatomical continuity between the ventricular wall, leaflets, chordae, and papillary muscles allows their synchronization, which is fundamental to preserve the ventricular function. The strong interaction between the mitral valve and cardiac walls explains how the valve can be affected by diseases caused by dysfunction of the myocardium (and vice versa), even if its sub-structures are intact [8], [10].

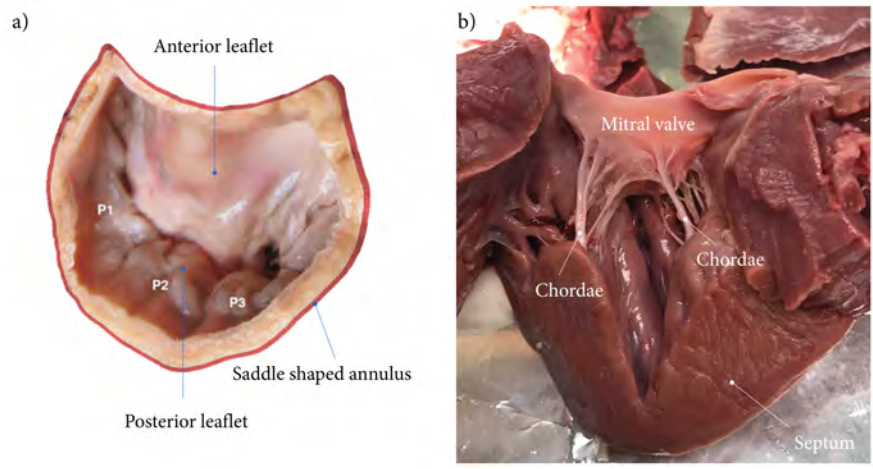

Figure 1.4: (a) Leaflets and annulus of the porcine mitral valve (top view), adapted from [11]; (b) Lateral section of the porcine Left Ventricle that shows the insertion of the Chordae Tendinae in the LV endocardium and the thickness of the septum, adapted from [12].

1.1.4 Left ventricle

The Left Ventricle (LV) is a conical-shaped chamber with the long axis passing through the apex and the center of MV orifice (Figure 1.4, b). The LV supports the systemic circulation and generates the highest pressure regime in the human body (120 mmHg on average), thanks to the thick muscular wall. Similarly to the rest of the cardiac tissue, the ventricular wall is composed of three layers that, from the outer to the inner layer, are: connective tissue (epicardium), muscular tissue (myocardium) and endothelial tissue (endocardium). The cardiac wall thickness is not uniform and varies from 7-10 mm at the basal level to 3 mm at the apex, and 7-9 mm at the free wall [13].

From a fluid dynamical perspective, the endocardium is the surface of interest since it is the one in contact with the blood. The morphology of the endocardium, shown in a longitudinal section (Fig 1.3, b), varies with the location: the inlet and apical zones have an irregular and spongy topology due to the presence of thin striated muscular structures named trabeculae carneae, whereas the outlet zone is smooth, partially composed of muscular and fibrous tissue [14]. The trabeculae carnae, described firstly by Leonardo da Vinci in his 'Trattato di Anatomia', allow blood to penetrate deep towards the apex, increase the blood-surface contact, support the papillary muscles during systole, reduce the walls shear stress and the turbulence state in the chamber [15]. The mitral and aortic valves, inclined by 30° to each other, are adjacent but separated by a continuous fibrous layer [8]. The left ventricle

endocardium can be divided along the long axis into the basal, medial, apical regions and the apex (Figure 1.5).

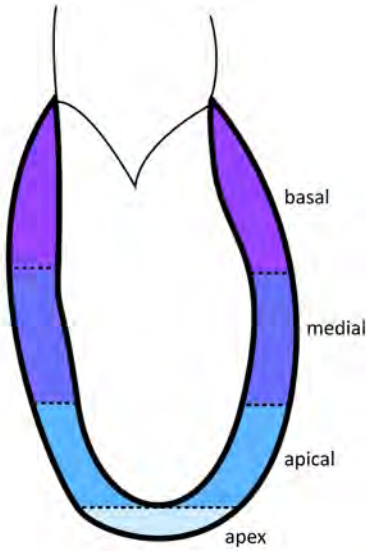

Figure 1.5: Endocardium of the Left Ventricle divided in the basal, medial, apical, and apex regions.

1.1.5 The aortic root and the aortic valve

The aortic root is the outflow tract of the left ventricle that supports the aortic valve [14], [16] (Figure 1.6). It changes dynamically and synergically during the cardiac cycle and consists of: (i) the aortic annulus, which is a fibrous ring that separates the left ventricle from the aorta and represents the attachment site of the leaflets; (ii) the valve itself, composed of three semilunar leaflets; (iii) the three sinuses of Valsalva, which are expansions of the aortic root delimited proximally and distally from the valve annulus and the synotubular junction, respectively; (iv) the synotubular junction, that supports the periphery of the valvular leaflets. The aortic valve regulates the blood flow towards the systemic circulation and the three semilunar leaflets are named corresponding to the sinuses of Valsalva where they are located: the right coronary cusp, the left coronary cusps, and the non-coronary cusp.

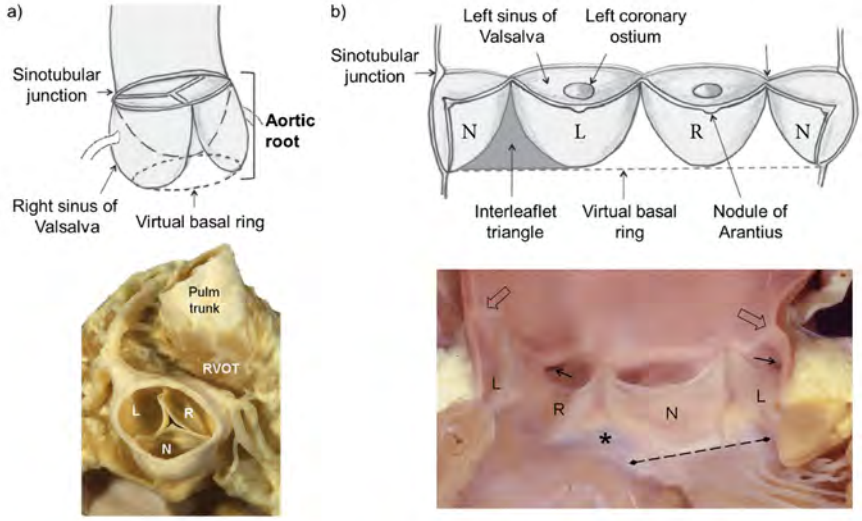

Figure 1.6: (a) Schematic representation (top) and top view (bottom) of the aortic root; (b) Schematic representation (top) and anatomical open section (bottom) of the aortic root. L = Left coronary cusp, R = Right coronary cusp, N = Non coronary cusp. Adapted from [14], [16].

1.1.6 Coronary arteries

The left (LCA) and right coronary (RCA) arteries supply oxygenated blood to the heart (Figure 1.7). They originate from the aortic sinuses and gradually divide into smaller arteries that penetrate towards the cardiac muscular surface, with the poor-oxygenated blood flowing through the capillary bed towards the cardiac veins. The right coronary artery supplies the right atrium, the right ventricle, the cardiac conduction system, and a small portion of the left ventricle, whereas the left coronary artery sustains the larger part of the left atrium, the left ventricle, and the inter-ventricular septum.

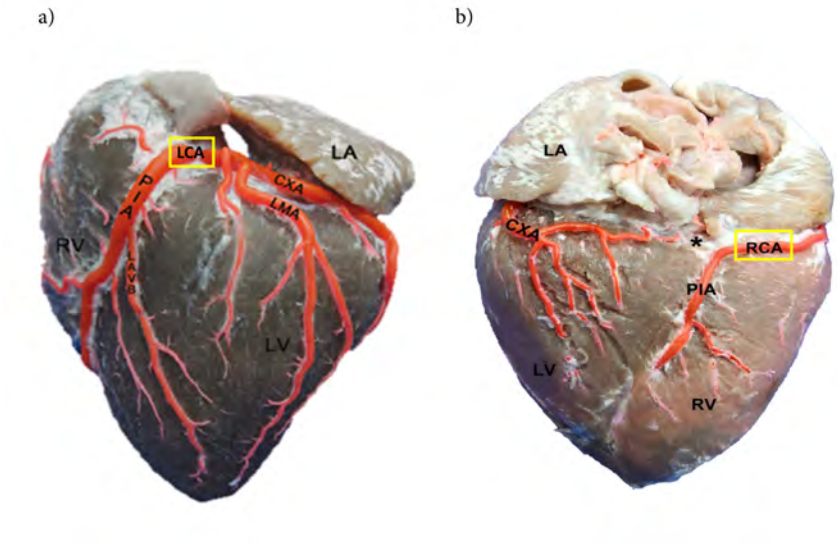

Figure 1.7: (a) Obtuse edge of the heart; (b) Posterior view of the heart. PIA = paraconal interventricular artery; CXA = circumflex artery; LAVB = first left anterior ventricular branch; LMA = left marginal artery; LA = left atrium; LV = left ventricle. RV = right ventricle. Adapted from [17], [18].

1.2 Physiology

1.2.1 Cardiac cycle

The cardiac cycle is the sequence of events between two heartbeats that allows the oxygenated blood and the deoxygenated blood to reach the systemic circulation and the lungs for the gas exchange, respectively. Physiologically, it typically lasts 0.8-0.9 seconds and it can be divided into two main mechanical phases activated by electrical impulses: the ventricular relaxation (diastole) and the ventricular contraction (systole). The mechanical events occurring in the left ventricle (Figure 1.8) during systole and diastole can be further subdivided into the phases described below.

Immediately preceding the isovolumetric contraction (phase 1a) the ventricle contracts with the consequent increase of the intra-ventricular pressure which induces the passive closure of the mitral valve. The ejection of blood towards the systemic circulation (phase 1b) begins when the intra-ventricular pressure overcomes aortic pressure (generally 80 mmHg) inducing the opening of the aortic valve and the resulting decrease of ventricular volume. This phase lasts around 270 ms and can be divided into rapid ejection (starting from the opening of the aortic valve until the maximum aortic pressure reaches 120 mmHg) and reduced ejection. Note that the left ventricle at end-

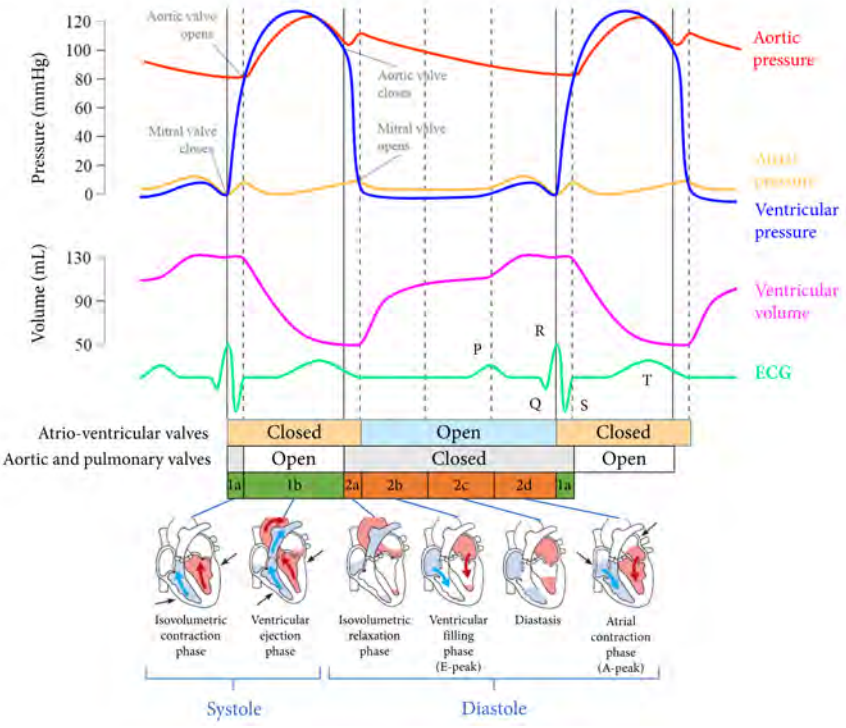

Figure 1.8: Schematic of the phases composing a cardiac cycle. The aortic pressure is reported in red, the left ventricular pressure in blue, the left atrial pressure in yellow, the ventricular volume in magenta, and the ECG in green. Adapted from [8] and [19].

systole is not empty, but contains about 50 mL of blood which corresponds to about half of the filling volume.

The isovolumetric relaxation (phase 2a) begins when the intra-ventricular pressure decreases below the aortic pressure inducing the closure of the aortic valve. During this phase, the LV sphericity increases and the motion of the MV leaflets towards the apex without opening induces a blood displacement into the LV before the separation and opening of the MV leaflets.

The filling phase starts when the intra-ventricular pressure drops below atrial pressure causing the opening of the mitral valve; it can be divided into three phases. Firstly, during the early-filling phase (E-peak, phase 2b), the most intense diastolic jet passes through the mitral valve inducing a sudden increase of ventricular volume. Secondly, there is a stasis (referred to as *diastasis*) where the ventricular volume increases slowly during a phase whereby which the atrial and ventricular pressure are almost equivalent (phase 2c). Finally, the atrial contraction (A-peak, phase 2d) induces a second

(lower) peak of the trans-mitral flow with the ventricular volume increasing up to 120 mL. The increase of ventricular pressure causes the closing of the mitral valve and the beginning of a successive heartbeat.

1.2.2 Intraventricular hemodynamics

The LV fluid dynamical patterns developed are strictly related to the mechanical events of a cardiac cycle and have been object of several studies as a potential indicator of pathologies (Figure 1.9). Particularly, the LV blood flow is characterized mainly by an asymmetric vortex ring during diastole.

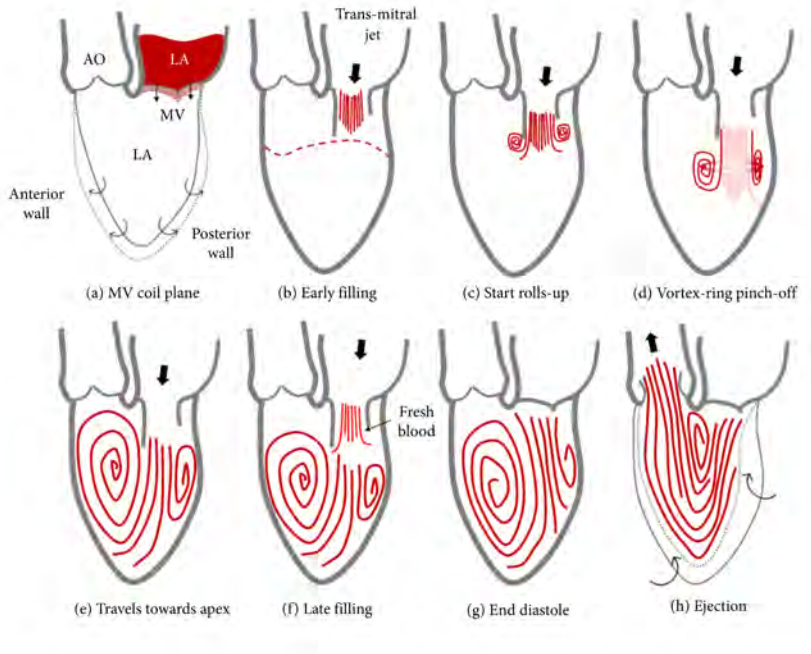

Figure 1.9: Sketches of intraventricular flow structures during one cardiac cycle. Adapted from [20].

At the beginning of the filling phase, the conical shape of the opening MV leaflets induces the formation of a transmitral blood jet. The shear layer between the leaflets and the blood rolls up and turns into an asymmetrical vortex ring, whose features and development are strongly affected by the asymmetric shape and inclination of the MV leaflets. The eccentricity of the mitral annulus was found to impact significantly (about 10 %) the viscous dissipation of the intraventricular flows with an optimal value resulting from a position that most closely resembles that of the physiological heart [21].

The toroidal vortex ring propagates progressively dissipating towards the apex, and it is paramount in terms of ventricular flow energetics to maintain the motion of the incoming fresh blood during the filling phase, avoiding thrombus formation, and to enhance the ejection by redirecting the blood towards the outflow tract [22], thus maintaining a close interplay of the filling and the ejection phases. The vortex ring formation enhances both the mutual interaction between diastole and systole by reducing the workload needed to re-accelerate the blood during ejection [22] and the mass transport from the left atrium occurring during the early filling [23], [24].

The intra-ventricular flow dynamics is the result of multiple factors - a.o. the temporal variation of the LV volume and shape, the endocardial motion and morphology, the action of the mitral valve, and the correct timing of the phases composing a cardiac cycle induced by regular electrical activity - and has been extensively studied to fully comprehend the slow transitions that from a physiological condition silently lead to the onset of pathologies. The flow alterations, known to be induced by the most common pathologies, are reported in a following section.

1.2.3 Functional indices of ventricular function used in clinics

The physiological working conditions of the left ventricle and the impairment induced by pathological conditions can be evaluated through several functional indices. We report the most commonly used ones.

As a pumping system, the work done by the LV can be derived as the area within the pressure-volume diagram (Figure 1.10). It is clinically derived via cardiac catheterization, an invasive procedure that requires the insertion of a multisensory-catheter in the heart and arteries providing: (i) the time varying conductance drop between to catheterized points and (ii) the intraventricular pressure. It is still referred to as the gold standard to assess severe cardiac valve stenosis or congenital heart diseases [25].

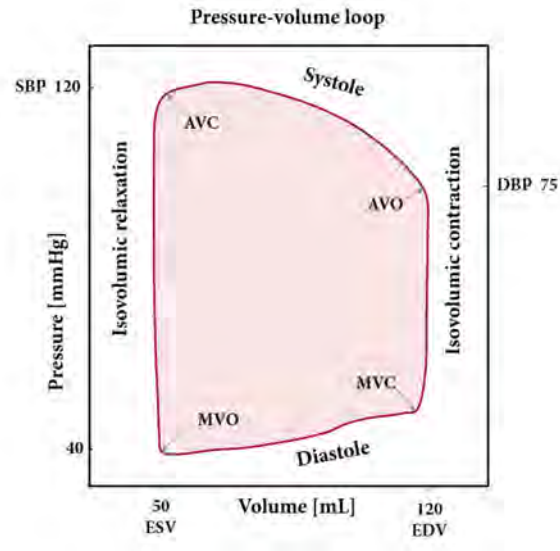

Figure 1.10: Pressure-Volume curve of the left ventricle. SBP and DBP = systemic systolic and diastolic blood pressure, respectively. MVO and MVC = mitral valve opens and mitral valve closes, respectively. AVO and AVC = aortic valve opens and aortic valve closes, respectively. Adopted from [25].

The Stroke Volume (SV) represents the volume of blood pumped by the left ventricle per beat and is computed as the difference between the End Diastolic Volume (EDV) and the End Systolic Volume (ESV), equation 1.1).

$$SV = EDV - ESV \tag{1.1}$$

The Ejection Fraction (EF) is the part of the end-diastolic volume ejected during systole, commonly used to evaluate the pumping efficiency of the heart (equation 1.2). The pumping condition of the heart can be classified based on the EF ranges as: normal (EF = 55-70 %), slightly below normal (EF = 40-54 %), moderately below normal (35-39 %), severely below normal (EF < 35 %) [26].

$$EF = \frac{SV}{EDV} \cdot 100 \tag{1.2}$$

The E/A ratio evaluates the ventricular diastolic filling, which in pathological cases of diastolic dysfunction can lead to heart failure. It is computed as the ratio of peak blood velocity during the E-wave over the A-wave and results in: normal diastolic function (E > A), impaired relaxation (E < A), pseudo-normal (E > A, but relaxation is abnormal), restrictive filling (E > 2

A). Doppler ultrasound can be used to assess the cardiac flow and potential abnormal patterns, by measuring an extensive number of indices related to cardiac flow (such as the E/A ratio, cardiac index [27], [28], cardiac output [29], valvular regurgitation [30], blood flow velocity [25]), and also the tissue kinematics of the mitral annulus and the ventricular wall [26]. Among other ultrasound imaging modalities, strain and strain rate imaging and elastography assess the stiffness and the deformation of the ventricle. Also Magnetic Resonance Imaging (MRI) is extensively used in cardiac applications to evaluate the cardiac function and structure, the perfusion of the coronary arteries and the intra- and extra-cardiac flow.

1.2.4 Emerging functional indices quantifying intraventricular hemodynamics

The potential link between LV fluid dynamics and the events that trigger the onset of a pathology led to the definition of several quantitative indices to represent the characteristic features of the intraventricular fluid dynamics. The quantification of the diastolic vortices, which is paramount to maintain the blood in motion and an adequate washout of the LV chamber, is not trivial and several indices have been proposed in this regard. The most widely adopted are the λ_2 [31] and the Q criteria (Figure 1.11).

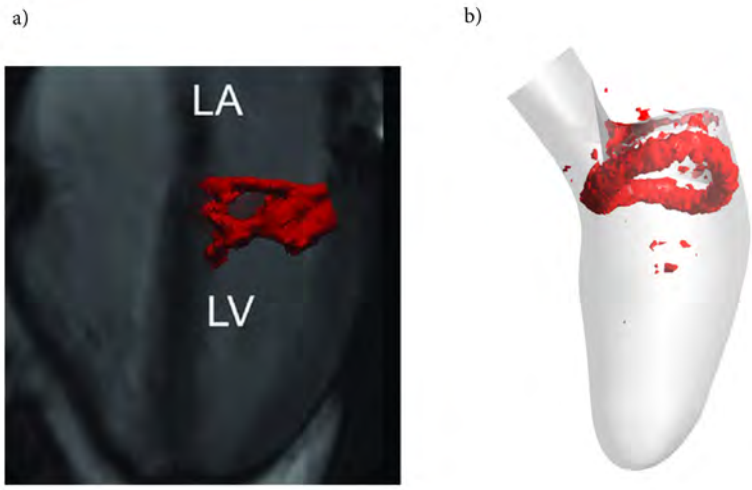

Figure 1.11: Diastolic 3D vortex structure visualized by iso-surface of λ_2 (left) and Q-criterion (right). Adapted from [32], [33].

The λ_2 criterion identifies the regions where the low values of pressure are associated with the rotation of the flow field, both at low and high Reynolds numbers. Mathematically, this is achieved as follows. Firstly, the velocity gradient tensor **J** is computed (equation 1.3) with x, y, z being the directions of the coordinate systame and u, v, w the velocity components:

$$\mathbf{J} = \begin{bmatrix} \frac{\partial u}{\partial x} & \frac{\partial u}{\partial y} & \frac{\partial u}{\partial z} \\ \frac{\partial v}{\partial x} & \frac{\partial v}{\partial y} & \frac{\partial v}{\partial z} \\ \frac{\partial w}{\partial x} & \frac{\partial w}{\partial y} & \frac{\partial w}{\partial z} \end{bmatrix} \tag{1.3}$$

Secondly, the velocity gradient tensor **J** is decomposed into its symmetric part, the strain deformation tensor ($\mathbf{S} = \frac{\mathbf{J}+\mathbf{J}^{\mathrm{T}}}{2}$), and the asymmetric part, the spin (or vorticity) tensor ($\Omega = \frac{\mathbf{J}-\mathbf{J}^{\mathrm{T}}}{2}$), where T represents the transpose operation. Thirdly, the eigenvalues of $(S^2 + \Omega^2)$ are computed as $\lambda_1, \lambda_2, \lambda_3$ and the vortex core is located where two negative eigenvalues occur, $\lambda_1 \geq \lambda_2 \geq \lambda_3$, which corresponds to $(\lambda_2 < 0)$. Usually, due to the noise of the velocity data, a threshold $\left(T_{\lambda_2} < 0\right)$ is applied to better separate the strong vortex structures from the weaker [31], [34].

The Q criterion [35] detects an eddy as the region in the velocity field where the Euclidean norm of the vorticity tensor (Ω) overcomes the norm of the strain rate tensor (**S**) and the pressure is lower than the ambient value (equation 1.4):

$$Q_{criterion} = \frac{1}{2}\left(|\vec{\Omega}|^2 - |\vec{S}|^2\right) > 0 \tag{1.4}$$

Without threshold applied, the condition $\lambda_2 < 0$ corresponds to a subset of the $Q_{criterion}$, therefore the λ_2 criterion relies on the strictest condition to identify the vortices [36].

The Energy loss (EL) is the amount of fluid energy lost as heat caused by the friction between the flowing blood and wall shear flow due to blood viscosity. It can be computed, under the assumption of incompressible fluid, as the viscous dissipation term of the Navier-Stokes equations, reported in equations 1.5 and 1.6, where $\frac{1}{2}\left(\frac{\partial \boldsymbol{u}_i}{\partial \boldsymbol{x}_j} + \frac{\partial \boldsymbol{u}_j}{\partial \boldsymbol{x}_i}\right)$ represents the strain deformation rate in the fluid domain, V_i the volume cell, and μ the blood dynamic viscosity.

$$\phi_V = \frac{1}{2}\mu \sum_{i=1}^{3}\sum_{j=1}^{3}\left[\left(\frac{\partial \boldsymbol{u}_i}{\partial \boldsymbol{x}_j} + \frac{\partial \boldsymbol{u}_j}{\partial \boldsymbol{x}_i}\right)\right]^2 \tag{1.5}$$

$$EL = \int_{to}^{t1} \sum_{i=1}^{num\ \mathrm{voxels}} \phi_V V_i \mathrm{d}t \tag{1.6}$$

The EL increases in case of pathological intra-ventricular flow patterns, such as turbulence, jet, or adverse direction. It is clinically relevant to detect cardiac dysfunction in diabetic patients [37], [38] and subclinical cardiac dysfunction in patients with hypertrophic cardiomyopathy [39]. The increased interest in recent and upcoming studies [40], [41] might provide new insights and spread the contribution in clinical cardiac applications.

The Residence Time (RT), typically associated with particle tracking, measures the time spent by blood particles injected in the left ventricle cavity. It can be used to evaluate the distribution of particles ejected within multiple cycles, the particles' motility, the ventricular wash-out, and the blood stasis. The particles ejected at the first beat and the ones remaining in the LV after a few beats are referred to as direct flow and residing particles, respectively.

The Wall Shear Stress (WSS) is the frictional force exerted by the blood flow on the wall that plays a leading role in the remodeling mechanisms, typically altered in case of pathologies. Under the assumption of laminar flow, the WSS is defined as the product between the fluid dynamic viscosity (μ) and the normal velocity gradient at the wall $\frac{\partial u}{\partial n}$ (equation 1.7):

$$\tau_w = \mu \frac{\partial u}{\partial n} \tag{1.7}$$

The Time Averaged Wall Shear Stress (TAWSS) is typically computed by averaging the WSS vector over one cardiac cycle (equation 1.8):

$$\text{TAWSS} = \frac{1}{T} \int_0^T \|\vec{\tau}\| \mathrm{d}t \tag{1.8}$$

In this study, the WSS is reported by means of the bull's eye plot. The bull's eye is a representation, recommended by the American Heart Association, that subdivides the LV endocardium into 17 sectors (Figure 1.12): longitudinally it is subdivided into four zones (basal, medial, apical, apex); circumferentially it is subdivided into six zones in the basal and medial sectors, four zones in the apical and one in the apex. It is typically used in clinics to quickly highlight the infarcted myocardial zones, and also adopted in research to represent the local distribution of the WSS as an indicator of stasis and thrombus formation.

1.3 Cardiac and valvular pathologies

In case of pathologies, the heart continuously adapts to sustain blood perfusion and undergoes tissue remodeling mechanisms. This is most commonly a slow process, which makes the detection of pathologies complicated. The

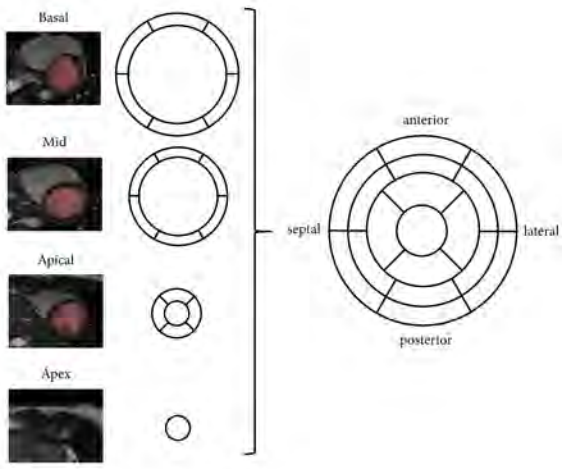

Figure 1.12: Sectors of the Bull's eye plot. Adapted from [42]

disease is most often only detected when the patient develops symptoms and when the heart has undergone irreversible pathological changes. The tissue remodeling mechanisms caused by pathologies remain insufficiently comprehended but appear to be linked with mechanical and fluid dynamic factors [43].

Heart failure accounts for more than 23 million cases worldwide every year and occurs when the heart is unable to pump an adequate amount of blood flow and sustain sufficiently high pressure. Different pathologies impair physiological cardiac functionality and can cause heart failure, a.o. cardiomyopathies, myocardial infarction, heart valve diseases, and abnormal electrical conduction of the excitation signal [44].

Based on the morphology and ventricular functionality, cardiomyopathies can be classified as dilatative, hypertrophic, and restrictive. Each cardiomyopathy reflects a specific phenotypic pattern and affects a specific transversal portion of the cardiac tissue, however, they all can cause an impaired stroke volume that, in turn, can lead to flow stagnation, delayed washout, and limited systemic perfusion. Since we will particularly address the contribution of torsion to intraventricular flow dynamics, we briefly highlights the effects of cardiac pathologies on torsion in the following section.

Dilated CardioMyopathy (DCM) corresponds to an increased ventricular volume with normal or reduced wall thickness, and induces a loss of contractility extended to the subepicardial layers. In the earliest stage it also induces blood flow abnormalities that represent the major predictors of adverse events [45], a.o. a prolonged inflow phase, increased apical and outlet

velocities with significant mitral regurgitation, and a later dissipation of the early-diastolic anteroseptal vortex ring. In comparison with controls, DCM is associated with a decreased direct flow (i.e. flow ejected at the first beat) and an increased residual volume (i.e. flow remaining in the LV) after two beats ($P<0.0001$), respectively [46]. Furthermore, it increases the incidence of cardiac valve pathologies, arrhythmias, and blood clots. In Hypertrophic CardioMyopathy (HCM), a portion of the cardiac tissue thickens and becomes stiffer, resulting in impaired systolic and diastolic functions [47]. The morphological alterations induce elevated filling pressures, slower trans-mitral velocity, smaller vortices, and decreased EL ([38], [48]. Both DCM and HCM can be obstructive or non-obstructive depending on whether the location of the structural alteration occurs close to the LV outflow or the apex, respectively. In restrictive cardiomyopathy, the stiffer cardiac tissue impairs filling and ejection, however, it is the least common and its origin is still debatable. Both the hypertrophic and restrictive cardiomyopathies affect only the subendocardial layers reducing the elongation and shortening in the longitudinal direction.

Acute myocardial infarction (AMI) is the necrosis of cardiac tissue due to a prolonged and insufficient supply of oxygenated blood induced by an obstruction or a narrowing of the coronary arteries. Therefore, the affected portion of the cardiac tissue is functionally compromised, and this leads to an impaired direct flow ($P<0.0001$) [46].

Valve pathologies are the direct and indirect cause of cardiac dysfunction. Pathological valves can be: (i) stenotic, when they cannot fully open with consequent higher hydraulic resistance; (ii) insufficient, when the leaflets are not completely sealed during closure allowing a backward leak across the valve (i.e. regurgitant flow); (iii) or a combination of the two conditions. Both pathological conditions can be induced by stiffer and/or calcified leaflets. Insufficiency can also be a consequence of cardiac or aortic/pulmonary dilation, and disruption of the chordae tendinae. The most common conditions of cardiac valve diseases are aortic stenosis and mitral regurgitation, which occur in 3 out of 4 pathological cardiac valves [49].

1.4 Effect of cardiac disease on torsion

The LV motion can be split into the perpendicular motion component (contraction and relaxation) and the twisting or torsional component. Torsion is defined as the angular difference of the simultaneous clockwise basal rotation and the counterclockwise apical rotation (typically 13-14° in physiological cases), seen from the basal view (Figure 1.13). The LV twisting and uncoiling occur during systole and diastole, respectively. Given the correlation

of torsion with EF and cardiac longitudinal deformations [50], it has been proposed as an index to evaluate the LV functionality and the alterations induced by pathologies.

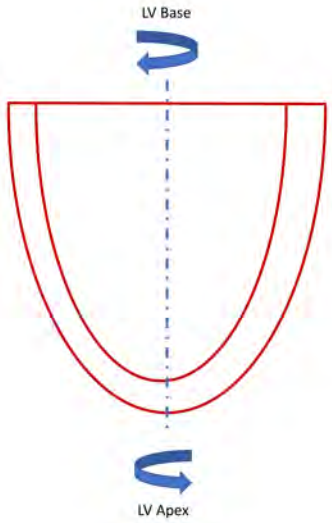

Figure 1.13: The torsional motion of the LV is defined as the rotational angular difference between the apex and the base.

The LV torsion supports the accumulation and the release of energy during systole and diastole, respectively [51]. Furthermore, due to the correlation with LV functional indexes, such as EF and cardiac longitudinal deformations [50], it is currently being investigated as a potential index to detect pathologies in an early stage, also because it can be easily quantified via ultrasound speckle tracking [47]. In this regard, several studies have been performed to study the effects of cardiac and valvular diseases on the LV twist.

The effects of cardiomyopathies can be summarized as follows: the increased sphericity in DCM LV induces a blunted twist degree (around 9°) and a delayed untwisting [50]; in HCM patients the thicker muscular tissue induces more pronounced radial differences between the endocardium and the epicardium (around 16°), resulting in an enhanced LV torsion [47]; on the contrary, restrictive cardiomyopathy preserves the torsional functionality within physiological values (typically 14°. Infarcted patients with normal EF have impaired torsion (around 7°) [52]. Regarding valvular pathologies, torsion increases with the hemodynamic loading conditions, such as aortic valve stenosis with preserved EF (around 20-25°), whereas it reduces in case of chronic mitral regurgitation with LV systolic dysfunction (around 3-6°), due to a decreased lever arm force of the epicardial fibers.

Several methods and algorithms have been proposed to evaluate the LV torsion [53]–[55]. However, the influence on the LV fluid dynamical patterns has never been tested in clinics and in vitro, due to the difficulty of isolating this motion component, representing the perfect case study for CFD simulations. It is exactly the strength of computational models to investigate changes due to isolated alterations of a given factor, rendering the study of the impact of ventricular torsion a perfect showcase and application for the computational workflow that has been developed within this PhD dissertation.

Chapter 2

Numerical methods for cardiac applications

This chapter provides an overview of the numerical fundamentals to understand this work, the state of the art of patient-specific Left Ventricle (LV) modeling with the related challenges, and, finally, a focus on the previous studies performed in our research group on the same topic.

2.1 Introduction

Computational fluid dynamics modeling has been widely adopted in cardiac applications to estimate variables of interest in locations not accessible by in-vivo measurements, to reduce the time and cost of in-vitro set-ups, and to perform parametric studies effectively. The fluid dynamics are assessed by solving the partial differential (PDEs) Navier-Stokes equations and the continuity equation within a geometry under the constraints of a set of boundary conditions and fluid properties. The PDEs can be discretized and solved with Finite Differences, Finite Element methods, or the Finite Volume (FV) methods. Among these, the FV method stands out historically to solve fluid flows (i.e. fluxes). In the Finite Volume (FV) method, the fluid domain is subdivided into small volumes (i.e cells) and, after the definition of both the fluid properties (density, viscosity) and the boundary conditions, the conservation of mass and momentum equations are solved at the center of each cell resulting in a system of linear equations. In the CFD modeling of an LV chamber, the implementation of the motion of the LV endocardium and

MV leaflets is crucial to replicate the typical intra-ventricular flow patterns, but introduces challenges on mesh handling as a high quality mesh of the fluid domain, which dynamically changes over time, is required at all time instants. In this context, two main approaches can be used: the deforming (among others the Arbitrary-Lagrangian Eulerian, ALE) and the non-deforming (among others the Immersed Boundary Method, IBM) mesh methods.

The details of each methodology are reported in the following sections. As a brief preview of the technical details disclosed in the upcoming sections, the ALE approach represents the fluid domain using a volume mesh. The external surface accurately follows the motion - whether prescribed from images in a patient-specific kinematic model or as the result of a Fluid-Structure Interaction (FSI) model - and the internal part that undergoes smoothing or remeshing to preserve the mesh quality. On the other hand, the IBM describes the fluid domain using a surface mesh embedded in a 3D static Cartesian grid and imposes the boundary conditions as a body force term in the Navier-Stokes equations. In terms of advantages and disadvantages, the ALE approach allows a fine evaluation of the flow field on the interface (important for the computation of interface stresses such as WSS), but it is limited to handle very large deformations. On the other hand, IBM is suited to handle problems with impulsive kinematics because it requires fewer constraints on the moving mesh (or object) but lacks accuracy at the interface between the grids due to the low resolution normal to the wall.

The main disadvantage of the ALE approach was experienced in a patient-specific CFD model of the LV previously performed within our research group (PhD work of Dr. Alessandra Bavo). This work can be considered as the precursor of the current dissertation and the calculations were limited to one cardiac cycle [1] or even the diastolic phase [2], due to negative volume errors in the CFD solver induced by excessive mesh distortion due to the large, rapid motion of the mitral leaflets.

In this regard, after having developed an algorithm to generate 4D LV grids that checks the mesh quality before the CFD calculation (extensively reported in Chapter 3), we based our CFD models of the LV on the Chimera technique, which combines the advantages of both IBM and ALE approaches allowing to handle the kinematics of several moving components - such as the LV endocardium and MV leaflets - while preserving accuracy on the WSS computation. Furthermore, the Chimera technique should allow us to handle the separation of the fluid domain during the valve coaptation without a local fictitious increase of viscosity or added source term in the Navier-Stokes equations as was done in previous work from our group [1].

This chapter is structured as follows: firstly, the fundamental equations of a fluid dynamical problem are introduced, conservation of mass and

momentum (i.e. the Navier-Stokes) equations; secondly, the approaches with deforming and non-deforming fluid domains are described, focusing mainly on the ALE approach and the Chimera technique; thirdly, the state of the art about the CFD models of the LV and MV is briefly reported.

2.2 Fundamental fluid dynamics equations

The fundamental equations of an isothermal fluid flow are the conservation of mass and momentum (i.e. Navier-Stokes equations).

The mass conservation equation (see equation 2.1) expresses the principle that the change in mass is equal to the net flow through boundaries, where ρ_f and $\vec{v_f}$ represent the fluid density and the fluid velocity vector, respectively. In cases where the volume changes:

$$\frac{\partial \rho_f}{\partial t} + \nabla \cdot \left(\rho_f \vec{v}_f\right) = 0 \tag{2.1}$$

Under the assumption of incompressible fluid ($\rho_f = constant$), equation 2.1 can be rewritten as in equation 2.2:

$$\nabla \cdot \vec{v}_f = 0 \tag{2.2}$$

The Navier-Stokes equations (N-S) can be written as in equation 2.3, where the external forces are split into the surface forces per unit of surface ($\overline{\sigma_f}$ [N/m^2]), expressed with the Cauchy stress tensor, and the body forces per unit of volume ($\overrightarrow{f_f}$ [N/m^3]):

$$\rho_f \frac{\partial \overrightarrow{v_f}}{\partial t} + \rho_f \overrightarrow{v_f} \cdot \nabla \overrightarrow{v_f} = \nabla \cdot \overline{\sigma_f} + \overrightarrow{f_f} \tag{2.3}$$

In cardiovascular applications, the effect of gravity (a body force) may be neglected and the fluid can be considered incompressible leading to the formulation in equation 2.4:

$$\rho_f \frac{\partial \overrightarrow{v_f}}{\partial t} + \rho_f \nabla \cdot \left(\overrightarrow{v_f} \overrightarrow{v_f}\right) = \nabla \cdot \overline{\sigma_f} \tag{2.4}$$

The solution of the N-S equations requires to link the Cauchy stress components with the kinematic variables (a.o. the velocity). The Cauchy stress tensor ($\overline{\sigma_f}$) can be divided into the normal stresses - the pressure term (p_f) - and the shear stress component ($\overline{\tau_f}$) induced by the viscous

forces. Under the assumption of blood as Newtonian fluid (i.e. viscosity μ independent from shear rate), it is possible to obtain equation 2.5, where $\bar{I}$ is the identity tensor, $\overline{\varepsilon_f}$ is the strain rate tensor computed as in equation 2.6:

$$\overline{\sigma_f} = -p_f\bar{I} + \bar{\tau}_f = -p_f\bar{I} + 2\mu\bar{\varepsilon}_f \tag{2.5}$$

$$\bar{\varepsilon}_f = \frac{1}{2}\left[\nabla\vec{v_f} + \left(\nabla\vec{v_f}\right)^T\right] \tag{2.6}$$

Integrating equations 2.5 and 2.6 in equation 2.4 results in equation 2.7:

$$\rho_f\left(\frac{\partial\vec{v_f}}{\partial t} + \nabla\cdot\left(\vec{v_f}\vec{v_f}\right)\right) = \nabla\cdot\left(-p_f\bar{I} + \mu\nabla\vec{v_f} + \mu\left(\nabla\vec{v_f}\right)^T\right) \tag{2.7}$$

2.3 Modelling turbulence

The cardiac flow is one of the main sites in the cardiovascular system characterized by a transitional-to-turbulent regime, in which velocity and pressure chaotically change. The flow regime is typically assessed with the Reynolds number, defined as the ratio between inertial and viscous forces:

$$Re = \frac{vD\rho}{\mu} \tag{2.8}$$

where v is the velocity, D is the diameter of the MV in this case (under the assumption of circular cross-section, $D = 2\sqrt{A_{MV}/\pi}$), μ and ρ are the viscosity and the density of the fluid. The following thresholds are typically used to characterize the flow regime of the blood in the human body: laminar regime ($Re < 2300$), transitional regime ($2300 < Re < 4000$), turbulent ($Re > 4000$). in a turbulent flow, fluctuations are induced by the transfer of energy from the large to the small scale (Kolmogorov scale), and the intraventricular flow regime was found to be on the edge between transitional-to-turbulent regime ($Re = 4000$) with swirling patterns [56]–[59]. Nonetheless, swirling patterns can occur also in non-turbulent flows. Several approaches can be used to accurately solve the smaller scales of the turbulent vortices. The Direct Numerical Simulation (DNS) approach resolves all the scales of the turbulent cascade (referred to as the gold standard) at the expense of a high computational cost due to the extremely fine grid. The Large Eddy Simulation (LES) resolves the larger scales and derives the effects of the unresolved smaller scales using sub-grid scale (SGS) models, which add artificial viscosity to dissipate kinetic energy. As consequence, the resulting flow field depends on the

used LES model and typically is less expensive and less accurate than a DNS. The prediction of the transition location with LES modeling is very sensitive to the choice of the Smagorinsky constant used for the calibration of the subgrid eddy viscosity. In this context, Germano et al. [60] proposed a dynamic subgrid-scale model that automatically reduces the subgrid eddy viscosity to zero in laminar boundary layers and near solid walls. However, Michelassi et al. [61] found that the comparison with the dynamic LES model and DNS results is valid only in qualitative terms. Monokrousos et al. [62] evaluated a relaxation-term model (ADM-RT) LES with linear feedback control that successfully damped linear and weakly nonlinear perturbations in a variety of wall-bounded shear flows. Hickel and Adams [63] developed an adaptive local deconvolution model (ALDM) to overcome the coupling between the truncation error of the numerical discretization and the conventional sub grid scale model.

The Reynolds-averaged Navier-Stokes equations (RANS) decomposes the velocity in the time-averaged component and the fluctuating one. The newly introduced variables require two additional equations to solve the N-S equations, typically called the $k-\varepsilon$ (suited for swirling cases, $20 < y^+ < 300$) or the $k-\omega$ model (suited for wall dominant cases, $1 < y^+ < 5$), where y^+ is a non-dimensional normal distance from the wall, which describes the height of the first cells near the wall. A low y^+ is needed to accurately characterize the gradient of velocity close to the wall [64].

2.4 Fluid domain mesh motion

2.4.1 The Arbitrary Lagrangian Eulerian (ALE) approach

The ALE approach combines the Lagrangian and Eulerian formulation in the implementation of mesh motion. In the Lagrangian formulation, the computational mesh follows the displacement of the fluid domain with the same velocity, whereas in the Eulerian formulation the grid is fixed in time and derives the fluid flow as the balance of mass and momentum (i.e. conservation) in each control volume (i.e. cell) of the fluid domain (Figure 2.1 a). In the ALE approach, the outer surface mesh follows the deformation of the fluid domain (image-derived or resulting of a fluid-structure interaction computation), whereas the internal nodes can move arbitrarily (Figure 2.1 b).

The grid velocity $\vec{w}$ has to be included in the N-S equations, therefore the conservation of mass and momentum become as in equations 2.9 and 2.10, where $\vec{w}$ is the velocity at the outer boundary of the control volume (in our case the LV endocardial wall), $\vec{n}$ is the outward surface unit normal of

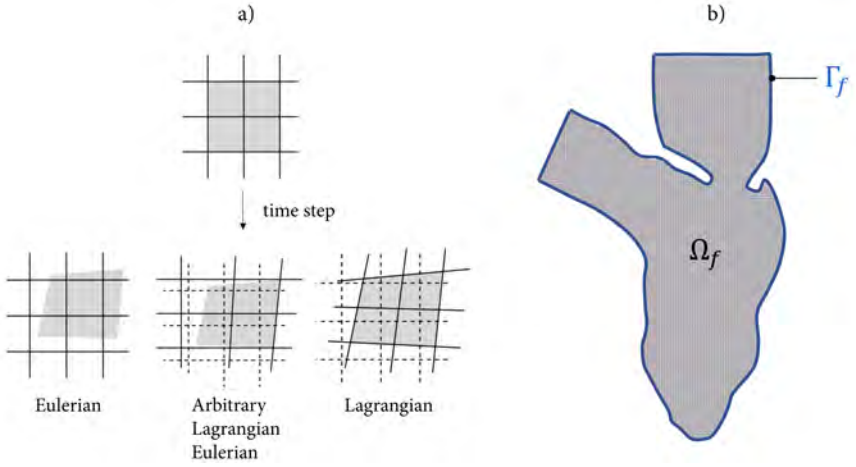

Figure 2.1: (a) Schematic of the different space discretization techniques (Eulerian, Arbitrary Lagrangian-Eulerian, Lagrangian methods) adapted from [65];(b) Schematic of a LV model based on the ALE approach, where the grid velocity is extended from the outer (Γ_f) to the inner grid (Ω_f).

the grid element. The cases $\vec{w} = 0$ and $\vec{w} = \vec{v_f}$ represent the Eulerian and the Lagrangian formulation, respectively.

$$\frac{\partial \rho_f}{\partial t} + \nabla \cdot \left(\rho_f \left(\vec{v_f} - \vec{w} \right) \right) = 0 \tag{2.9}$$

$$\rho_f \left(\frac{\partial \vec{v}_f}{\partial t} + \left(\vec{v_f} - \vec{w} \right) \nabla \cdot \vec{v_f} \right) = \nabla \cdot \overline{\sigma}_f + \vec{f}_f \tag{2.10}$$

The extension of the grid velocity from the outer boundary (Γ_f) to the inner grid (Ω_f) (see equation 2.11) can be performed via several smoothing algorithms, a.o the spring and the diffusion method.

$$\vec{w}_{\Omega_f} = \text{Ext}\left(\vec{w}_{\Gamma_f} \right) \tag{2.11}$$

The spring method handles the edges of the mesh elements as springs, with the length of the initial edge corresponding to the equilibrium state (i.e. $Force_{node} = 0$) of the spring and the new configuration of the nodes computed through Hooke's law. Usually, the quality of the grid is better preserved by choosing the spring constant inversely proportional to the edge length so that shorter edges become stiffer and more displacement occurs compared to the long edges [65].

The diffusion method is based on the Laplace equation, with the computation of the diffusion parameter based either on the wall distance, which preserves the quality of the mesh in the proximity of the moving walls, or the cell volume, which induces a larger deformation in the bigger sized elements [65].

With large deformations, the smoothing methods might not be sufficient to avoid highly skewed elements. In these cases, the remeshing option can be enabled to improve the quality of the inner volume mesh. Nonetheless, remeshing increases the computational time of the simulation, due to the interpolation process to update the mesh, and also numerical diffusion. The studies of Bavo et al. were based on the ALE approach implemented in Ansys Fluent, with the outer boundary of the grid velocity prescribed via User-Defined Functions (UDFs) and the inner boundary of the grid handled via smoothing methods and remeshing.

2.4.2 The Immersed Boundary Method

With the IBM technique, introduced by Peskin in 1972 [66] to study heart valves, the immersed boundaries (i.e. the LV endocardium and the mitral valve leaflets) are modeled as a set of non-conforming interconnected Lagrangian points that move on top of a fixed Eulerian Cartesian grid (Figure 2.2). The immersed bodies are accounted for as an added body force term ($\overrightarrow{f_f}$) in the N-S equation spread over the neighbor nodes of the Cartesian grid, with a resulting diffusive effect of the solution at the fluid interface.

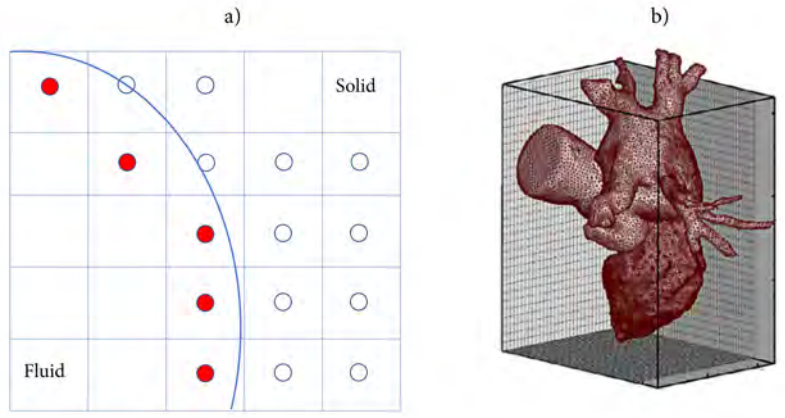

Figure 2.2: (a) Schematic of the immersed boundary method showing the delineation of the fluid domain boundary, adapted from [67]; (b) A left heart model immersed in a Cartesian volume grid using the IBM method, adapted from [67].

In FSI simulations, the interpolation of the fluid velocity from the incompressible fluid to a fully enclosed structure implies that the structure is divergence-free, which might not be a valid assumption for the structure.

2.4.3 The Smoothed Particles Hydrodynamics method

The Smoothed Particles Hydrodynamics (SPH) method is a mesh-free Lagrangian method used for FSI simulations that divides the fluid into a set of discrete moving particles, with the density of each particle matching either the fluid or the solid. It is suited to handle problems with complex boundary motion and to handle the valve coaptation. However, this method introduces a small degree of compressibility [65].

2.4.4 The Chimera Technique

In the Chimera (or Overset meshes) technique, the fluid domain is defined by one or several boundary layer component (or overset) grids embedded in a Cartesian fixed grid. This technique is particularly suited to handle cases with multiple moving components as the independent grids are free to move individually. Firstly, the interface between the background and overset grids is established through hole cutting, which disables the cells outside of the fluid region. In case that the fluid region does not involve grid motion, the disabled cells are removed permanently. Secondly, a domain decomposition coupling algorithm is used to obtain a continuous solution across the interfaces. In the literature, three different methods are available to handle hole cutting.

In the first approach (Figure 2.3, left), the hole cutting determines a gap between the two subdomains, successively filled with a conformal mesh that connects the subdomains. This strategy is typically used to attach an octree mesh (mesh that recursively subdivides the internal elements into eight octants) to the boundary layer meshes, and it provides two main advantages: (i) it is a pre-processing technique that can be isolated from the simulation code; (ii) the resulting mesh is conformal. The main disadvantage is that the generation of the conformal mesh might not be straightforward in case of different mesh size elements with the creation of extra nodes. Nevertheless, this can be overcome in case of meshes composed of elements with similar size by using a Shear-Slip Mesh Update Method (SSMUM) [69].

The second approach (Figure 2.3, middle) guarantees continuous variables and flow across the interfaces through transmission conditions, implemented as additional iterations to the original algorithm [70]. The implementation of the flow continuity depends on the PDEs and the physics of the problem.

The third approach (Figure 2.3, right) connects the overlapping meshes by creating gluing elements, with the following advantages: (i) it leads to

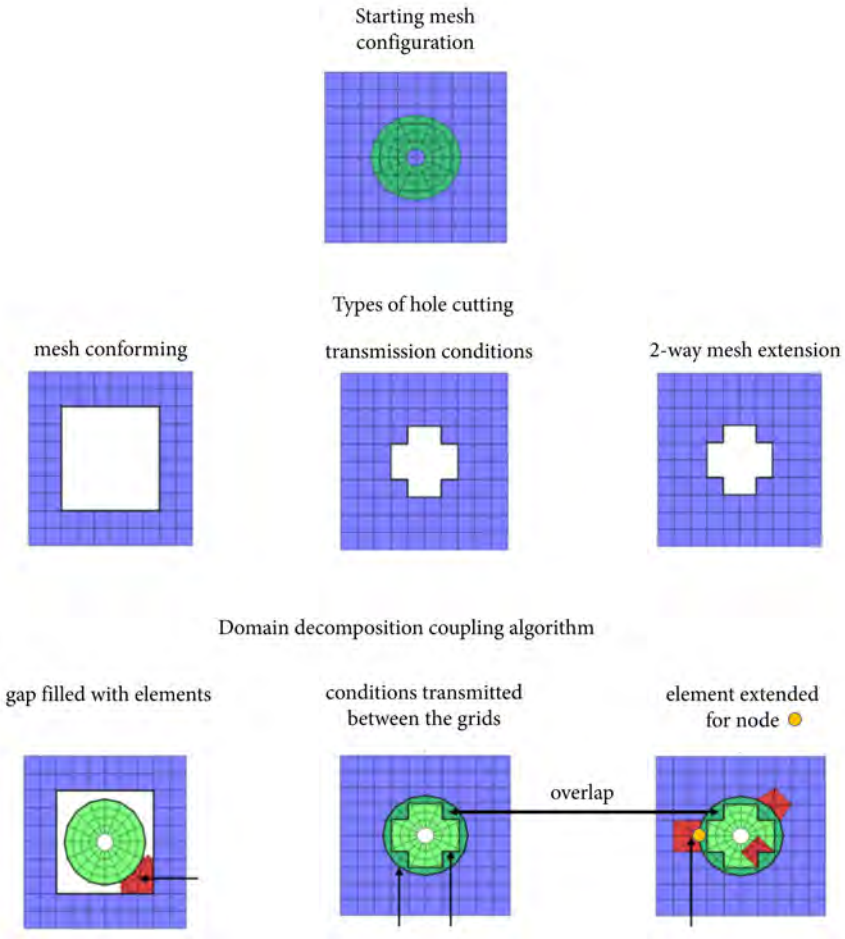

Figure 2.3: Different methods to handle the hole cutting of the Chimera approach. Adapted from [68].

implicit coupling; (ii) it can be applied to any PDE regardless of the physics; (iii) the method is inherently parallel.

We have set up our Chimera-based CFD model in Fluent 2019 R3® (ANSYS Inc., Canonsburg PA, USA) (Figure 2.4), in which the hole cutting relies on the exchange of the boundary information between these grids via interpolation of the flow variables until convergence is reached (hole cutting approach). The connectivity between the grids is established by classifying the cells into (Figure 2.4) (i) Dead cells, which lay outside the fluid domain; (ii) Solve cells, in which the flow equations are solved; (iii) Receptor cells, which receive the data interpolated from the donor cells of another mesh; (iv) Donor cells, which are a subset of the solve cells and send the data to the receptor cells.

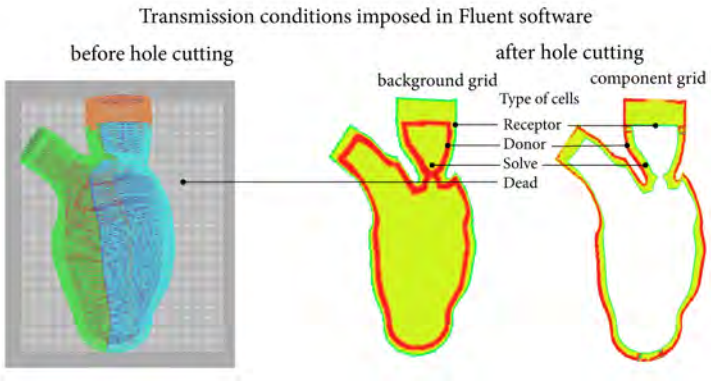

Figure 2.4: Type of cells of the Chimera method assigned in Fluent to exchange the conditions from the background and the component grid(s).

After setting the overset interface and the priority of the overlapping grids (the latter to enforce the computation of the variables on a particular grid), the definition of the type of cells and the connectivity consists of three steps automatically performed by the software. Firstly, the cells outside of the physical boundaries (i.e. wall) are marked as dead cells (hole cutting). Secondly, in case of a donor cell with a higher priority, the solve cells are converted into receptor cells and the unnecessary receptors are turned into dead cells (overlap minimization). Finally, the domain connectivity is established, with each receptor coupled with one solve cell (donor search). The grids are required to have at least four overlapping cells to ensure adequate connectivity and, after establishing the overset interface at every time step, the flow field is computed by solving the Navier-Stokes equations. Therefore, the Chimera technique can be considered as a mixture of the ALE and IBM approaches that allows overcoming the limitations of both techniques while exploiting the advantages, a.o. the accurate WSS computation and the implementation of large mesh motion.

2.5 LV patient-specific models: State of the art and LV modeling challenges

Several anatomical (a.o. the LV endocardium, the MV leaflets, the trabeculae) and fluid mechanical features (vortex formation, transitional-to-turbulent state) interplay to maintain a physiological LV flow state. Nevertheless, implementing all these features in a patient-specific CFD model is challenging from both a computational modeling and clinical imaging perspective.

Patient-specific CFD models have been used in several research studies as a fundamental research and design tool, to assess the impact of different features on the LV fluid dynamics, a.o. the natural [2], [71] and prosthetic MV [72], [73], the trabeculae carnae and the papillary muscles [74]–[76], and the transitional-to-turbulent state [57]–[59]. The studies by Seo et al. [71] and Bavo et al. [2] successfully simulated the paramount effects of the MV on the LV fluid dynamics (furtherly described) but encountered the following limitations: (i) Seo et al. [71] proposed a prescribed kinematic model of the MV that disregarded some patient-specific details - such as the high-frequency motion component and the change in the leaflet curvature - and the valve opening and closing was based on data from literature; (ii) Bavo et al. [2] showcased a patient-specific model limited to the diastolic phase due to the excessive mesh distortion. The main limitation regarding prosthetic MV is that the flow details are not typically incorporated in the hinge region [72], [73]. A patient-specific model of the LV that includes accurately the trabeculae and the papillary muscles is still not feasible due to the limited available resolution of the current *in-vivo* medical images [74], [76], however, when derived from *ex-vivo* scans, the small scale of the trabeculae conflicts with the large mesh motion of the LV endocardium, which is modeled as non-moving boundary [75]. Finally, Chnafa et al. [57]–[59] evaluated the transitional-to-turbulent state in multiple cardiac cycles with the MV leaflets that switch instantly from an open to a closed configuration (and vice versa).

As diagnostic tool, to detect the altered flow conditions induced by cardiac pathologies and to quantitatively define physiological flow-derived parameters: Bavo et al. [2] compared patients with dilated cardiomyopathy and impaired ejection; Nguyen et al. [27] compared diastolic dysfunction cases with controls disregarding the MV; Mittal et al. [67] proposed virtual Doppler cardiograms derived from cardiac simulations; Le et al. [77] investigated the features of the mitral vortex ring in a physiological LV disregarding the kinematics of the MV leaflets.

As evaluation tool of surgical procedures, a.o: Khalafvand et al. [78] assessed the effects of surgical ventricular restoration by comparing the pre- and post- operative intraventricular flow conditions without the MV;

Corsini et al. [79] virtually performed and evaluate the best surgical treatment between bi-directional Glenn and hemi-Fontan operations in patients with congenital single ventricle defect.

In the following sections, the state of the art and the main challenges regarding the above-mentioned features will be briefly discussed one by one to provide an outlook of the research regarding patient-specific CFD modeling of the LV. Lastly, the studies of Bavo et al.[1], [2], developed within our research group, had significant impact on the current dissertation and can be referred to as the starting point of this PhD thesis. The last part will therefore focus on the details of that work, the unsolved challenges and the differences with our approach.

2.5.1 The LV endocardial motion

The irregular morphology and the large deformation of the ventricular endocardial wall is one of the main challenges to tackle in the set-up of a CFD LV model. The first computational models of the LV were typically based on idealized 2D or 3D geometrical models [80]–[83] (i.e. a truncated ellipsoid) with the endocardial motion prescribed analytically. Successively, the outstanding progress of both clinical imaging techniques and computational maturity introduced the concept of patient-specific CFD simulations to replicate both the morphology and the kinematics of the left ventricle.

The 4D (3D + time) patient-specific LV configurations spanning one cardiac cycle can be easily assigned by using meshes of the endocardium that share the same topology and connectivity (i.e. 1-to-1 vertex correspondence). 4D LV meshes with 1-to-1 vertex correspondence can be useful also for the temporal interpolation needed to increase the temporal resolution of medical images up to the one needed in computational simulations. Typically, the 4D LV endocardium is retrieved from clinical images (MRI, CT, US) using deformable or Statistical Shape Models (SSM).

There are several deformable models, but they require two steps to set them up. Firstly, the LV is (manually) segmented in one time-instant of the cardiac cycle, usually corresponding to the end-systolic configuration. Secondly, the segmented mesh is automatically deformed to match the remaining configuration spanning one cycle. Among the deformable models, several approaches have been used. Wang et al. [84] relied on a meshless point-clouds model. Bavo et al. [1] combined deformable models with multi-atlas joint label fusion. Skrinjar and Bistoquet [85] used a pre-meshed sphere to target the segmented 3D LV meshes. Gao et al. [86] used a snake-based semi-automatic segmentation method to build high-resolution meshes including the papillary muscles and the trabeculae. Lastly, Mittal relied on a diffeomorphic registration algorithm to map a template LV surface mesh onto

the patient-specific target at each keyframe [67]. When using deformable meshes, related key issues are the sensitivity to the initialization process with manual interaction, the poor convergence associated with noisy images, and the considerable errors in case of large deformations between neighboring frames.

On the other hand, the SSMs are based on a dataset atlas and also require two main steps. Initially, the statistical model is trained with datasets to define the morphology and the variability of the structure of interest, and, successively, it is used to derive the structure in a new imaging dataset. Among the SSM approaches, both Sun et al. [87] and Zhu et al. [88] used the combination of shape knowledge and dynamic information to account for cardiac shape variability, while Besbes et al. [89] used a control points representation of the LV to be deformed into other images. The main advantage is that SSMs can rely on a large number of cardiac-atlases based on physiological and pathological conditions, even though the pathologically-induced alterations could require specific model training for every pathological condition. Furthermore, manual training is time-consuming and can lead to inconsistencies, making SSMs a perfect application for machine learning methods. In this regard, Mihalef et al. [90] modeled the left cardiac heart with the valves from multiple 4D CT datasets using a machine-learning algorithm with a claimed precision of 90%.

We found only two studies (Schenkel et al. [91] and Doenst et al. [92]) that created structured hexahedral meshes of the LV by semi-automatically projecting the vertexes of a tube-like base grid onto the segmented surface. Nonetheless, the authors report that the quality of the mesh could not be preserved with meshes exceeding 400 000 elements. Lim et al. [93], [94] built 4D patient-specific meshes of the left and right heart proposing tetrahedral meshes based on the manual delineation of the contours across all slices through the cardiac cycle, resulting in a time-consuming operation.

A graphical representation of the LV patient-specific models developed by Lim et al. [94], Schenkel et al. [91], and Gao et al. [86] is reported in Figure 2.5.

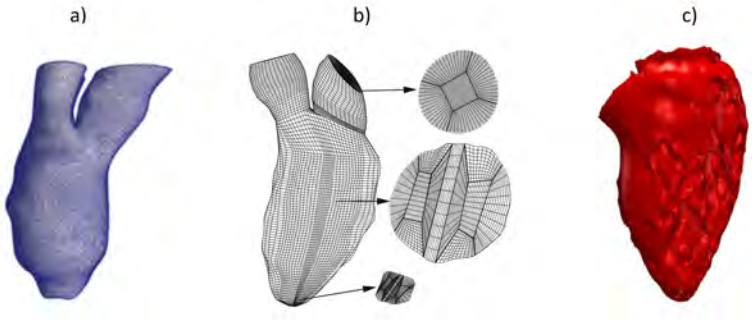

Figure 2.5: Examples of patient-specific 4D LV endocardial models: (a) Lim et al. [94] developed a smooth tetrahedral mesh of the LV endocardium; (b) Schenkel et al. [91] generated a fully hexahedral mesh; (c) Gao et al. [86] partially included also the trabeculae carnae and the papillary muscles.

Of note is that most of the kinematic LV models usually disregard torsion due to the intrinsic difficulties in accurately tracking it from medical images, as confirmed by the lack of validation of the tracking algorithm proposed by Conti et al. [54], which is based on the local curvature and the nearest neighbor search. Only a few studies implemented the torsional motion in CFD models of the LV [95], [96], and only Vasudevan et al. [96] evaluated the impact of torsion on the LV fluid dynamics, finding no major impact on the intra-ventricular flow field.

In this dissertation, we used a strategy based on isoparametric transformations for the LV model that resembles a deformable model (please refer to Chapter 3 and Chapter 4) to take into account the torsional motion of the LV.

2.5.2 The MV annulus and leaflets

The morphology and kinematics of the MV leaflets play a crucial role in the development of the diastolic asymmetric vortical patterns, which is a key feature in maintaining the physiological wash-out and energetics inside the ventricular chamber. The impact of the MV on the LV intra-ventricular flow pattern was also confirmed using patient-specific CFD modeling (Seo et al. [71] and Bavo et al. [2]). The findings by Seo et al. [71] suggest that the mitral valve enhances the circulatory flow pattern in the ventricle and increases the intensity of the apical flow, resulting in an improved apical washout and mixing of the ventricular blood. Similarly, Bavo et al. [2] found that the presence of the MV enhances the vortical patterns and allows the vortex ring to better penetrate towards the apex.

In the context of a CFD model, the MV motion can be computationally implemented either via a prescribed kinematic model or a Fluid-Structure

Interaction (FSI) model, in which the motion at a specific time is the result of the pressure field computed at the same time frame.

The first models of the MV aimed to mimic the functionality of the valvular orifice alone, as they were based on an on-off approach [97], [98] or on a time-varying planar orifice approach [91], [92], [99], hence disregarding both the configuration and kinematics of the leaflets. Successively, these features have been implemented with different degrees of accuracy leading to patient-inspired or patient-specific MV models.

Among the patient-inspired MV models: (i) Chnafa et al. [57]–[59] segmented the moving MV annulus from 4D CT scans and modeled the MV leaflets as a thick continuous elliptical shape which instantaneously switches between the open and the closed configuration; (ii) Seo et al. [100] defined the morphology of the MV leaflets based on the anatomical measurements obtained by Ranganathan et al. [101], and assigned a specific angle profile for the rigid rotation of the anterior (α_{AL}) and posterior (α_{PL}) leaflets.

Referring to the patient-specific MV models: (i) Mihalef et al. [90] modeled the MV and the left cardiac heart using machine-learning algorithms from multiple 4D CT datasets; (ii) Bavo et al. [2] segmented both the LV and MV kinematics from 4D transesophageal echocardiographic images combining deformable models with multi-atlas joint label fusion.

The advantage of patient-specific MV models over patient-inspired ones lies in the more reliable tracking of local fluctuations and curvature changes of the leaflets. Nonetheless, the thin leaflets and their highly impulsive kinematics pose challenges to choose an adequate imaging modality able to capture the opening/closing phases.

A graphical representation of the MV models developed by Chnafa et al. [58], Bavo et al. [2], and Seo et al. [71] are reported in Figure 2.6.

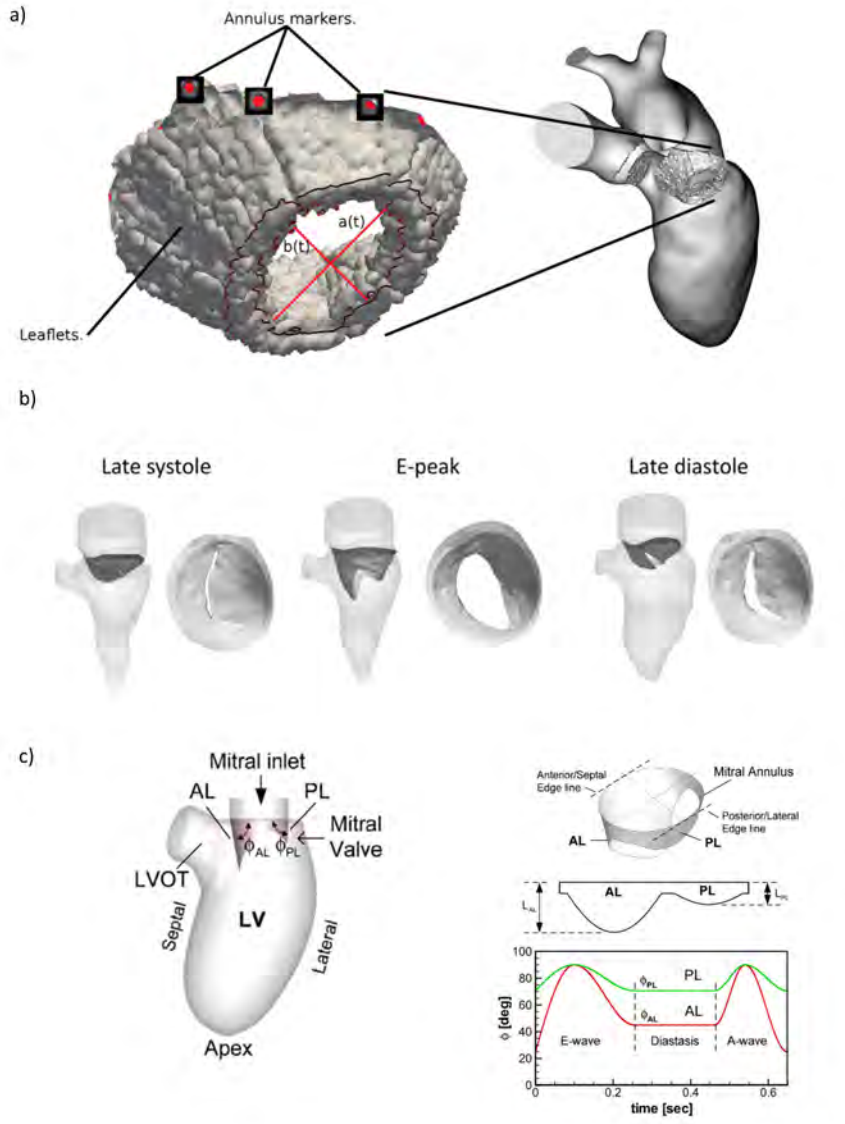

Figure 2.6: Graphical representation of the MV models developed by (a) Chnafa et al. [58], Bavo et al. [2], and Seo et al. [71].

In this dissertation, we applied a patient-inspired MV model, in which the MV leaflets were segmented at the A-wave peak from a radial MRI dataset. The motion was patient-inspired, due to high uncertainty linked with the highly impulsive leaflets and motion artifacts. More details regarding the kinematic model of the MV are reported in Chapter 5.

2.5.3 The transitional-to-turbulent flow state

Identifying the precise nature of the flow regime inside the Left Ventricle (LV) is non-trivial. In physiological cases, the Reynolds number is around 4000 and the highly transient dynamicity of the LV does not seem to allow the Kolmogorov cascade enough time to establish, resulting in a problematic definition of intracardiac turbulence. Few studies (Domenichini et al. [56], Chnafa et al. [57]–[59]) found out that several regimes occur, evolving from laminar to transitional, and (briefly) turbulent flow at the diastolic E peak. Domenichini et al. [56] investigated the impact of different conditions (such as the eccentricity of the inlet profile, the Stokes number and the Strouhal number) on the fluid dynamics of a predefined LV, whereas Chnafa et al. [57]–[59] studied the hemodynamics inside a patient-specific LV model using LES modeling.

The pioneering study about the LV flow state has been performed by Domenichini and Pedrizzetti [56] who reported a weak turbulent flow in a healthy left ventricle model, even though the LV model shape and motion were defined analytically. Later, also Chnafa et al. [57]–[59] found that the transitional-to-turbulent flow of the LV induces high-frequency flow fluctuations in a patient-specific physiological LV model.

Later, Chnafa et al. [57]–[59] investigated the LV transitional flow using a Large Eddy Simulation (LES) approach to model the smaller subgrid scales because a Direct Numerical Simulation approach would require a too fine grid and the Reynolds Averaged Navier-Stokes (RANS) approaches are not applicable due to the not fully developed neither ergodic turbulence. In the referred study [59], Chnafa et al. simulated 35 consecutive cardiac cycles and they mentioned that the cycle-to-cycle variation was still noticeable at the last cycle (Figure 2.7). This finding has important implications in the hypothesis typically assumed in the phase-average Cardiac Magnetic Resonance (CMR).

Even though there is a high variability of the LV flow from cycle-to-cycle due to the intraventricular quasi-turbulent flow, most publications will assume that the flow is repeatable after a few cycles. In this regard, we considered cycle-to-cycle variations in our simulations and simulated six cardiac cycles. Our study mainly aimed to address the challenges related to the mesh motion (both the LV and the MV), and the limited opening angle of the MV (introduced to solve some technical issues related to the use of

the Chimera technique) resulted in an artificial impaired opening of the MV that led to a Reynolds number of 10 000 in correspondence to the MV orifice at the diastolic E-peak. As these peak values of the Reynolds number are only reached during a few time steps, in our simulations we used the laminar flow assumption. The use of a turbulence model that can handle the different flow regimes and the transitions between them would be a relevant further development, however, following Chnafa et al. [57]–[59], we believe that the main large-scale hemodynamic features (such as jets, main vortices, and ejection) can be assessed even with the laminar flow assumption.

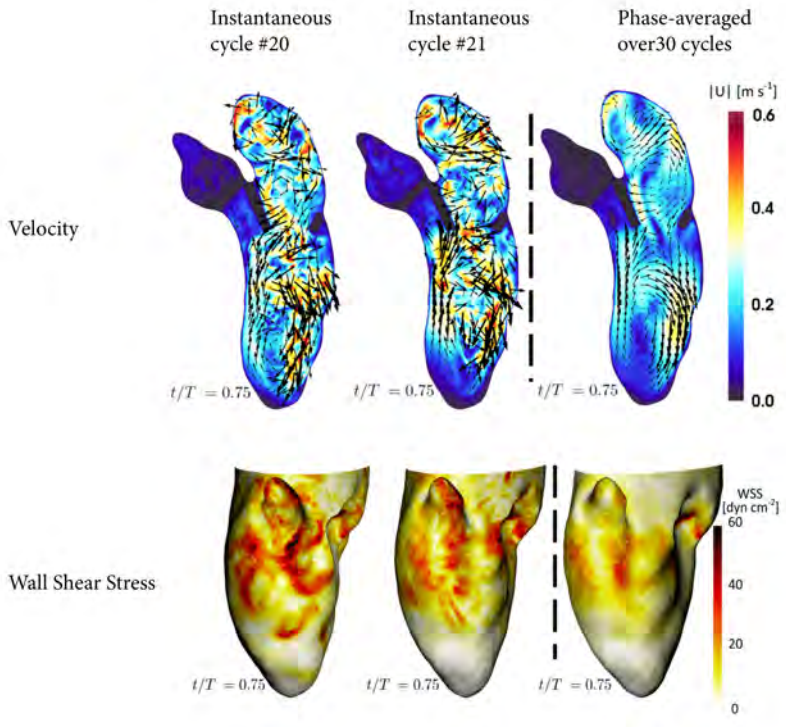

Figure 2.7: Cycle-to-cycle variation assessed by Chnafa et al.[59] between the 21^{st} 22^{nd} cardiac cycle in the velocity magnitude (m/s) and the wall shear stress (dyn/cm^3).

2.5.4 The trabeculae carnae

The small geometrical scale to accurately characterize the trabeculae carnae poses multi-disciplinary challenges in terms of imaging modality acquisition, meshing strategy, and motion implementation. Particularly, an accurate mesh model of the trabeculae with features on the mm scale can be hardly coupled with the large deformation of the endocardium. From a dynamic mesh motion perspective, this represents a nearly impossible challenge because the motion of the finely trabeculated endocardial mesh should not exceed the mesh element size (in the mm scale) within one time step.

Few studies tried to evaluate the influence of the larger-scale structures composing the trabeculae and the papillary muscles on the intra-ventricular flow [74], [76] or finely scanned the ex-vivo trabeculae implementing them in a CFD simulation which disregards the motion of the LV endocardium [75].

Despite differences among studies, they all agreed on that the trabeculae enhance the disruption of the two main vortices into smaller structures with increased vorticity. Among the cited studies, only Vedula et al. [74] (Figure 2.8) noticed a deeper penetration of the inlet jet. Sacco et al. [75] proposed to include the trabeculae into smoothed ventricular geometries as a porous layer in correspondence with the LV endocardial wall. In this PhD thesis, the trabeculae carnae and the papillary muscles were disregarded from our analysis due to the inadequate slice thickness of our cine-MRI short-axis imaging data (8 mm). However, implementing the trabeculae carnae represents an interesting further development of our model since the Chimera technique should allow to represent them as an additional component grid.

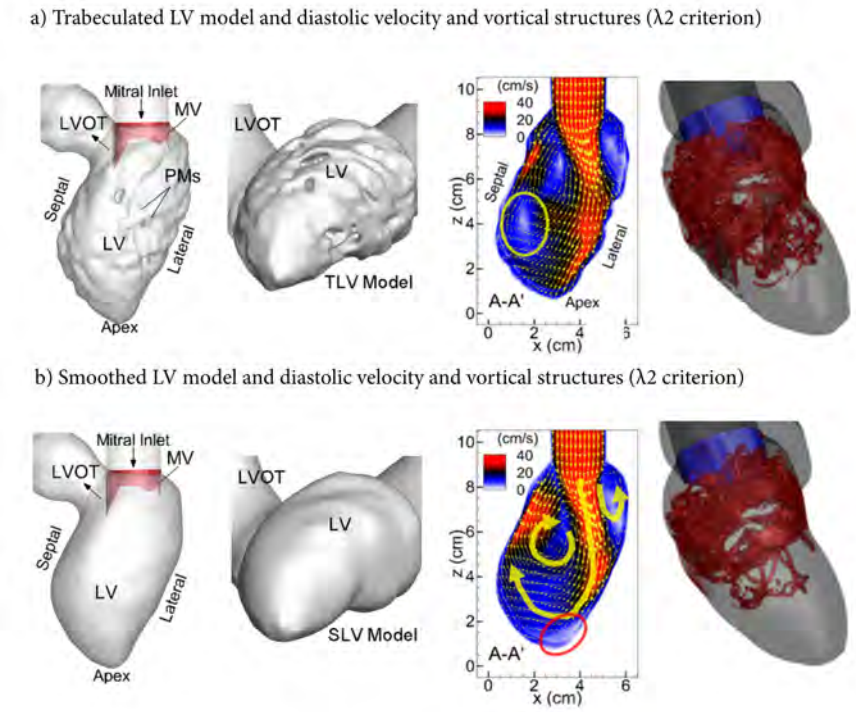

Figure 2.8: (a) Geometrical differences between the trabeculated (top) and the smoothed (top) LV model; (b) The trabeculae carnae induce a higher velocity magnitude (m/s) in the apical and an enhanced distruption of the vortices during diastole.

2.5.5 The blood fluid model

Blood is composed of liquid (plasma) and particles (blood cells) that induce non-Newtonian characteristics for a shear rate below 100 s^{-1}. In the cardiovascular system, such condition exists in regions of oscillatory and recirculating blood flow especially during the deceleration phases of the cardiac cycle with quasi-null velocity and velocity gradients. In this regard, Doost et al. [102], by comparing different non-Newtonian models with a Newtonian model of the LV, noticed differences in the flow patterns, the size of the vortices, and the maximum WSS. Even though the blood is assumed Newtonian in the majority of the CFD studies about the LV, these findings demonstrated that the Newtonian assumption for the blood inside the LV cavity may not be valid due to the pulsatility, recirculation, and low shear rate. In this thesis, with the technical focus on the implementation of the Chimera technique to the moving LV and MV, we assumed Newtonian properties for the blood. Nonetheless, the non-Newtonian model represents an interesting further development.

2.5.6 Starting point: the patient-specific CFD model of the LV by Bavo et al.

The work performed by Bavo et al. [1], [2] on the LV modeling encompasses (i) the definition of the workflow behind the patient-specific CFD model and (ii) the comparison of the intraventricular flow field for three clinical cases built through the referred workflow. The proposed workflow, typical of any patient-specific CFD model, provided us some computational tools used as a starting point for this dissertation.

At the same time, the work of Bavo et al. also had some intrinsic limitations, that necessitated another approach. In Bavo et al. [1], [2] the segmentation of the LV and MV from 3D ultrasound images was performed through the algorithm developed by Pouch et al. [103] and allowed for the generation of standalone triangular surface meshes of the LV and MV with 1-to-1 vertices correspondence. After fusing the LV and the MV meshes the internal fluid mesh was created, resulting in a tetrahedral LVMV mesh. The segmented LV and MV surface meshes were temporally interpolated and used as reference meshes to deform the outer boundary of the LVMV volume mesh, using an ALE approach. Both these operations were handled directly in Fluent with customized User Defined Functions (UDFs). As boundary conditions of the CFD model, the inlet was set at constant pressure (0 mmHg) throughout the entire cardiac cycle, an on-off condition was imposed at the outlet, with a pressure condition of 100 mmHg during systole and a wall condition during diastole. An artificial gap was introduced in the MV leaflets during systole due to the difficulties for the ALE approach to handle the fluid domain separation resulting from the coaptation of the MV valve during systole. Furthermore, the reverse flow during systole was avoided by adding a source term in the Navier-Stokes equation in the cells representing the valve orifice.

The comparative study between the three different clinical cases provided two important considerations (Figure 2.9): (i) the influence of the LV shape and the MV presence led to different flow features depending on the pathology; (ii) the pattern and the evolution of the vortical structure was influenced by the valvular orifice and the ventricular shape.

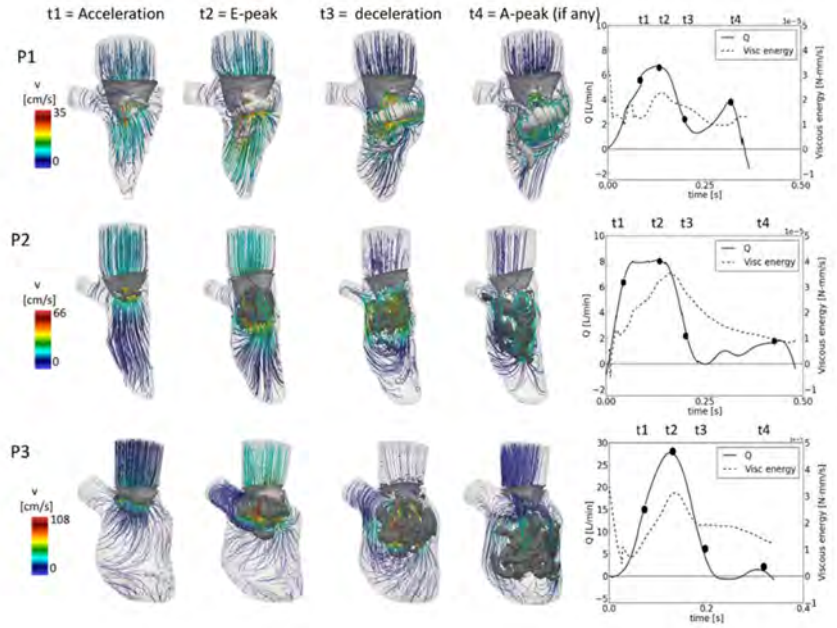

Figure 2.9: Intraventricular vortex visualization (λ_2) and velocity streamlines at four relevant time-points simulated by Bavo et al.[2]. P1 = Pathological LV case with normal size, hypokinetic walls and concentric hypertrophy; P2 = Pathological LV case with normal size and impaired relaxation: P3 = Pathological dilated LV case with global diastolic dysfunction and severe hypokinesis.

The two studies by Bavo et al. [1], [2], however, also highlighted the limitations of the developed workflow, which was too specifically tailored to solve that specific problem and was virtually impossible to apply within a workflow aiming to augment clinical images with CFD data on a larger scale. As such, the work of Bavo et al. defined the technical challenges that we aimed to solve within this dissertation.

A first important limitation was that the numerical calculations were limited to one cardiac cycle or even to the diastolic phase due to excessive mesh distortion, which led us to change the meshing strategy. In this regard, we introduced three main changes. Firstly, we defined our semi-automatic algorithm to build 4D patient-specific BL meshes of the LV with 1-to-1 vertices correspondence.

Secondly, we decoupled the temporal interpolation from the CFD solver

so that both the mesh generation and the quality of the 4D BL meshes could be tested before setting up the CFD case in Fluent.

Thirdly, we used the Chimera technique instead of the ALE approach to benefit from the advantage of handling moving mesh problems with multiple component grids.

The resulting improved numerical reliability allowed us to simulate multiple cardiac cycles and to perform particle tracking. Additionally, we defined an algorithm to implement the torsional motion, typically disregarded, in our patient-specific CFD simulation and evaluated the influence on the intraventricular fluid dynamics.

II

CFD model of the contracting LV using the Chimera technique: impact of torsion on intraventricular hemodynamics

Chapters

Chapter 3

Patient-specific boundary layer meshes of the 4D LV endocardium

This chapter introduces a semi-automatic morphing tool focused on the generation of structured high-quality 4D surface meshes (3D in space + time) with 1-to-1 vertex correspondence from medical images, as essential to impose the patient-specific LV motion of the LV in a Computational Fluid Dynamics simulation. This chapter is based on the paper From 4D medical images to 4D structured mesh models of the Left Ventricular endocardium for patient-specific simulations, *BioMed Research International*, vol. 2018, Article ID 7030718, 14 pages, 2018.

3.1 Introduction

Cardiovascular disease (CVD) is the leading cause of death, with a worldwide mortality of 31% [104] and even 40% within the European borders [105]. In absolute terms, 17.5 million people die each year in the world from CVDs. Not surprisingly, numerous studies focused on a better understanding of CVDs including hypertension, atherosclerosis, Coronary Heart Disease (CHD), stroke, Congestive Heart Failure (CHF), and congenital and rheumatic heart disease. The clinical diagnosis of CVDs most often relies on different imaging modalities such as angiography, MRI, Ultrasound (US), and CT with the choice depending on the pathology under investigation.

Thanks to the massive development of computational resources, in the last 20 years there has been a growing interest in computational modeling such as Computational Fluid Dynamics (CFD) and Finite Element (FE) and Fluid-Structure Interaction (FSI) analysis. Nowadays, applied biomechanical research has moved into the direction of medical and patient-specific applications; thus the coupling between clinical images and computational modeling can play a fundamental role in this regard. Several examples of commercially available simulation-based services can be mentioned: Medis [106] and HeartFlow [107] use CFD as diagnostic tool for Fractional Flow Reserve (FRR) by means of angio-based and CT-based images, respectively, while from a treatment perspective FluidDA [108] and FEops [7], [109] developed commercial tools to support clinicians in respiratory disease cases and in TAVI applications. Lastly, SIMULIA created an integrative predictive biophysical model of the human heart to extract clinical parameters and guide device design and treatment planning in cardiac diseases [110].

While vascular pathologies can - depending on the specific application - be addressed using models not accounting for the dynamic expansion and recoil of the wall, modeling of the flow or the mechanics of the heart chambers cannot disregard the large motion of cardiovascular structures. Indeed, the combination and integration of computational modeling and clinical images become even more essential. Among the 4 chambers, the left ventricle (LV) is the pump responsible for the systemic circulation and a better knowledge of its fluid dynamics can help to understand pathologies such as hypertrophy, valvular leakages, cardiomyopathy, and correct phenotyping of heart failure. In this context, the general final target of this work is to develop a pipeline that allows setting up patient-specific CFD models of the LV that are able to quantify the swirling flow inside it, which could help the clinicians in diagnosing, phenotyping, and finding the best therapy. The CFD modeling of a heart chamber, such as the LV, faces important technical obstacles such as accounting for endocardial motion and valves kinematics. The rapid and large motion and deformation of these features can easily lead to very distorted elements in the mesh that is used for the CFD calculation and affect its accuracy or in the worst case scenario lead to negative volume meshes and, thus, failure of the simulation. Despite a lot of works focusing on 4D (3D space + time) LV segmentation (mainly based on deformable models and Statistical Shape Modeling (SSM)), to the best of our knowledge there is still a lack of methodologies for high quality structured meshing of a 4D dataset for subsequent CFD analysis.

Among the deformable models, one can cite the studies by Wang et al. [84] and Gao et al. [86] who reconstructed the 4D LV, the former by meshless point-clouds and the latter including anatomical details such as the papillary

muscles (PMs) and the trabeculae. Bavo et al. [1] reproduced the LV with a semiautomated image segmentation and the mitral valve (MV) [103] with a combination of multi-atlas joint label fusion and deformable models. Skrinjar and Bistoquet [85] built meshes from segmented 3D MR images mapping a pre-meshed sphere to the target surface of the segmented object with the mapping operation defined by the gradient field of the solution of the Laplace equation between the sphere and the surface of the object. Among the SSM approaches the studies of Sun et al. [87] and Zhu et al. [88] used the shape knowledge combined with dynamic information to account for cardiac shape variability, while Besbes et al. [89] used a control point representation of the LV prior to deforming other images.

When using deformable meshes derived from 4D data sources, related key issues are sensitiveness to the initialization process with manual interaction required for the first step, poor convergence for noisy images, and large errors associated with large deformations between neighboring frames.

As far as we know, only two studies (Schenkel et al. [91] and Doenst et al. [92]) based their CFD analysis in the LV on structured hexahedral meshes. These were semiautomatically created by projecting the vertexes of a tube-like base grid onto the segmented surface. No detailed information about the followed strategy was reported in the paper. In Schenkel et al. [91], the hexahedral mesh is generated following the same strategy but for the whole heart. Nonetheless, the authors report that the quality of the mesh could not be preserved with meshes exceeding 400,000 elements. Lim et al. [93] realized a 4D patient-specific mesh of the right heart from segmented MRI contour lines with 1-to-1 vertex correspondence in 2013 and, in the following year, the method was extended to both the left and right heart [94]. In both the studies, the delineation of the contour lines had to be drawn across all slices through the cardiac cycle, resulting in a time-consuming operation. Furthermore, only triangular surface meshes are presented in these studies, while in the CFD community the use of hexahedral or hybrid meshes with a prism layer is preferred for a more accurate Wall Shear Stress (WSS) evaluation [111]. Consequently, we believe that there is still a lack of practically feasible methodology to derive high-quality structured meshes from 4D clinical cardiac imaging datasets with 1-to-1 vertex correspondence and this study attempts to fill this gap. The nodal correspondence between the 4D meshes is essential in a CFD set-up with moving boundaries to assign the endocardial wall displacement as the displacement of each node that composes the mesh and avoids problems of mesh quality that could be induced by spatial interpolation schemes. Furthermore, as a result of temporal interpolation, the nodal correspondence of the 4D high-quality meshes allows us to generate high-quality intermediate meshes and overcome, in this way, the

low temporal resolution of 4D clinical imaging datasets for a CFD software environment. In the following sections, the steps of the newly proposed mesh generation methodology are described in detail, starting from the general strategy in section 3.2.3, as well as its applications on the different parts that compose our ventricle mesh (see sections 3.2.3.1, 3.2.3.2 and 3.2.3.3). In order to demonstrate the versatility and efficiency, it is tested with the three most used 4D cardiac imaging modalities (CT, US, and MRI). Lastly, the quality and the accuracy of the different meshes are analyzed.

3.2 Methods

The high-quality mesh tool will be tested on three different types of 4D imaging datasets (US, MRI, and CT) coming from three different patients in order to prove the versatility and the applicability of the method. The segmentation procedure is differently managed depending on the availability of the segmentation software (Figure 3.1), while the high-quality meshing scripts have been developed in PyFormex, a python-based open-source software.

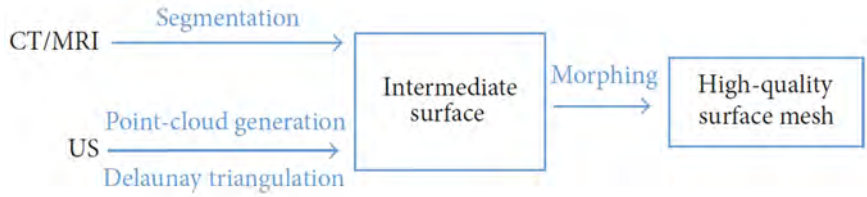

Figure 3.1: The workflow used for the three different 4D datasets is reported: CT and MRI datasets are segmented by using the Materialise Mimics CT Heart tool, whereas the US images are segmented via an in-house code developed in PyFormex, a python-based software environment. The morphing is performed with algorithms that rely on isoparametric transformations.

3.2.1 Datasets

All images were acquired as part of standard clinical care in 3 different hospitals. Data were anonymized and all subjects gave informed consent for the use of their data for this study. The 4D MRI dataset was acquired along the short

axis of the ventricle with an initial slice thickness of 10 mm. Due to the high slice thickness the data were interpolated by means of trilinear interpolation resulting in a slice thickness of 2 mm, whereas no interpolation was used for the US and CT datasets. The voxel dimensions are 1x1x1 mm, 1.641x1.641x2 mm and 0.352x0.352x0.75 mm for 4D US, 4D MRI and 4D CT, respectively. For each imaging modality, data spanning one cardiac cycle were available with data at 23 time instants for 4D US, 30 for 4D MRI, and 15 for the 4D CT.

3.2.2 Segmentation

In the case of the 4D CT dataset the segmentation was performed straightforward using the Materialise Mimics CT Heart tool for heart chamber segmentation for each of the 15 time frames of the cardiac cycle. Also each frame of the 4D MRI dataset (30 time frames) was initially segmented by means of the Materialise Mimics CT Heart tool, but due to the low through-plane spatial resolution manual corrections were needed. For the CT and MRI datasets also other open-source software (such as 3D Slicer) could have been used, but to speed up the process these other ways were preferred. Conversely, as far as we know there are no available opensource software able to visualize and segment 4D Ultrasound datasets. For this reason, we developed our own algorithm compiled in PyFormex, a python-based in-house software environment, to manually segment this dataset. The workflow of the algorithm can be described in 5 steps:

1. Load the 4D US dataset and define the axis of the dataset along which the camera is rotated (Figure 3.2 a);
2. Manually place points in the view to delineate the LV endocardium (Figure 3.2 b);
3. Rotate every 5 or 10 degrees around the rotating axis and repeat step 2 until the complete volume of the chamber is covered (Figure 3.2 c);
4. Save the point-cloud of the LV for each time frame (time frame can be manually chosen by rolling a scroll-bar).
5. As outcome of this process, N left ventricle point clouds are obtained, where N is equal to the number of time points where data is available and the surfaces are obtained by means of Delaunay triangulation.

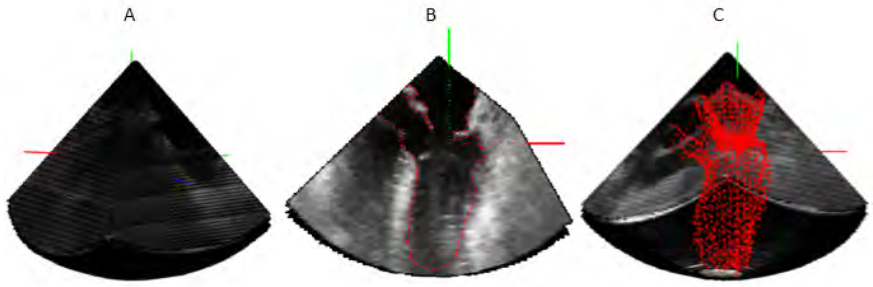

Figure 3.2: Steps of the algorithm to reconstruct the 4D point-clouds from the 4D US dataset:(a) definition of the rotating axis; (b) placement of the points in a view of the US cone; (c) resulting point-cloud distribution of the LV.

3.2.3 High quality mesh generation

In this core section, the strategy behind the generation of the high quality structured mesh is described and implemented as a semiautomatic process to the different parts that compound the LV (Figure 3.3): LV sac, Y-junction , and connection between the LV sac and Y-junction in subsections 3.2.3.1, 3.2.3.2 and 3.2.3.3, respectively. The tool is described for the CT dataset, but it is generic and has been used for the processing of all datasets in this paper. We chose to detail the method using the CT dataset as this is the most complex dataset that includes the LV as well as the left atrium, aorta, and the valvular planes. As it is impossible to mesh these structures as a whole, 3 subdomains are created: (i) the ventricular sac, (ii) the atrium and aorta, and (iii) the zone connecting both.

After discerning the general strategy of the high-quality mesh generation, it will be explained how these 3 subdomains can be meshed using a morphing toolkit specifically designed for these 3 anatomical regions. The general strategy is to cover the segmented surface of the 4D dataset, which typically has a non adequate quality of the surface mesh, with a combination of patches that have the desired mesh topology by means of isoparametric transformations. The application of an isoparametric transformation requires the definition of the following inputs:

- The patch: this is the object (2D or 3D) to which to apply the isoparametric transformation. In our case, the patch is a structured quadratic

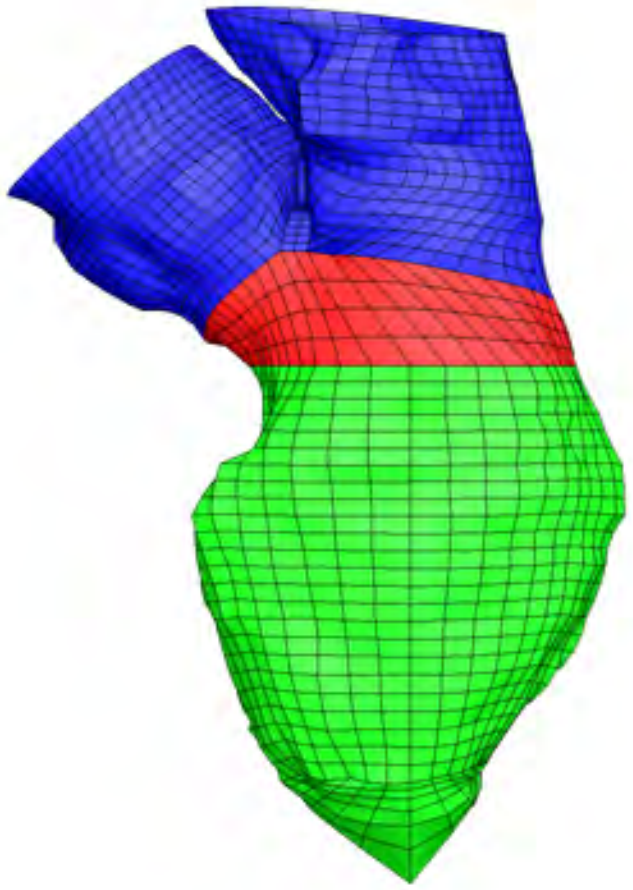

Figure 3.3: LV divided into three parts: LV sac (in green), Y-junction (in blue), and connection between the two (in red) [4D CT dataset].

surface mesh defined in the x-y plane (2D) (3.4 a), but it could be of any shape (a triangular mesh, a star, an asterisk, etc.).

- The initial control points (CPs): these are defined on the patch to be transformed (Figure 3.4 b, in blue). Their number (equal to the number of the final CPs) depends on the type of transformation.
- The final CPs: these are the points, numbered identical as the initial CPs, onto which the initial CPs will be transformed (Figure 3.4d, in red). In other words, their location will define the shape of the resulting patch.

- The type of transformation: this sets the type of relation between the initial and final CPs. For example, a quadratic transformation can have 4 CPs (in the corners of the patch), 8 CPs (in the corners and in the middle of the edges), or 9 CPs (with the extra CP located in the center of the face) (Figure 3.4).

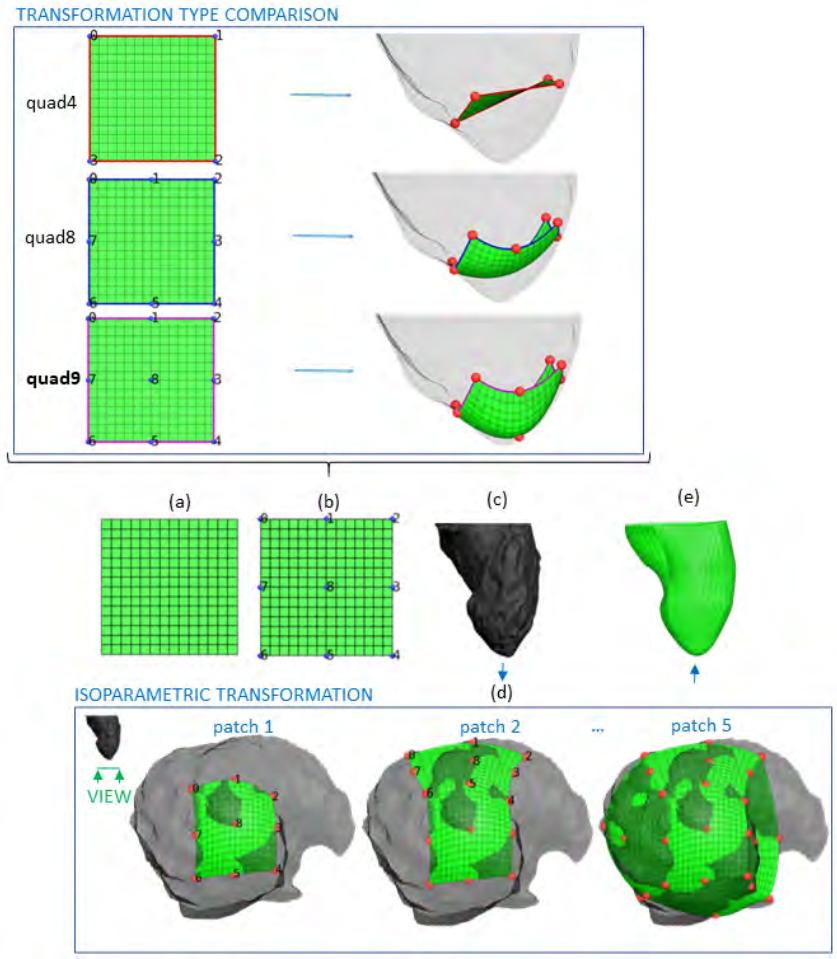

Figure 3.4: Example of the strategy used to reconstruct the target geometry by means of isoparametric transformations: (a) definition of the patch in the x-y domain used to cover the target geometry; (b) definition of the initial control points (CPs) of the isoparametric transformation; (c) initial geometry to be mapped; (d) placement of the final CPs onto the target geometry and sequential application of the isoparametric transformations; (e) final mapped geometry. The top part of the figure shows how the same patch is differently deformed using different isoparametric transformations (quad 4, quad 8, and quad 9).

In the quad 4 transformation the edges of the transformed object follow a linear equation and in the quad 8 and quad 9 a quadratic one [21]. In our case, a quad 9 transformation is used because it allows a more accurate adhesion to the irregular structures that compose the LV endocardium (as visible in the top panel of Figure 3.4). To be more specific, in case of quad 9 isoparametric transformation, the transformation of a point $(x, y, z = 0)$ to a new point (x_1, y_1, z_1) is described by the 2^{nd} order Lagrangian interpolation polynomial in x, y reported in equations 3.1, 3.2 and 3.3.

$$x_1 = a_0+a_1\cdot x+a_2\cdot y+a_3\cdot x^2+a_4\cdot y^2+a_5\cdot x\cdot y+a_6\cdot x^2\cdot y+a_7\cdot x\cdot y^2+a_8\cdot x^2\cdot y^2 \quad (3.1)$$

$$y_1 = b_0+b_1\cdot x+b_2\cdot y+b_3\cdot x^2+b_4\cdot y^2+b_5\cdot x\cdot y+b_6\cdot x^2\cdot y+b_7\cdot x\cdot y^2+b_8\cdot x^2\cdot y^2 \quad (3.2)$$

$$z_1 = c_0+c_1\cdot x+c_2\cdot y+c_3\cdot x^2+c_4\cdot y^2+c_5\cdot x\cdot y+c_6\cdot x^2\cdot y+c_7\cdot x\cdot y^2+c_8\cdot x^2\cdot y^2 \quad (3.3)$$

The coefficients a_n, b_n, c_n are determined by solving the system of linear equations expressing the conditions that the initial control points should map exactly on the final ones. For example, assuming that the first initial control point is (1, 2, 0) and the final one is (4, 6, 7) the corresponding set of equations becomes as in equations 3.4, 3.5 and 3.6, respectively.

$$4 = a_0 + a_1 \cdot 1 + a_2 \cdot 2 + a_3 \cdot 1^2 + \cdots + a_8 \cdot 1^2 \cdot 2^2 \quad (3.4)$$

$$6 = b_0 + b_1 \cdot 1 + b_2 \cdot 2 + b_3 \cdot 1^2 + \cdots + b_8 \cdot 1^2 \cdot 2^2 \quad (3.5)$$

$$7 = c_0 + c_1 \cdot 1 + c_2 \cdot 2 + c_3 \cdot 1^2 + \cdots + c_8 \cdot 1^2 \cdot 2^2 \quad (3.6)$$

By enforcing the conditions for interpolation for each of the control points, the coefficients can be determined and the above equations with the known coefficients are used to compute the new position of each node in the patch. Note that the quadratic edges of the final mesh would introduce a discontinuity in the tangent where the border nodes connect two consecutive patches. This problem can be tackled by using an isoparametric transformation with cubic edges (quad 16 transformation) or, as we did, by increasing the density of the patches until this effect becomes negligible.

As outcome of the isoparametric transformation, the patch is moved from the initial CPs to the final ones by following the defined transformation. In our application the strategy is to place the final CPs on the LV endocardium for every segmented surface of the 4D dataset and to apply the isoparametric transformation sequentially until the surface is completely covered by the defined patch (Figure 3.4 e).

In this way the initial patch is deformed accordingly to the shape of the geometry that the user wants to reproduce. The effects of this method can be qualitatively evaluated by comparing Figures 3.4 c and 3.4 e, where the former figure represents the initial segmented geometry and the latter the high-quality mesh of the reproduced object. In the case that the user wants to include finer details of the initial geometry, more CPs have to be used. There is not any restraint on which geometry of the 4D dataset to start with.

The accuracy of this method is proportional to the number of CPs used, because the new mesh is anchored to the old one by means of the CPs, which are exactly coincident with the surface, while the intermediate nodes are not necessarily exactly on the surface.

Dedicated algorithms have been developed to semiautomatically project the final CPs onto all the configurations of the 4D dataset in order to avoid a tedious and a time-consuming manual positioning of the final CPs in each of the LV target configurations that form the 4D datasets.

Please note that a simple radial projection of the CPs from a scaled down model on the whole geometry would have resulted in an inaccurate reproduction in particular around the Y-junction area (where the LV is connected to the LA and aorta). For this reason, the mesh of the LV is built as sum of three different parts (the LV sac, the Y-junction, and the connection between these two parts) and disclosed separately in the following sections 3.2.3.1, 3.2.3.2, and 3.2.3.3.

The low spatial resolution of the 4D MRI and 4D US (if compared to the 4D CT) could result in high uncertainty in correspondence of the Y-junction, where finer details would be needed. Consequently, only the LV sac is built for the 4D MRI and 4D US datasets, while the complete reconstruction is performed for the 4D CT dataset.

3.2.3.1 Application of the Morphing Tool on the LV sac

In this section, the strategy used to project the final CPs of the isoparametric transformation on the LV sac configurations of the 4D dataset is reported. The structured mesh of the LV sac is built up to a predefined percentage of the total vertical length of the LV, from the apex to the mitral valve orifice centroid. The application of the morphing tool in the LV sac can be summarized as follows:

1. Build a simplified generic shape (Figure 3.5 (1)) (whether half cylinder or truncated pyramid) to which the manual morphing tool is applied with the desired number of patches and CPs. In Figure 3.5 (1), the simplified generic shapes used with 9, 36, 144, and 420 patches (from left to right) are reported;
2. Scale up and down the mapped simplified generic shape in order to fit outside and inside the LV (Figure 3.5 (2));
3. The CPs of the two scaled models define the projection trajectories of the CPs onto the target surface. (3) The CPs are projected onto the target surface by following the defined projection trajectories (Figure 3.5 (3));
4. The LV sac is mapped with the same patches of the simplified generic shape. The user has a direct control on the number of nodes by changing the number of subdivisions inside each patch (Figure 3.5 (4)).

The morphing tool application in the LV sac is performed sequentially to all the configurations of the 4D dataset by using a loop-structure. The scale factors of step (2) are chosen such that the two scaled models fit completely inside and outside all the LV configurations throughout the cardiac cycle. Therefore, the scale down and scale up factors are tuned manually at this stage with respect to the end-systolic (such that one scaled model fits inside) and end-diastolic configurations (the second scaled model should encompass this configuration).

Once built and mapped, one simplified generic shape can be used to map an infinite number of datasets. Therefore, step (1) has to be repeated only if the user wants to change the number of CPs.

3.2.3.2 Application of the Morphing Tool to the Y-junction (Aorta and Left Atrium)

As already mentioned this step was accomplished only for the 4D CT dataset. Anatomically the left atrium and the aorta root are very closely located resulting in the empty space between the two parts to be very narrow. For this reason, the previous approach of deforming the initial mapped shape (truncated pyramid) into the 4D segmented shapes was feasible only for the LV sac reconstruction of the different 4D imaging datasets. However, the same approach was found impracticable for the upper part of the left heart (denoted as Y-junction), because in this region the nodes of the LA and of the aorta are separated by a really thin empty space which would get intersected after the deformation to the new temporal configuration. Therefore, this anatomical part is treated as a vessel bifurcation and mapped by means of the following steps:

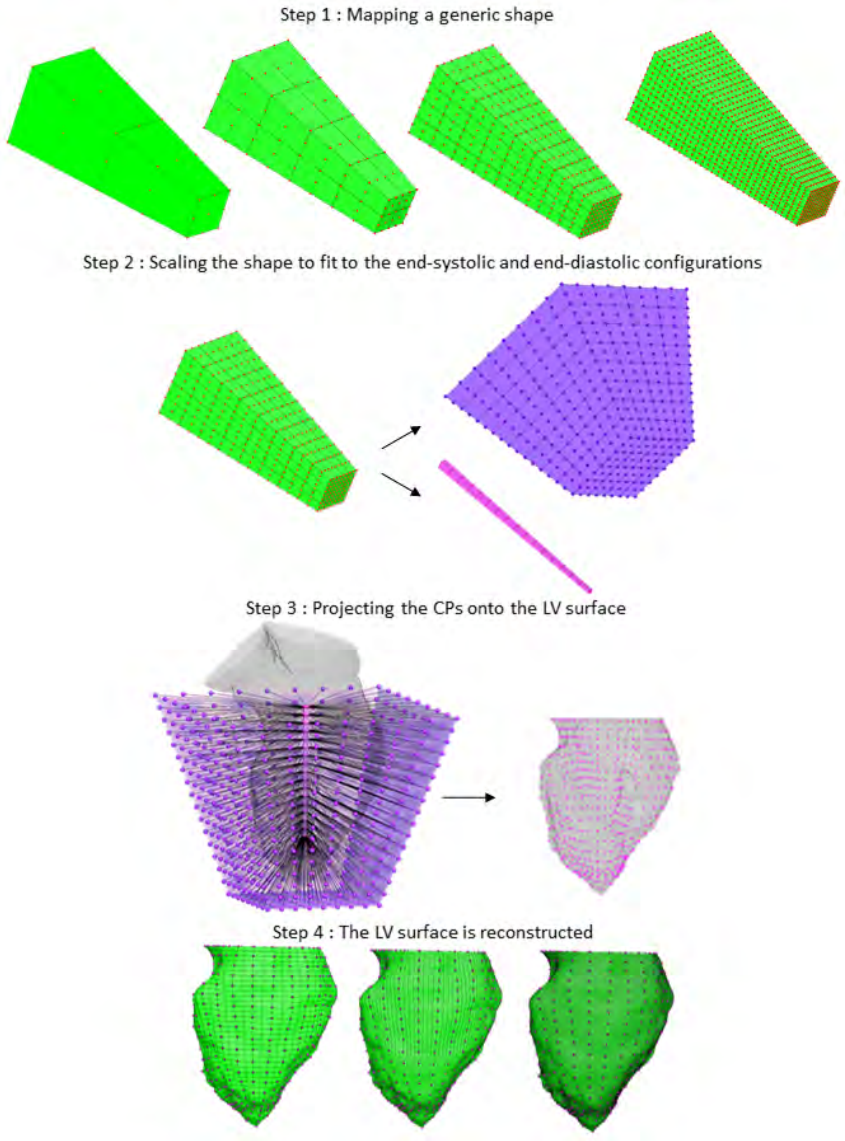

Figure 3.5: Strategy used to build a high-quality mesh of the LV chamber: (1) a truncated pyramid is mapped with the desired mesh topology (resp., 9, 36, 144, and 420 patches from left to right); (2) the mapped truncated pyramid is scaled up and down to fit completely inside and outside the LV; the CPs of the two scaled truncated pyramids define the projection trajectories to be followed to locate the CPs onto the target LV; (3) the CPs are projected onto the LV surface; (4) the LV surface is reconstructed by using the projected CPs and the connectivity of the truncated pyramid. The user can directly choose the number of nodes by varying the number of subdivisions of the patches.

1. Two biplanar meshes are located in the bifurcation center (Figure 3.6(1e)) by following this procedure:
    a) Two points are manually picked in the part of the surface that separates the conduits (Figure 3.6(1a)).
    b) A Polyline is delineated as a result of the intersection on the surface between the Polyline passing through the two points and a copy of it translated in the vertical direction (Figure 3.6(1b)).
    c) The resulting Polyline is translated towards the two directions of the valve centroids (Figure 3.6(1c)).
    d) The two translated Polylines are rotated to obtain a double upside-down Y-mesh in correspondence to the bifurcation center (Figure 3.6(1d)).
    e) The nodes of the horizontal semicircle are radially projected onto the target surface (Figure 3.6(1e)).
2. An infinitesimally small circular shape mesh-line, that shares the same topology of the biplanar mesh, is located in the centroid of the two valvular planes (Figure 3.6 (2)).
3. The circular meshes are translated up to the desired vertical length; N small intermediate Polylines are created as a result of linear interpolation between a concentric scaled down biplanar mesh and the circular shape mesh-line (Figure 3.6(3)).
4. *N* large intermediate Polylines are created by scaling up concentrically the *N* small intermediate Polylines (Figure 3.6 (4)).
5. Polylines of the conduits are created as a result of the linear intersection between the intermediate small and big Polylines on the target surface (Figure 3.6(5)).
6. The coordinates of the Polylines are used as target CPs of the isoparametric transformations (Figure 3.6(6)).

As before, the morphing tool is applied sequentially to all the configurations of the 4D dataset by using a loop-structure. Only Step (1a) requires manual interaction of the user in order to pick the two points in the first configuration of the datasets. The remaining steps are performed automatically by the algorithm. In the current state, the main limitation of the Y-junction reconstruction is that the LA appendage cannot be reproduced accurately and for this reason it was not included during the segmentation process.

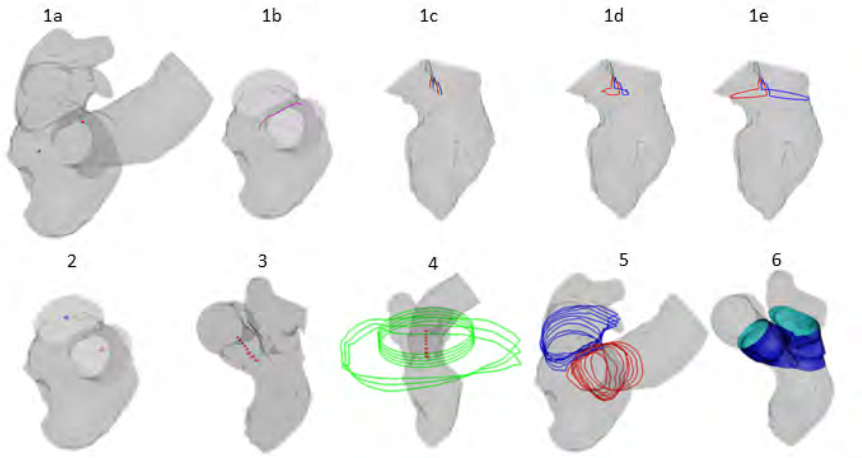

Figure 3.6: Strategy followed to create high-quality mesh of the Y-junction: (1) generation of two semi-circular biplanar meshes; (2) generation of two circular meshes infinitesimally small located in the centroid of the valvular planes; (3) translation of the circular mesh up to the desired position; generation of intermediate Polylines infinitesimally small (in red) as linear interpolation between a concentric scaled down biplanar meshes and the translated circular meshes; (4) the intermediate small Polylines are concentrically scaled up (in green); (5) the Polylines of the bifurcation are created as linear intersection between the small and big versions of the Polylines which lie on the target surface; (6) the coordinates of the Polylines are used as final CPs for the isoparametric transformations.

3.2.3.3 Connection of the LV sac and the Y-junction

The upper LV sac border and the lower border of the Y-junction of each mesh are built such that they share the same number of nodes but not the same numbered order. The final step is then to connect the two parts following this strategy:

1. Reordering the nodes of the two borders (ventricle side and bifurcation-side) (Figure 3.7 (1)). This intermediate step is needed because the generated lower border of the bifurcation and the upper border of the LV sac do not share the same numbering of nodes.

2. Generation of an intermediate Polyline that lies on the target surface (Figure 3.7 (2)).

3. The coordinates of the two borders and the intermediate Polyline are used as final CPs for the isoparametric transformations (Figure 3.7 (3)).

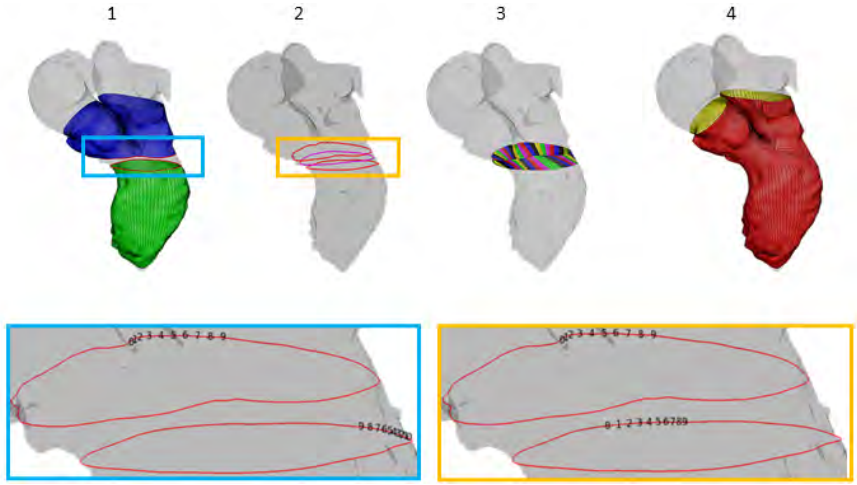

Figure 3.7: Generation of the connection between LV sac and the Y-junction: (1) renumbering of the border nodes; (2) generation of an intermediate Polyline; the nodes of the three Polylines will be the final CPs of the isoparametric transformations; (3) application of the isoparametric transformation; (4) final reconstruction of the total LV.

The morphing tool application in the LV sac, Y-junction, and the connection between these two parts is performed sequentially for every LV configuration of the 4D dataset by means of a loop-structure.

3.2.4 Temporal interpolation

The temporal interpolation of the newly created 4D structured meshes is needed in order to match the temporal resolution requirements of a CFD simulation (Figure 3.8). In this way, the set-up of the CFD model with moving boundaries is independent of the time instants available in the 4D imaging dataset. The related code (developed as well in PyFormex) takes the 4D newly created meshes as input and interpolates the position of each node of the mesh with a cubic spline (Bezier or natural) that can be chosen by the user. By knowing the cardiac cycle duration and the time step size required in the CFD simulation, the user can choose the number of the intermediate configurations to be created.

3.2.5 Quality and accuracy assessment of generated meshes

In order to validate the described method both the quality of the meshes and the accuracy of the meshed geometry reconstructions, compared to the starting dataset, are investigated. As quality criterion, the equiangle skewness (Q_{eas}) is chosen. This parameter, often used as quality index for CFD meshes, represents a normalized measure of skewness, ranging from 0 (the optimal

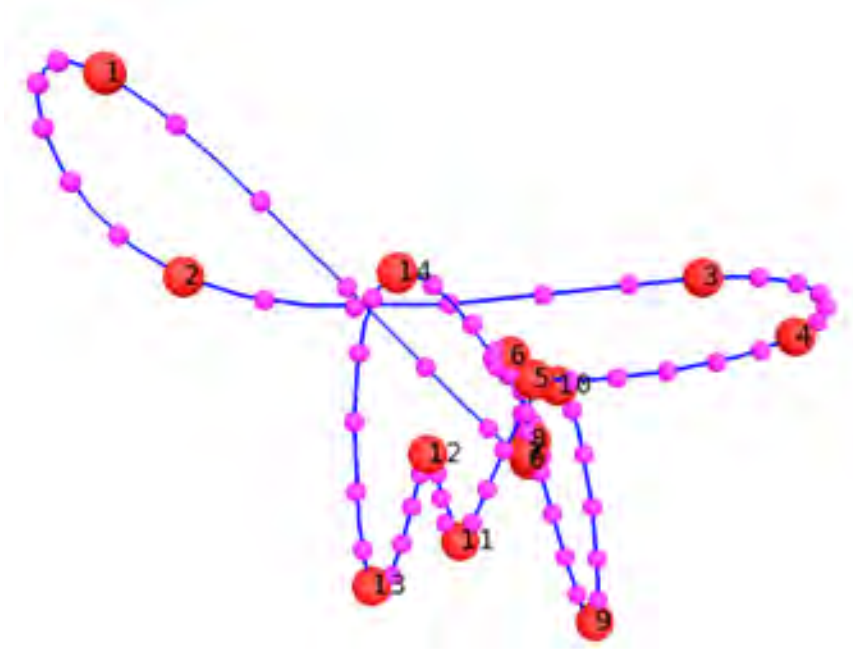

Figure 3.8: Temporal interpolation for the first node of the 4D reconstructed meshes during a cardiac cycle, represented as trajectory (in blue) between the positions derived from the 4D CT reconstruction with 336 CPs (in red, numbered from 0 to 14). The resulting intermediate positions of each node (in magenta, for the first node) are connected using the initial mesh connectivity to get the intermediate meshes.

equilateral cell) to 1 (for a completely degenerated cell). The Q_{eas} depends on the angle formed between adjacent edges of each cell in the mesh, as reported in equation 3.7, where θ_{max} and θ_{min} are the largest and smallest angles in the cell and θ_e is the angle of the equiangular cell, which is 90° for the quadrilateral faces. As usually done in the CFD meshing community, the maximum and average threshold values for the equiangle skewness (from now on referred to simply as *skewness*) are set, respectively, to 0.9 and 0.25 [111]–[113].

$$Q_{eas} = max\left(\frac{\theta_{max} - \theta_e}{180 - \theta_e}, \frac{\theta_e - \theta_{min}}{\theta_e}\right) \tag{3.7}$$

Regarding the accuracy, the distances of the points in the mapped mesh from the segmented surface are reported for all the 4D reconstructed datasets. The distance for each node of the mapped mesh from the segmented surface has been classified into 6 fixed different intervals from 1/1000 of a mm up to

the maximum computed value. We also calculated the volume percentage difference with respect to the initial segmented geometries. This was done only for the 4D CT dataset because only in this case the LV was completely reconstructed.

3.2.6 Algorithm speed assessment

The analysis was performed on a PC with a processor $IntelCore^{TM}$ I7-4810MQ @2.80GHz with 16.0 GB RAM. The total time of the algorithm is directly reported by PyFormex while the time related to reading operations has been evaluated using the timeit function available in the timeit python library.

3.3 Results

For the 4D CT dataset 336, 968, and 2165 CPs were chosen to reconstruct the complete LV,while for the 4D US and 4D MRI datasets the LV sac reconstructions were performed with 41, 153, and 593 CPs. This different choice is due to the fact that for the 4D CT dataset we reproduced the whole LV geometry and (at least partially) finer details of the endocardial surface such as the trabeculae. For clarity the analysis of the parameters is conducted on averaged values over a dataset (all time steps), except when reporting the maximum and minimum values of a parameter. Unless explicitly stated, conclusions drawn are applicable to each mesh of the 4D dataset. The skewness distribution is reported for the reconstructed LV mesh of the 4D data that has the maximum skewness value.

3.3.1 CT Dataset

For the 4D CT dataset the LV sac was reconstructed with 153, 593, and 1705 CPs. In the first case the reconstruction resulted in smooth LV endocardial surfaces, while in the other cases the finer control given by the increased number of CPs was allowed to catch, at least partially, the trabeculae and the papillary muscle. The Y-junction was reconstructed, respectively, with 183, 375, and 460 CPs. Therefore 3 different reconstructions of the total geometry (which includes the LV, the left atrium, aorta, and the valvular planes) were performed with 336, 968, and 2165 CPs (Figure 3.9). In addition to the accuracy and quality evaluations (for the 4D CT dataset) an estimation of some useful physiological quantities are disclosed, such as the LV volume and the distance between the apex and the bifurcation center.

3.3.1.1 Accuracy

For the reconstructions with 336, 968, and 2165 CPs, respectively, 67.6%, 74.5%, and 83% of the nodes have a distance error inferior to the pixel size,

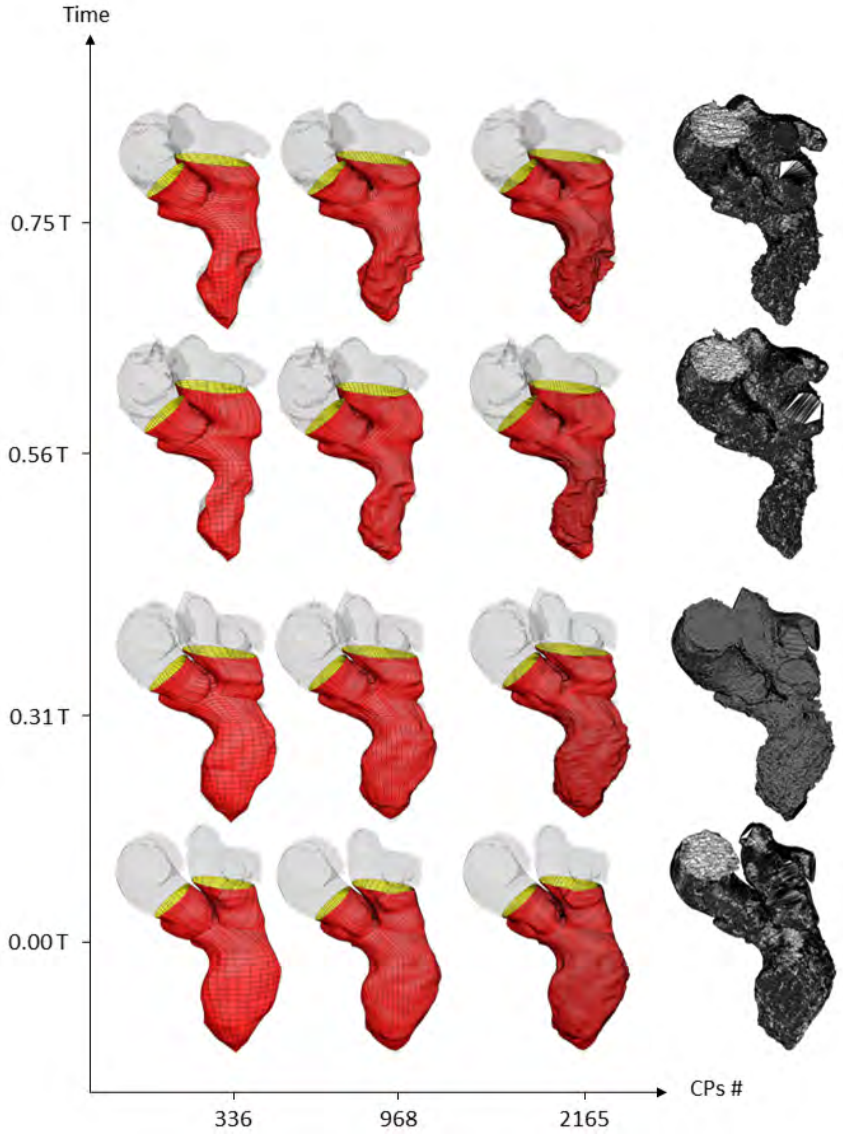

Figure 3.9: LV sac reconstructions for the 4D CT dataset with 336 (left), 968 (middle), and 2165 (right) at the end-diastolic configuration (1st row down), end-systolic configuration (3^{rd} row down) CPs, and two intermediate configurations (2^{nd} and 4^{th} rows). On the right side of the graph are the corresponding segmented meshes. T represents the adimensional period of the cardiac cycle, where $T = 0$ indicates the time corresponding to the end-diastolic configuration.

while 7.6%, 4.0%, and 2.4% of the nodes have a distance error larger than 1mm (Figure 3.10(b)). Conversely, the percentage of the nodes with distance error inferior to 1/1000 mm decreases by increasing the number of CPs. This trend is due to the fact that the reconstructions with 968 and 2165 CPs could better catch the trabeculae of the LV surface resulting in a more irregular surface. Therefore, some smoothing operations were performed in these cases to preserve the mesh quality. The differences induced by the smoothing operations in the LV sac are visible also in the colormaps (Figure 3.10(a)). By looking at them from left to right it is also noticeable how increasing the number of CPs enlarges/reduces the areas associated with a lower/higher distance error (yellow, green, cyan spots/red, and magenta spots).

As for the volume difference percentage (Figure 3.10(c)), the average value is 2.9%, 1.1%, and 0.9%, for the LV reconstructions with 336, 968, and 2165 CPs, respectively. This again indicates that the two latter cases provide more accurate reconstructions of the original surfaces.

3.3.1.2 Quality

In the reconstructions with 968 and 2165 CPs some configurations (resp., 3 and 6) throughout the cardiac cycle had a few elements with a skewness higher than the threshold value of 0.9. For this reason, some manual corrections were performed with a dedicated algorithm to modify critical mesh elements in the Y-junction (which took less than 10 minutes). Regarding the skewness distribution (Figure 3.10(d)), 65%, 72.7%, and 77.9% of the elements are below the threshold of 0.3 for the reconstructions with 336 CPs, 968 CPs, and 2165 CPs, respectively.

3.3.1.3 Physiological Quantities

We also derived relevant physiological quantities from the 4D CT dataset: the LV volume (Figure 10(f)), the distance between the apex and the bifurcation center (Figure 3.10(g)), and the ejection fraction (EF). The volume and the EF are reported both for the segmented geometries and the reconstructed datasets. The distance between the apex and the bifurcation center was calculated only for the reconstructed datasets. EF was 0.56, 0.58, 0.55, and 0.56, respectively, for the segmented geometry and the reconstructions with 336, 968, and 2165 CPs underlying once more the accuracy and the reliability of the method. The distance between the apex and the bifurcation center (Figure 3.10(g)) follows the same trend in the three different reconstructions, with an increase in the initial configurations (the 1st configuration of the dataset corresponds to the end diastolic LV configuration) followed by a decrease until the last configuration. This is in agreement with the evolution of LV volume until the 10^{th} configuration, while the opposite trend after this configuration suggests that the increase in volume is not followed by a vertical elongation.

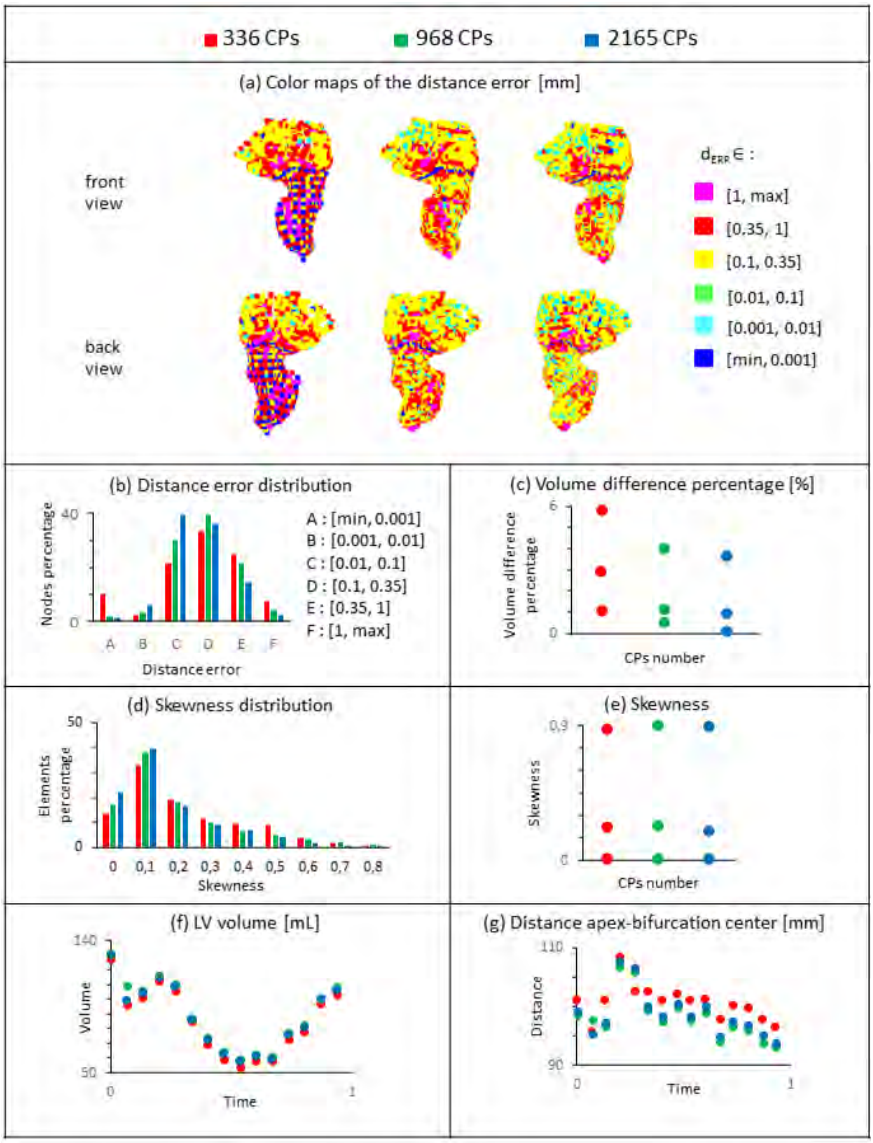

Figure 3.10: (a), (b), (c) Accuracy of the generated 4D CT meshes from the original 4D dataset with (c) that reports the minimum, average, and maximum value of the volume difference percentage between the reconstructed meshes and the segmented geometries in the 4D CT dataset; (d), (e) quality of the newly created 4D meshes with the latter reporting the minimum, average, and maximum skewness for the 4D meshes of the CT dataset; (f), (g) estimation of physiological parameters. In (a) the color maps of the distance error (front and bottom views) are reported for the reconstructions, respectively, with 336, 968, and 2165 CPs from left to right. In the horizontal axis of Figures 3.9(f) and 3.9(g), time represents the adimensional period of the cardiac cycle, where $T = 0$ indicates the time corresponding to the end-diastolic configuration.

3.3.2 US and MRI datasets

In the US (Figure 3.11) and MRI cases (Figure 3.12), the LV endocardial surfaces have been reconstructed up to 50% and 55% of the distance between the apex and the mitral valve centroid, respectively.

3.3.2.1 Accuracy

As expected, increasing the number of CPs from 41 to 593 resulted in a better accuracy. This leads to the following (Figures 3.13(a) and 3.13(d)):

1. An increasing number of elements in the classes associated with a lower error, thus closer to the surface to be reproduced.
2. For about 90% of the configurations, the maximum value of the distance error decreased.

Increasing the number of CPs, the percentage of the nodes with distance error inferior to 1 mm is 61%, 89.8%, and 99.3% and 76.4%, 94%, and 98.5%, respectively, for the US and MRI. The maximum value of the distance error decreased for almost 90% of the cases for both MRI and US.

3.3.2.2 Quality

The skewness conditions were satisfied in every case (Figures 3.13(b) and 3.13(e)), but increasing the number of CPs did not result in an improvement of the mesh quality. Both for the US and MRI datasets the histograms of the skewness distribution (Figures 3.13(c) and 3.13(f)) highlight that around 90% of the elements had a skewness between 0.0 and 0.3.

3.3.3 Algorithm speed

The total running time of the algorithm is reported in (Figure 3.14). For the CT case the performance data refers to the reconstruction with 336 CPs, in order to have a number of CPs closer to the US and MRI case. At first glance, the total time was very different in the three cases, but this is due to the different reading time that is proportional to the dimension of the starting geometry file (resp., 0.1, 2, and 20 MB). In the CT case, 1.97 s are required to reconstruct one LV sac, while the total reconstruction time for one complete LV geometry becomes 22.37 s. Note that 9.99 s out of these 22.37 s are related to reading the data. Most of the processing time is spent on the script that creates the high-quality structured mesh for the LV Y-junction; therefore future optimization of the algorithm should aim for this part.

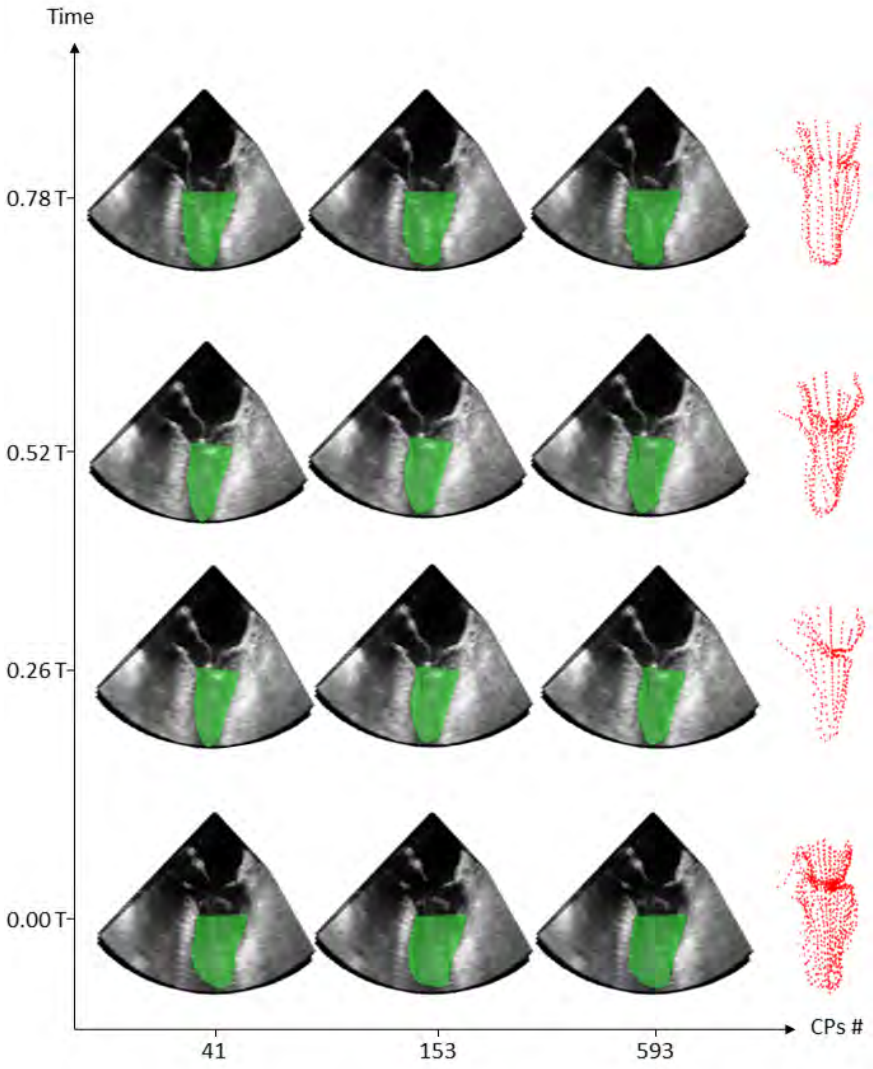

Figure 3.11: LV sac reconstructions for the 4D US dataset with 41 (left), 153 (middle), and 593 (right) at the end-diastolic configuration (1st row down), end-systolic configuration (2^{nd} row down) CPs, and two intermediate configurations (upper rows). On the right side of the graph are the corresponding segmented point-clouds. T represents the adimensional period of the cardiac cycle, where $T = 0$ indicates the time corresponding to the end-diastolic configuration.

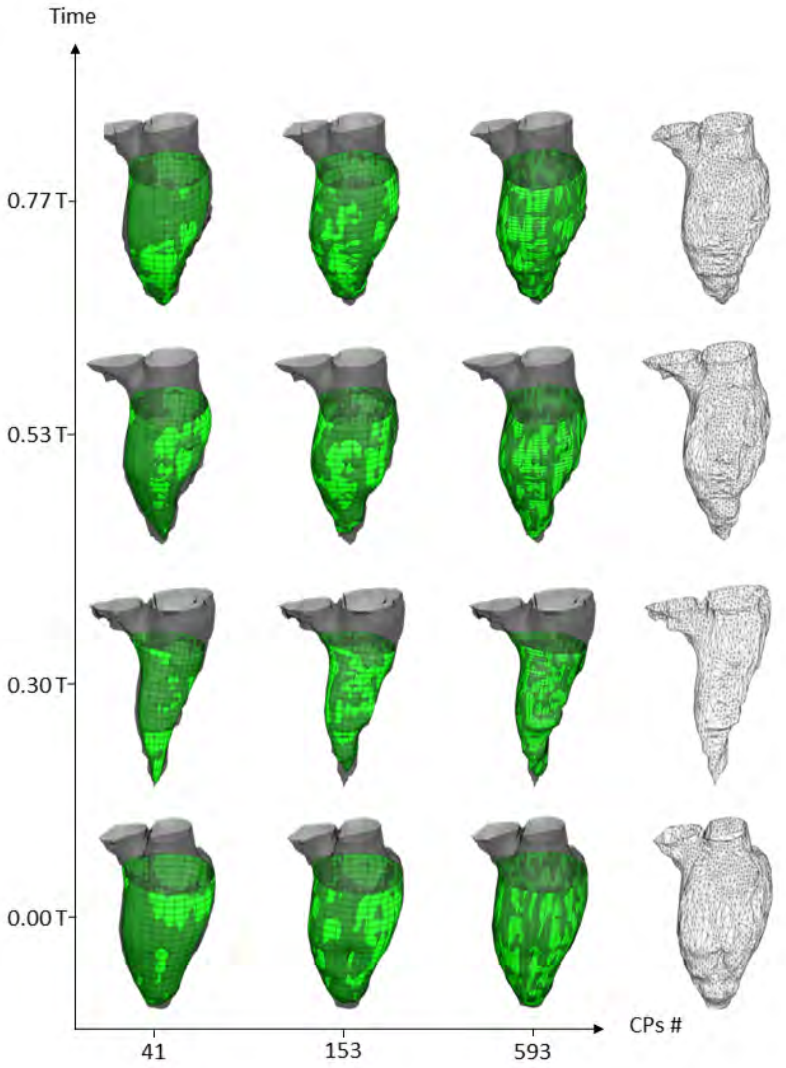

Figure 3.12: LV sac reconstructions for the 4D MRI dataset with 41 (left), 153 (middle), and 593 (right) CPs at the end-diastolic configuration (1^{st} row down), end-systolic configuration (2^{nd} row down), and two intermediate configurations (upper rows). On the right side of the graph there are the corresponding segmented meshes. T represents the adimensional period of the cardiac cycle, where $T = 0$ indicates the time corresponding to the end-diastolic configuration.

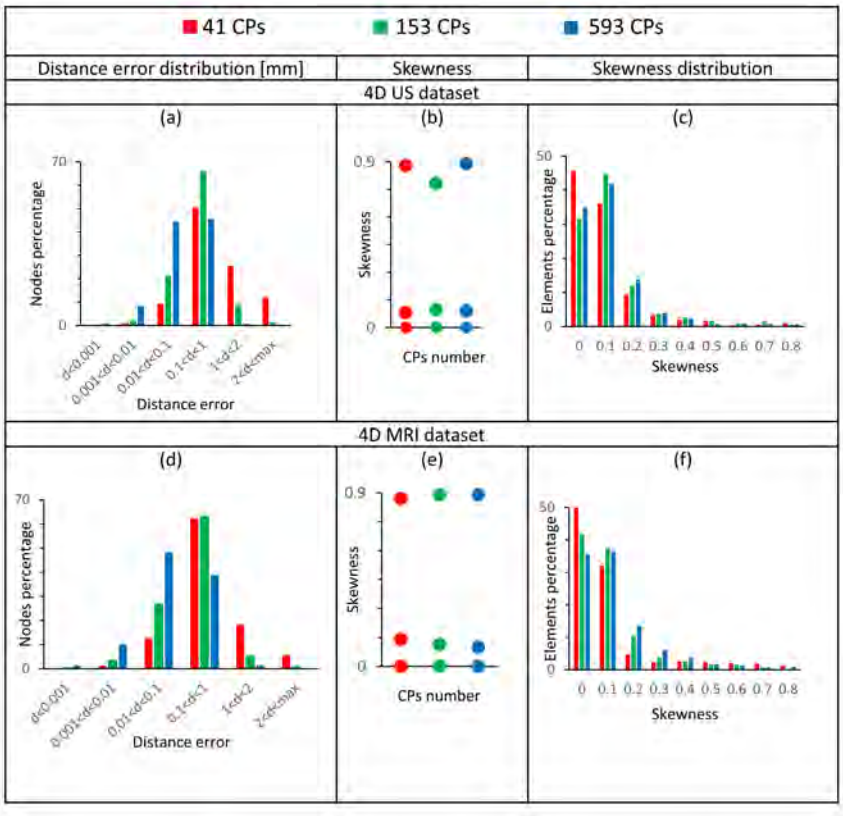

Figure 3.13: Quantities reported to evaluate the accuracy from the original 4D dataset and the quality of the newly created 4D meshes for the 4D US (a, b, c) and 4D MRI datasets (d, e, f), respectively, with 41, 153, and 593 CPs in red, green, and blue. (b) and (e) report the minimum, average, and maximum skewness for the 4D meshes of the US and MRI datasets, respectively.

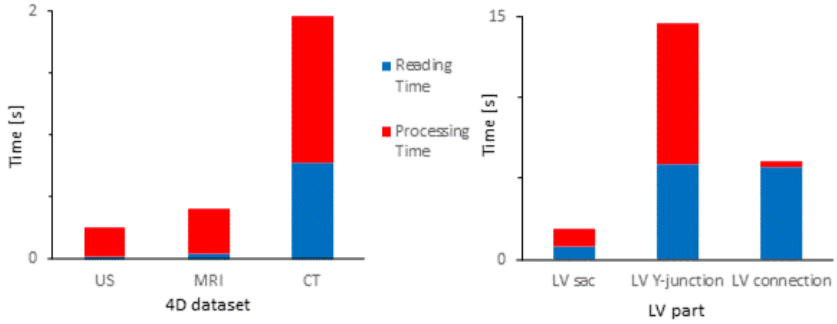

Figure 3.14: Total running time (divided into reading and processing time) is reported for the three 4D datasets (a) and for each part that form the total model in the 4D CT case (b) as index to evaluate the performance of the algorithm. The meshing involves the configuration at one instance in time.

3.4 Discussion

This paper presents a novel semiautomatic methodology to create 4D high-quality structured meshes with 1-to-1 vertex correspondence starting from 4D imaging acquisitions of the left ventricle. It has been applied to three different 4D imaging datasets (US, MRI, and CT) and all the generated 4D meshes have been reported as video file in the Supplementary Materials included with the referred paper (see section 3.8). To the best of our knowledge, the current state of the art in 4D patient-specific cardiac geometries is mainly based on deformable models, with an extended part of the research being focused on improving the quality of the clinical images, the temporal resolution of the acquisition techniques, and the automation of the cited models.

Among the works on deformable models, among others, Lim et al. [94] reconstructed 4D patient-specific meshes of the heart with 1-to-1 vertex correspondence. In the referred case the heart was automatically meshed with triangular elements only and it took about 30 minutes to create a 4D mesh dataset of 20 frames with 20,000 nodes on their computer infrastructure. The main limitations of deformable model techniques are that they exhibit poor convergence for noisy images, large errors associated with large deformations between the neighboring frames, and the need of user interaction to manually segment the first configuration and delineating the contours along all the configurations of the 4D dataset, which is a very laborious task also for skilled practitioners [94], [114]. The added value of our method is that it is independent of the clinical images quality, the accuracy is tunable by varying the number of control points, it is versatile both in terms of the pathophysiological state of the heart (working equally with healthy and pathological hearts)

and in terms of imaging clinical modalities (CT, MRI, and US). Together with our developed code which performs a temporal interpolation of the 4D high-quality meshes, we can easily meet the temporal resolution requirements of a CFD simulation (by creating as many intermediate high-quality meshes as needed) even when starting from a 4D dataset which contains at most 30 configurations along the cardiac cycle. Furthermore, referring to the manual version of our tool (which requires the manual placement of the final CPs), it can be used in general for all the high-quality meshing problems and, in combination with tracking methods and landmarks, it could be used to include the torsion and stretching of the LV endocardium.

From a more practical point of view, the advantages related to the use of our semiautomatic morphing tool are that the operator can choose both the number of nodes (by changing the number of subdivisions of the isoparametric transformations) and the mesh element type (by defining the patch delimited by the initial CPs); moreover, the subdivision of the LV in three different parts is useful in case that the user wants to increase the mesh density in a specific location (around the apex or the Y-junction bifurcation or in the middle band).

As quality requirements, we choose mean and maximum skewness threshold values of 0.25 and 0.9. In the cases corresponding to the 4D US, 4D MRI, and CT with 336 CPs the criteria were successfully fulfilled. For the CT data, in the Y-junction reconstructions with 968 CPs and 2165 CPs the few elements that did not meet these criteria were fixed with an additional code, which let the user manually move the CPs or the nodes in the critical spots of the mesh. For the studied case, this involved no more than 10 minutes for the corrections.

Regarding the accuracy, in the 4D CT case the percentage of nodes that has a distance error inferior to the pixel size (0.35 mm) is 67.6%, 74.5%, and 83.0%, respectively, for the 336, 968, and 2165 CPs reconstructions. These values become 92.4%, 96%, and 97.6% if we use a threshold value of 1 mm, such as what is done for the US and MRI case. In the case with 593 CPs both the 4D US and MRI high-quality meshes have a distance error inferior to 1 mm for, respectively, 99.3% and 98.5% of the nodes. Considering that the pixel size is 0.60 and 1.64 mm, using the threshold of 1 mm can be regarded as effective. Therefore, we conclude that both the quality and the accuracy of the morphing tool have been successfully tested for each of the three 4D datasets.

For the 4D CT dataset (which reconstructs the total LV geometry), we also estimated some relevant physiological parameters, quantifying cardiac deformation and function (distance between the apex and the bifurcation

center, the volume and the ejection fraction). Due to the fact that the meshes share the same connectivity, an evaluation of a distance during the cardiac cycle becomes immediately feasible with few lines of code. The algorithm developed can build a complete high quality LV mesh in approximately 22 s; thus a 4D dataset of 15 configurations is reconstructed in 5 minutes and 30 seconds. In our case the computational time is affected by the number of CPs projected onto the surface but does not depend on the number of nodes of the mesh (determined by the subdivision used in each patch); therefore the subdivision of each patch is almost of free-cost resulting in a substantial saving of computational time if the user wants to change the mesh density ex post. The code was entirely implemented in PyFormex, an open-source python-based software.

The main limitation of the morphing tool (in the semiautomatic implementation) is that the nodes of the reconstructed 4D meshes do not follow the material anatomical points of the LV. Therefore, the resulting 4D meshes do not take into account the torsional motion of the LV, which may have an impact on the development of the intraventricular flow and may be a parameter of physiological relevance. In the cases presented, the available 4D medical image modalities (4D US, MRI, and CT) could not track the motion of the material points of the LV endocardium. However, when one can start from images with tracking and landmarks positioning (such as CMR Tissue tagging, MRI Phase contrast imaging, or Speckle-Tracking Echo), one can track the material points by means of the general technique which relies on the manual positioning of the final CPs, without using the semiautomatic algorithms for the LV sac, the atrium and the aorta, and the zone connecting both. As such, one could incorporate torsion in the meshed datasets. Also, the mapping algorithms are not fully automatic, requiring the interaction of the user, even if minimal, in the choice of (i) the two scaling factors in the LV sac application, (ii) the two picked points in the Y-junction application, and (iii) the starting border nodes for the renumbering (step (1) of the connection between LV sac and Y-junction). A strategy similar to the one used by Lim et al. [93] (based on greedy algorithm) could be used to automatically select the two points in the Y-junction. As future development, these steps could be fully automated.

For the CT dataset, we included the LA and aorta up to a certain length, which can be increased straightforwardly until running into principal bifurcations. On the contrary, the presence of the appendage was neglected at this stage. Future actions must be performed to accurately include the appendage and the principal bifurcations of the LA in order to segment and mesh a complete left heart model.

At this stage the morphing tool requires a 4D segmented dataset or a 4D cloud points as input to build the 4D quality meshes. Even if more and more

segmentation software is going into the direction of automatic procedures, the morphing tool could be upgraded in order to be applied directly to the 4D imaging dataset. In this case the placement or projection of the CPs would be based on the grey-scale levels of the image. Also, by starting from the generated structured surface meshes the automatic development of high-quality hexahedral volume meshes will be addressed.

3.5 Conclusions

We developed a novel method capable of creating 4D high quality meshes of the LV with 1-to-1 vertex correspondence starting from a generic 4D clinical imaging dataset. The generated 4D high-quality meshes can be used as reference to impose the LV endocardial motion in a patient-specific CFD or FSI simulation with moving boundaries and avoid convergence errors due to low quality meshes. The sensitivity of the CFD and FSI-results to choices made in morphing and meshing will be the subject of a follow-up study. The method focuses on the LV geometry but is easily adaptable to other anatomical sac or tube-like structures.

3.6 Conflicts of interest

The authors declare that they have no conflicts of interest.

3.7 Acknowledgments

This work was supported by the European Commission within the Horizon 2020 Framework through the MSCAITN-ETN European TrainingNetworks (Project no. 642458).

3.8 Supplementary Materials

4D patient-specific structured meshes of the LV endocardium from 4D clinical images are available at the following link: Supplementary Materials.

Chapter 4

Influence of torsion on a patient-specific CFD model of the LV based on the Chimera technique

This chapter introduces the methodology to develop patient-specific Computational Fluid Dynamics models based on the Chimera technique, to overcome the excessive mesh distortion previously encountered by means of the Arbitrarian Lagrangian Eulerian approach. The workflow is showcased assessing the impact of torsion on the Left Ventricle (LV) hemodynamics. This chapter is based on the paper Mixed impact of torsion on LV hemodynamics: A CFD study based on the Chimera technique, *Computers in Biology and Medicine*, vol. 112 (2019), Article ID 103363.

4.1 Introduction

With Cardiovascular Disease being the leading cause of death worldwide with global mortality of 31% [115], the progressive ageing of the population challenges the clinical routine, creating needs for new tools to assist the clinicians. In this regard, Computational Fluid Dynamics (CFD) modeling can provide relevant variables, such as local pressures gradients, velocities, energy indexes, residence time and shear stress, which would otherwise require invasive procedures such as catheterization [115], [116]. Furthermore,

the continuous progress of computational performance (as indicated by Moore's law [67]) and medical imaging modalities opens perspectives for new concepts of diagnostics, therapy and surgical planning based on patient-specific CFD models. In comparison with cardiac in vivo imaging modalities, such as 3D ultrasound, cine-MRI and 4D flow MRI, patient-specific CFD cardiac simulations allow for a finer spatial and temporal resolution which is necessary to fully comprehend LV fluid dynamics and explore how imaging data can be converted into quantitative metrics, useful for the clinic, and with a clear mechanistic interpretation. Furthermore, such simulations also allow us to assess the impact that medical imaging protocols and subsequent image and signal processing may have on the interpretation of the measured flow field and appreciate the impact of limited resolution, averaging and filtering on the visualized flow metrics. An example is the work of Chnafa et al. [117], who demonstrated the existence of turbulence in the left ventricle using computational models, which is impossible to visualize in vivo due to the temporal and spatial limitations of all existing imaging modalities, or the work of Van Cauwenberge et al. [118], where CFD simulations were used as the basis and ground truth of virtual ultrasound sequences of the (idealized) ventricle.

Despite the clinical application of CFD modeling in cardiology applications is still very limited, the FDA approval in 2016 of HeartFlow [6] (which diagnoses the Fractional Flow Reserve in the individual patient by means of CT images of the coronary vasculature) together with the CE mark of TAV-Iguide [7] (which predicts a.o. the paravalvular leakage in endovascular aortic valve treatment) demonstrate the recent breakthrough of patient-specific CFD techniques. Such level of clinical application readiness is not within immediate reach for simulations involving blood flow inside cardiac chambers. When focusing on the Left Ventricle (LV), several factors arise the complexity of the CFD problem, among which the irregularities on the endocardial surface determined by the trabeculae carneae and the papillary muscles [74]–[76], [119], the large deformation of the LV endocardium, the impulsive kinetics of the Mitral Valve (MV) leaflets, and the transitional-to-turbulent flow in the LV sac [117]. The combination of all these factors implies that flow should be solved as part of a CFD or a fluid-structure interaction problem where the motion and deformation of the wall and leaflets may or may not be prescribed. Even though, to the best of our knowledge, they have never been combined all together, patient-specific CFD simulations of the LV have already been used to compare the surgical options to treat patients with ventricle malformation [79], [120] and to improve our understanding of the impact of cardiac pathologies, such as dilated [121], [122] and hypertrophic [123] cardiomyopathy, and myocardial infarction [123] on intraventricular

flow dynamics. As confirmed by these studies, patient-specific CFD simulations can have an important impact in several clinical applications and, in this regard, we want to improve our current level of the technology that would allow for more robust patient-specific CFD simulations of cardiac hemodynamics.

Patient-specific CFD models of the LV are typically performed by means of the Arbitrary Lagrangian Eulerian (ALE) approach or the Immersed Boundary Method (IBM). In the former, the fluid domain is represented by a volume mesh, whose interface follows the imposed kinematic motion and whose inner part undergoes remeshing in cases of large deformations. In the IBM, a LV surface mesh is embedded in a 3D static Cartesian grid and the boundary conditions are imposed by a localized body force term in the Navier-Stokes equations. The advantage is that the flow solver can be simple and fast by using a Cartesian grid, whereas the weaknesses are the loss of accuracy and smearing out near the interface caused by the interpolations [124], [125]. In previous work, our group developed a patient-specific CFD model of the Left Ventricle (LV) [1] to investigate the fluid dynamics inside the LV chamber by means of an ALE approach, taking into account both the motion of the LV and MV starting from a 4D ultrasound dataset. The method, however, remains cumbersome and convergence is not always assured, often due to negative volume errors induced by the complex and large mesh motion, resulting in simulations restricted to one cardiac cycle.

From our perspective, we can overcome these limitations using the Chimera (or overset mesh) technique, which is particularly suitable in handling problems where different components are in motion, but has not yet been widely applied to cardiovascular problems. The Chimera technique decomposes the fluid domain in overlapping fluid grids, which exchange information via interpolation of the flow variables during the calculation. The main advantage, with respect to the ALE approach, is the capability of handling the separation of the fluid domain without requiring the local fictitious increase of viscosity or an added source term in the Navier-Stokes equations, which is a useful feature when simulating the closure of cardiac valves. With respect to the IBM, the major advantage is the possibility of representing complex geometries with boundary layer meshes [126]. On the other hand, the iterations performed between the overlapping grids to ensure that their solution is in equilibrium might increase the computational cost. In this regard, the primary aim of this study is to develop a robust workflow which allows building patient-specific CFD models based on the Chimera technique, to assess the LV fluid dynamics starting from clinical images and overcome the limitations of the previous model. This would allow us to assess also the sensitivity of calculated flow fields to the number of simulated cardiac cycles.

Furthermore, despite the main current limitations, this model can be useful to evaluate the effect that torsion may have on LV fluid dynamics. It has been shown that LV torsion is impaired or increased with cardiomyopathies, hypertrophy, diabetes, hypertension, ischemia and normal aging [127], and hypothesized that torsion is sensitive to changes in contraction and cardiac remodeling [128]. However, it is hard to assess the isolated effect of torsion from in vivo data [54], where pathology has an impact on the entire physiology of the ventricle, and not just on torsion. Torsional motion is commonly neglected in CFD models of the LV [1] and the induced effects on the LV fluid dynamics have never been investigated. Differently from a Tagged MRI sequence, which evaluates the entity of the ventricular wall strain and torsion [129], we want to use the proposed workflow to evaluate if the impaired torsional motion can induce alterations in the fluid dynamics that could be used as biomarker to early detect pathologies. Section 4.2 reports the CFD techniques used in LV modeling, with details of the steps of the workflow performed to build the CFD model starting from medical images (sections 4.2.1 to 4.2.6) and the choice of the flow variables used to analyze the flow field (section 4.2.7). The background-overset mesh combination was determined from a mesh sensitivity analysis (in Appendix 4.8). In the Results section, we report the comparison between the considered CFD cases.

4.2 Materials and methods

The framework used to build patient-specific CFD models starting from medical images can be summarized in six steps (Figure 4.1), each of which is detailed in the subsections below.

4.2.1 Medical imaging dataset segmentation

A cine-MRI short axis dataset of a healthy male volunteer of 27 years old was manually segmented (Materialise Mimics 18.0) to reconstruct the 4D LV endocardial surfaces in 30 time instants spanning 1 cardiac cycle. The acquisition of the medical images was performed using a Gradient Recalled Echo (GRE) sequence, with an in-plane and through-plane resolution (also known as slice thickness) of 1.17 mm and 8 mm, respectively. The study was approved by Policlinico San Donato with informed consent of the volunteer. In addition, a cine-MRI radial dataset of the same healthy volunteer was segmented (in-house Matlab-code developed by the Biomechs groups of Politecnico di Milano) to reconstruct the 4D annulus of the Mitral Valve (MV) with 18 planes rotating every 10° around the axis passing through the MV centroid and the LV apex. Also for the latter dataset, the in-plane resolution was 1.17 mm. The MV annulus was segmented from the cine-radial dataset in 30 time instants spanning one cardiac cycle. Nevertheless

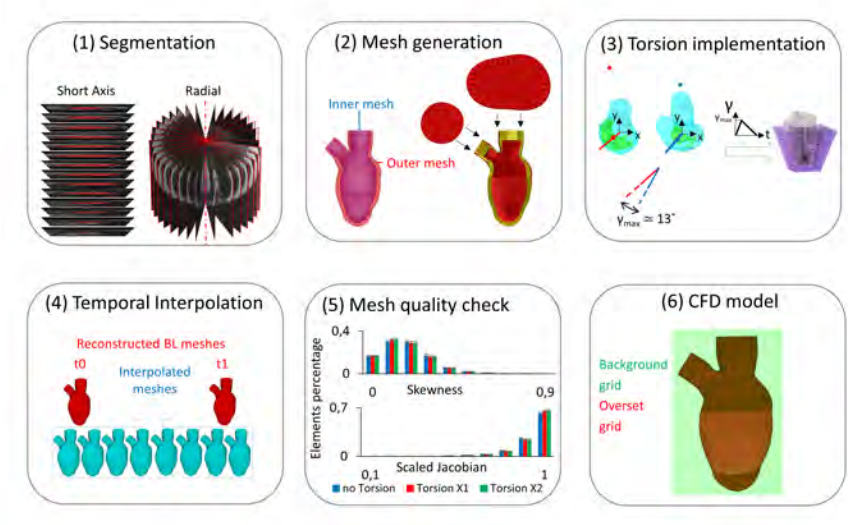

Figure 4.1: Workflow used to generate a patient-specific Computational Fluid Dynamics (CFD) model of the Left Ventricle (LV) based on the Chimera technique starting from medical images.

the motion of the MV annulus was not accounted for, it was kept in the static position obtained from averaging its 4D configurations over a cardiac cycle. The centroid of the MV annulus was computed using the built-in *centroid* function in PyFormex, an open-source in-house python based software. The *centroid* function returns the average coordinates of the points composing an object (curve or mesh).

4.2.2 Mesh generation

The Chimera technique decomposes the fluid domain in overlapping grids, in our case with (i) a fixed 3D Cartesian grid (background mesh), and (ii) a boundary layer mesh around the LV which moves and deforms every time step with the LV border and thus accounts for its motion (also called component mesh). Both meshes were generated in PyFormex. The 4D boundary layer multiblock structured mesh was generated using an updated version of a previously developed semi-automatic morphing tool [130] (reported in Chapter 3). In the 2.0 version, the tool is applied both to the outer part of the mesh (LV endocardium) [Figure 4.1.2, left, in red] and to the inner one by applying a scaling factor of 0.8 [Figure 4.1.2, left, in blue]. Then, taking advantage of the same numbering of the nodes of the two surface meshes, the boundary layer volume meshes were created using the built-in function *Connect*, which connects the nodes of the two meshes with a number of subdivisions specified by the user. Finally, two volume plugs were built for the inlet and outlet tracts in order to have a closed boundary layer mesh.

The Cartesian background mesh was generated using a built-in function which allows the user to create a structured hexahedral mesh. The number of elements of both the component and background meshes was tuned by using the PyFormex built-in function *SubdivideIsopar*, which allows the user to divide the elements of the mesh in a defined number of sub-elements. A mesh sensitivity study (reported in the Appendix 4.8) was conducted to choose the best combination between the density of the 4D boundary layer grid and the Cartesian one. In this study, the boundary layer mesh with 100k and 300k elements was coupled with a background mesh having an edge length of 0.5 mm and 0.7 mm.

4.2.3 Implementation of torsional motion

The motion of the LV endocardium can be decomposed in a perpendicular component, which determines the LV volume change, and a tangential component commonly referred to as torsion.

As our 4D boundary layer meshing method tracks the perpendicular component of the LV motion, but not the torsional one, torsion was superimposed on the perpendicular deformation. To do this, we first segmented the papillary muscles in end diastole and end systole, measured the torsional angle (gamma) as the circumferential angle enclosed by the papillary muscles centroid between end diastole and end systole. This measurement was done in the coordinate system where the mitral valve centroid is the origin; the vertical axis (z axis) points towards the apex; the y axis points towards the projection of the saddle horn at the vertical height of the origin (anterior-posterior direction); the x axis is oriented towards the posterior commissure (lateral-septal direction). Under the assumption that the shortening-elongation occurs along the defined vertical direction, the torsion has been computed as the rotation of the papillary muscles' centroid in the x-y plane (represented in Figure 4.13). The torsional angle was found to be 13° in our dataset. Torsion was subsequently imposed by means of a ramp-based function not directly to our 4D boundary layer meshes, but to the two scaled copies of the mapped shape (represented in Figure 4.13 in purple) used during the mesh generation of the LV sac to project the control points and also the mesh pattern. For a more extended explanation of the role of the two scaled mapped shapes and of the controls points the reader is referred to Ref. [130].

The presented workflow was used to investigate the effects of the torsional motion on the LV fluid dynamics by comparing three CFD cases with different degrees of torsion: (i) a case which takes into account only the perpendicular component, neglecting the torsional one (No Torsion); (ii) a physiological case which takes into account both the perpendicular and torsional component (Torsion X1); (iii) a case with a physiological perpen-

dicular component and a torsional one multiplied with a factor 2 to enhance the differences (Torsion X2).

4.2.4 Temporal interpolation

The temporal resolution of our imaging dataset, which corresponds to 30 time instants spanning one cardiac cycle, is not sufficient in order to fulfill an adequate temporal resolution for a CFD model. Therefore, a temporal interpolation of our 4D boundary layer meshes was needed. A Natural Cubic spline was chosen as interpolator function because the C2 continuity ensures the continuity and smoothness of the volume (V) and the flow rate ($Q = \frac{dV}{dt}$) waveforms. Based on our experience, the use of a cubic Bezier spline leads to discontinuities in the flow rate curve which resulted in convergence issues of the flow solver.

4.2.5 Mesh quality

The errors associated with negative volumes and convergence problems experienced by Bavo et al. [1] motivated us to perform the temporal mesh interpolation prior to the CFD calculation, so that we could check the quality of the 4D boundary layer mesh in every time step before starting the set-up of the CFD model. As quality parameters both the equiangle skewness (Qeas) and the Scaled Jacobian (SJ), defined in Chapter 3, were evaluated with threshold values set to 0.9 (max) and 0.02 (min), respectively [111]. The mesh quality check is performed both for the mesh sensitivity study and for the case study.

4.2.6 CFD set-up

Our CFD model is based on the Chimera technique, referred to as overset mesh approach in Fluent 18.2 software package, in which the fluid domain is represented by one moving component boundary layer grid embedded in a 3D Cartesian one. Once the overset boundary is defined and the overset interface is initialized, the cells of the meshes are categorized as follows:

1. Dead cells - if they lay outside the computational fluid domain;
2. Solve cells - in which the flow equations are solved;
3. Receptor cells - which receive the data interpolated from the donor cells of another mesh;
4. Donor cells - which send the data to the receptor cells and are a subset of the solve cells.

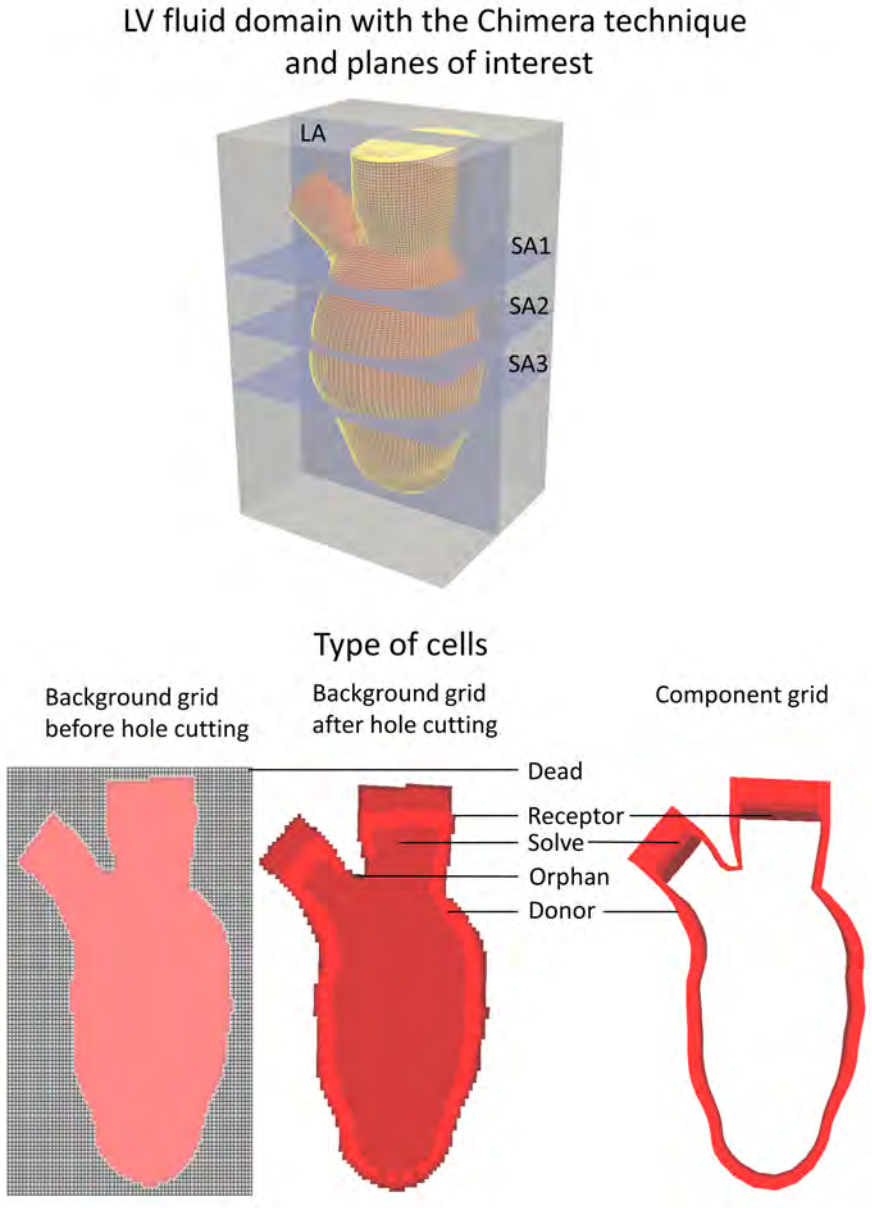

Figure 4.2: LV fluid domain modeling by means of the Chimera technique and location of the planes of interest (upper). Cells classification of the background and component grid for the Chimera technique in a case with meshes coarser than the ones used to show also the orphan cells (bottom).

Please refer to Figure 4.2 for a graphical representation.

The following operations are automatically performed by Fluent to define the type of cells and establish the connectivity between the participating zones. Firstly, the cells lying outside the physical boundary zones of the flow region are marked as dead cells (hole cutting). Secondly, if the cells can find a suitable donor cell with higher donor priority, the solve cells are converted into receptor cells and the unnecessary receptors are turned into dead cells (overlap minimization). Lastly, the domain connectivity between solve and receptor cells is established, with each receptor that should have one solve cell (donor search). Both meshes should have at least four or more cells in the direction perpendicular to the overlap boundary in order to have sufficient overlap. If the donor search fails, receptor cells are marked as orphan cells. In every time step, the connectivity between the zones is determined and the solver calculates the flow field by solving the Navier-Stokes equations. In terms of solver, a coupled scheme was used for the pressure-velocity coupling, while a 2^{nd} order upwind scheme was used for the convective terms and a 1^{st} order implicit scheme was used for time discretization. The 1^{st} order temporal discretization scheme was used because the Overset meshes technique, in case of dynamic mesh motion (referring to Fluent software versions 18.0 and 19 R3), is currently incompatible with the 2^{nd} order temporal discretization. The use of a 1^{st} order temporal discretization scheme instead of the 2^{nd} order scheme decreases the accuracy of the computed solution, but this can be mitigated by reducing the time step size.

Blood was modeled as a homogeneous and Newtonian ($\rho = 1060 kg/m^3$, $\mu = 0.003 kg/(m \cdot s)$) fluid. Due to the lack of patient-specific pressure waveforms, alternating on-off conditions were imposed at the inlet and outlet surfaces: the inlet pressure is set at 7 mmHg and the outlet is a wall during diastole, whereas the inlet becomes a wall and the outlet pressure is set at 120 mmHg during systole. Six cardiac cycles were simulated to study transient effects and cycle-to-cycle variation of the flow field and derived indices.

The simulations were run on a Dell Power Edge R620 server (2xIntel Xeon E5-2680v2 CPUs at 2.8 Ghz) using six cores, and one cardiac cycle lasted 30 hours.

4.2.7 Post-processing

The following variables were extracted from the simulations: velocity and vorticity magnitude along four short axis planes and one long axis plane (passing through the MV annulus centroid and the apex); the energy loss; the Residence Time (RT) using massless Particle Paths in the Tecplot software environment; and the WSS distribution. The velocity, vorticity, and WSS are compared in the end systolic configuration of every cardiac cycle, because

this is the time point when the difference in the torsional angles between the simulated cases is maximal. The residence time computation is based on the last two cardiac cycles to avoid the influence of the large flow field variations that occur in the initial cardiac cycles. The cycle-to-cycle variation are more extensively described in the results.

The energy loss and the energy power due to viscous dissipation occurring in the last two cardiac cycles were computed from the viscous portion of the incompressible Navier-Stokes equations to evaluate the influence of the different torsion degrees on the LV energetics. To calculate RT, stream tracers are first calculated at every time step of the simulation and then used to calculate the position of massless particles, of which the paths are calculated with an integration time equal to the time step of the simulation. 4500 particles are initially placed at the starting point of each stream tracer (located in the inlet surface) and the particle positions are advanced at every time step following the stream tracers corresponding to each time level. The integration for each particle continues until the final time level is reached or until the particle leaves the solution domain. Particles are classified in three categories as follows:

1. particles ejected within the first cardiac cycle ($0 < t < T$);
2. particles ejected with the second cardiac cycles ($T < t < 2T$);
3. particles remaining in the LV chamber after two cardiac cycles ($t > 2T$).

Furthermore, we reported the particles staying inside the LV chamber after two cardiac cycles colored by the velocity magnitude and their vectors, together with their distribution in function of the velocity magnitude for the three simulated cases. Note that first and second refer to the last two cycles. As Supplementary Material, a video showing the temporal evolution of the particles is available in Appendix 4.7. The WSS distribution is reported using the bull's eye representation, which divides the LV endocardial wall into 17 sectors.

4.3 Results

The manual segmentation of the 30 LV configurations throughout one cardiac cycle required approximately 3.5 h and the boundary layer meshes with 1-to-1 vertex correspondence were generated within 10 min. The density of the component and background meshes was chosen evaluating the accuracy of four mesh combinations for the CFD case which disregards torsion. Based on the results of the mesh sensitivity analysis (see Appendix 4.8), we decided

to use the finest resolution for both the background (edge length = 0.5 mm) and component meshes (number of cells = 300k).

In all three simulated cases, regardless of the torsional degree, we observed a large flow field variation in the first cardiac cycle with respect to the following ones and minor cycle-to-cycle variations in the other cardiac cycles. These minor cycle-to-cycle variations affected more the shape of the patterns rather than the peak value of the investigated quantity. These transitional effects occurred in all the three simulated cases and are reported for the case with physiological torsion (see Figure 4.3.

Because of these variations, the flow features of the three simulated cases are evaluated and compared during the last end systolic configuration. Considering the velocity field, one can observe from Figure 4.4 that the maximum velocity in the aortic tract is located in proximity of the posterior part of the aorta wall in the Torsion X2 case, whereas in the No Torsion case it is shifted towards the anterior part of the wall (visible in the long axis view).

For the physiological case, the peak is located in the middle of the aortic lumen, which suggests that torsional motion pushes the peak located in the aortic tract towards the anterior wall. Note that only the location of the maximum value is affected, not the maximum velocity magnitude. The shift of the peak velocity value towards the outer wall is also visible in the basal short axis slice (SA1). The Torsion X2 case also shows a wider extension of the areas where velocity is above 0.1 m/s in the basal and apical planes; compared to the reference solution: +69.7%, +34.2% is found, respectively (see Table 4.1).

ES	vel	[0.0, 0.1] m/s	[0.1, 0.2] m/s	[0.2, 0.3] m/s
SA1	NoT (mm^2)	655.9	529.0	1.30
	TX1 (mm^2)	945.8	309.4	11.6
	TX2 (mm^2)	728.1	536.9	7.8
SA2	NoT (mm^2)	955.9	28.2	0.0
	TX1 (mm^2)	886.7	108.5	0.0
	TX2 (mm^2)	872.5	102.3	0.0
SA3	NoT (mm^2)	501.6	156.2	0.0
	TX1 (mm^2)	548.0	110.8	0.0
	TX2 (mm^2)	510.6	148.7	0.0

Table 4.1: Extension of the contours (mm^2) at end systole based on ranges of the velocity magnitude [m/s], where *NoT*, *TX1*, *TX2* refer to the No Torsion, Torsion X1, Torsion X2 cases, respectively. The extension of the contours with a velocity greater than 0.1 m/s increases with the torsion degree only in the medial plane.

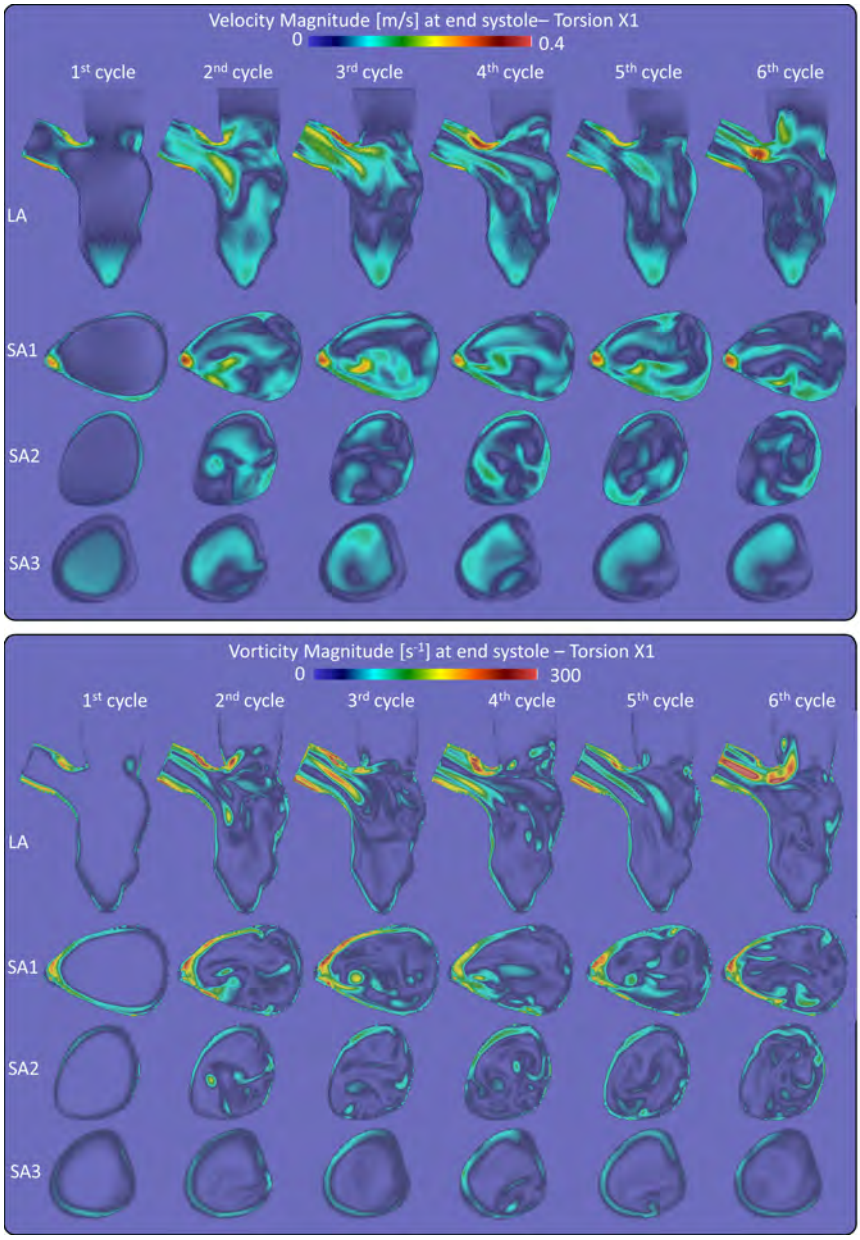

Figure 4.3: The cycle-to-cycle variation of velocity (upper) and vorticity (bottom) during the End Systolic (ES) configuration of the case with physiological torsion along the Long Axis (LA) plane and the three Short Axis (SA) ones. This behavior is irrespective of the torsion degree and it shows the importance of simulating at least two cardiac cycles to reach a stable solution.

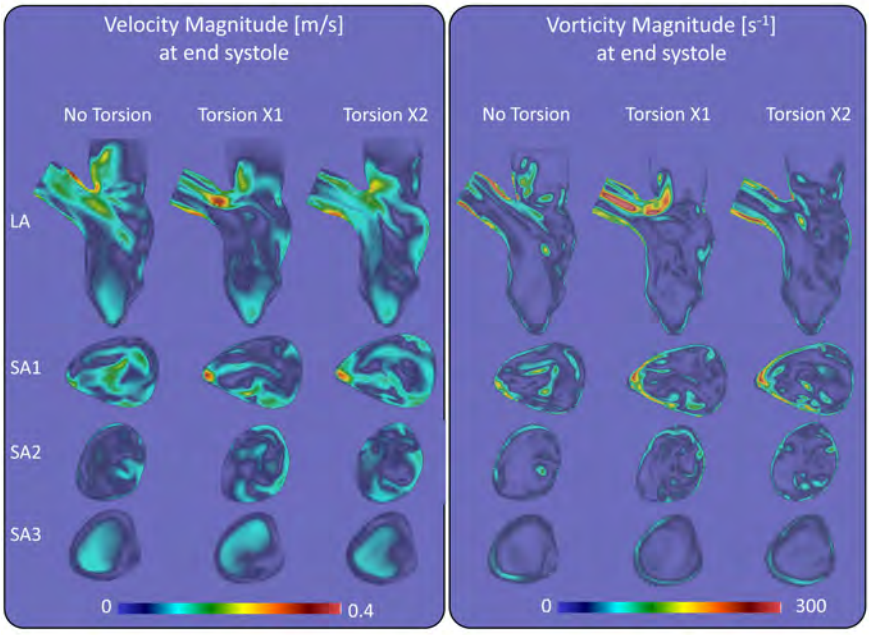

Figure 4.4: Velocity and vorticity in the three simulated cases to assess whether the torsion has an impact on the LV fluid dynamics. The torsional motion induces only minor differences in the extension of the spots associated with the peak values, but the maximum value of velocity and vorticity is not affected.

In the medial short axis plane (SA2) the resemblance of the Torsion X2 case with the reference solution is higher than the No Torsion case: the area associated with higher velocity is more extended in both torsion cases, especially in the proximity of the endocardial wall. In the apical short axis plane (SA3) there are no significant differences between the three simulated cases.

When investigating vorticity (see Figure 4.4 and Table 4.2, it is found that areas with vorticity > $200s^{-1}$ increase with the torsion degree in the basal plane. This area is reduced by -71.1% for the No Torsion case, while it increases by +3% in the Torsion X2 case (in comparison to the reference case). The threshold to detect swirling patterns was set at $50s^{-1}$ in the medial and apical planes because there were no areas with vorticity > $150s^{-1}$. The extension of areas with higher vorticity is reduced by -32.1% and -2.0% in the medial plane of the No Torsion and Torsion X2 case respectively, in comparison to the reference case. It increases with the torsion degree also in the apical plane: +20.1% and +7.4% in the No Torsion and Torsion X2 case respectively, in comparison to the reference case. Overall, differences are most pronounced when comparing physiological torsion with the No torsion

case; the additional effect of doubling torsion on the investigated parameter is much more limited.

The WSS does not change homogenously in all the sectors when increasing the degree of torsion (Figure 4.5). The mean WSS is proportional to the torsion degree in the basal lateral sectors and inversely proportional in the medial anterior sectors and in the apical anterior-septal sector. The maximum WSS is proportional to the torsion degree in the posterior and anterior-lateral basal sectors and inversely proportional in the posterior and septal-posterior medial sectors. In all the remaining sectors the WSS does not vary proportionally or inversely proportionally to the torsion degree.

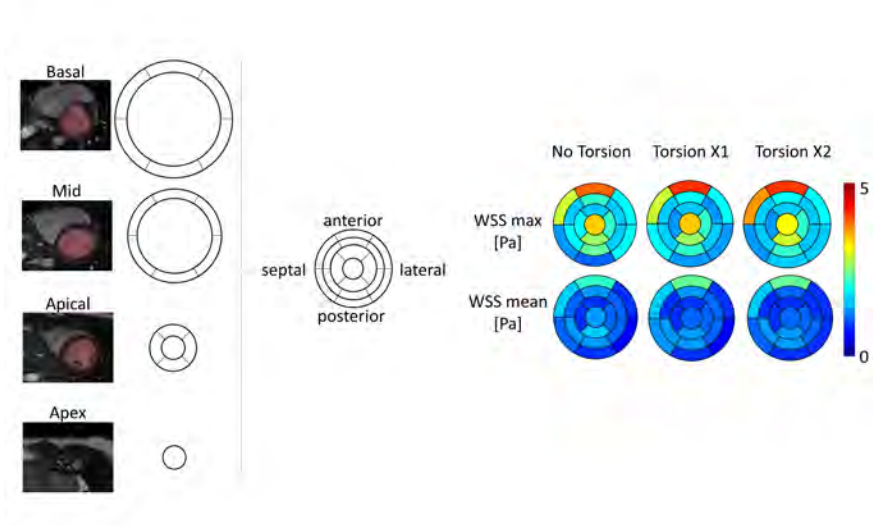

Figure 4.5: Corresponding Left Ventricular (LV) regions of the bull's eye model with 17 sectors, used to report the Wall Shear Stress distribution on the LV endocardium (left). Distribution of the maximum and mean WSS for the three simulated cases (right). Torsion does not induce a general homogeneous increase or decrease of the WSS.

The energy loss (Joule) is not affected by the different torsion degree, resulting in 0.0025, 0.0024, 0.0025 Joules in the No Torsion, Torsion X1 and Torsion X2 cases, respectively. This result in an average power of 1.4 mW in every simulated case.

Analyzing residence time (RT) (Figure 4.6), we found an increase of +7.9% of the particles with $t < T$ and a decrease (-3.0%) of the ones with $T < t < 2T$ for the case without torsion in comparison to the reference (see Figure 4.6a).

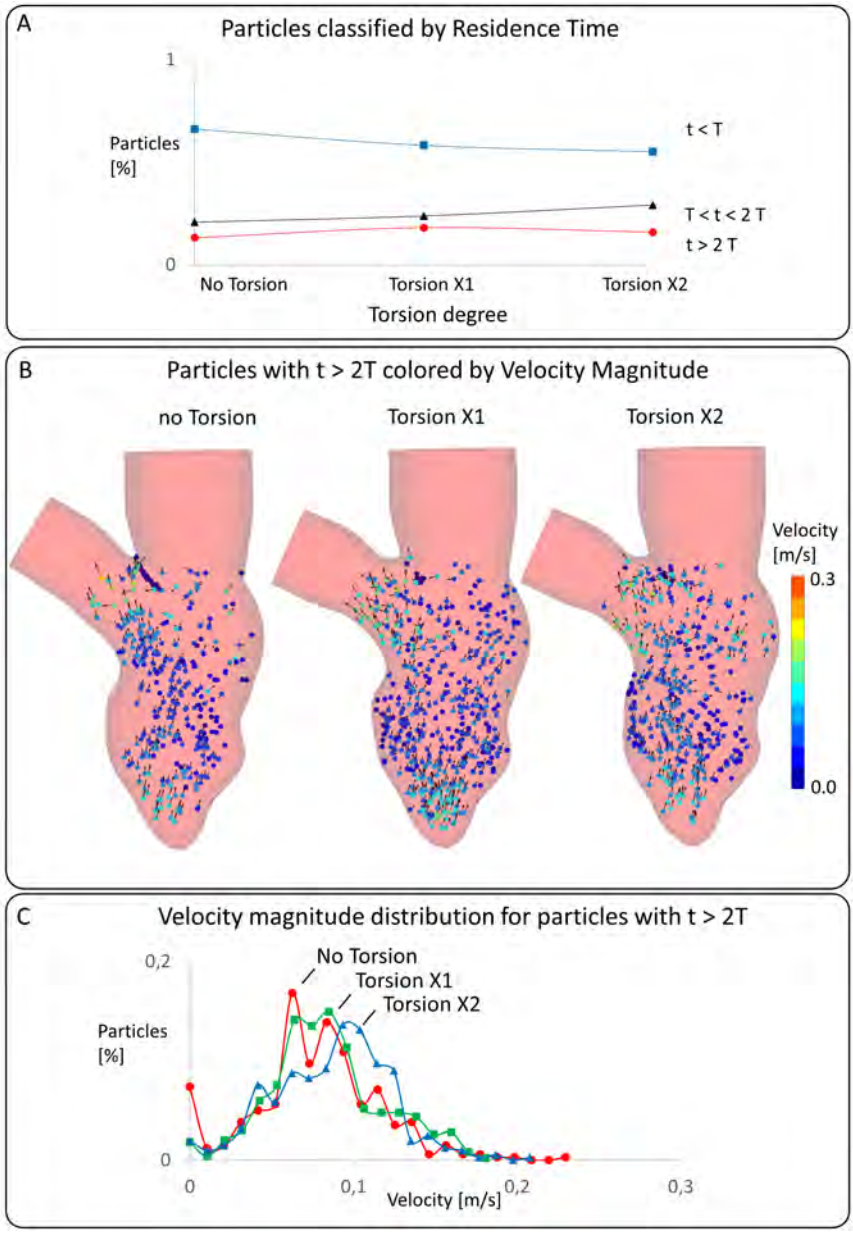

Figure 4.6: (A) Residence Time (RT) of the particles injected in the LV. The trend of the particles with $t > 2T$ does not increase nor decrease with the torsion degree, resulting in questions about the behavior of this class of particles. (B) The number of particles staying in the LV after two cardiac cycles is different in the three simulated cases, but no differences arise from a qualitative analysis of velocity magnitude and orientation of the vectors. (C) The distribution of the particles with $t > 2T$ in function of their velocity magnitude shows that the location of the peak value shifts towards higher velocity values by increasing the torsion degree.

ES	vor	[0, 50] s^{-1}	[50, 100] s^{-1}	[100, 150] s^{-1}	[150, 200] s^{-1}	[200, 250] s^{-1}	[250, 300] s^{-1}	[300, 350] s^{-1}
SA1	NoT (mm^2)	761.1	339.4	55.6	22.6	6.5	1.1	0.0
	TX1 (mm^2)	854.4	264.8	79.3	42.2	17.2	6.7	2.2
	TX2 (mm^2)	779.5	326.7	94.9	44.9	16.4	8.6	1.9
SA2	NoT (mm^2)	842.9	133.4	7.8	0.0	0.0	0.0	0.0
	TX1 (mm^2)	787.3	183.7	23.9	0.3	0.0	0.0	0.0
	TX2 (mm^2)	771.0	183.1	20.7	0.0	0.0	0.0	0.0
SA3	NoT (mm^2)	578.9	78.1	0.8	0.0	0.0	0.0	0.0
	TX1 (mm^2)	560.1	98.8	0.0	0.0	0.0	0.0	0.0
	TX2 (mm^2)	553.2	106.1	0.0	0.0	0.0	0.0	0.0

Table 4.2: Extension of the contours (mm^2) based on ranges of the vorticity magnitude (s^{-1}), where *NoT*, *TX1*, *TX2* refer to the No Torsion, Torsion X1, Torsion X2 cases, respectively. The extension of the contours with vorticity > 200 s^{-1} and vorticity > 50 s^{-1} increases with the torsion degree in the basal and apical planes, respectively.

Conversely, in the case with exaggerated Torsion, there is a decrease (-3.1%) of the particles with $t < T$ and an increase (+5.3%) of the ones residing $T < t < 2T$. Consequently, the number of particles residing less than 1 cardiac cycle seems to vary inversely with the imposed degree of torsion, whereas the number of particles residing $T < t < 2T$ increases with the torsion degree. Both cases without Torsion and with Torsion X2 show a decrease of the number of particles residing more than two cardiac cycles ($t > 2T$), -4.9% and -2.2% (Figure 4.6a), respectively in comparison to the reference case. The percentage of the particles with $t > 2T$ does not increase nor decrease with the torsional degree. Given that it is especially the long residing particles that are associated with an enhanced risk of thrombus formation, we focused on this class of particles.

Despite that the magnitude and direction of particles velocity are comparable between the three simulated cases (Figure 4.6b), the quantitative analysis

of the velocity distribution for the particles with $t > 2T$ added another perspective to our analysis. It is observed that the peak of the distribution of particles in function of velocity magnitude is shifted towards higher velocity values by increasing the degree of torsion (Figure 4.6c). Furthermore, when categorizing the particles in three classes based on the velocity magnitude values, we found that Torsion X2 leads to more particles with velocity between 0.1 and 0.2 m/s than the other cases (see Table 4.3), reducing the ones with velocity between 0 and 0.1 m/s.

4.4 Discussion

In this manuscript, we presented a workflow to generate patient-specific CFD models of the LV with moving boundaries based on the improvement of the patient-specific LV model based on the ALE approach developed by Bavo et al. [2], which encountered frequent negative volume errors and convergence problems and, therefore, was limited to only one cardiac cycle. The advantages of the Chimera technique over the ALE and IBM approaches are reported in the section CFD approaches in LV applications. As far as we know, only Al-Azawy et al. [131] used the Chimera technique to investigate the hemodynamics in a cardiac application, a pulsatile Left Ventricular Assist Device (LVAD) during one cardiac cycle. In the referred case, the overset mesh approach was adopted to handle the motion of both the pusher plate and the valve: the former by defining wall velocity equations during systole and diastole, and the latter as rigid rotation. The Chimera technique was chosen to provide more insight for shear stress and strain rate near the valves. This may particularly be fundamental in biomedical cardiovascular applications where local near-wall hemodynamic factors can discern between physiological and pathological conditions at the interface between the blood and the cellular interface, affecting mass transport processes and thrombus and clots formation. The advantage of the overset mesh in handling fluid

Velocity of residing particles	[0.0, 0.1] m/s	[0.1, 0.2] m/s	[0.2, 0.3] m/s
No Torsion (%)	75.8	23.9	0.3
Torsion X1 (%)	74.6	25.4	0.0
Torsion X2 (%)	60.7	39.1	0.2

Table 4.3: Distribution of the particles staying in the LV chamber after two cardiac cycles in function of their velocity. The case with exaggerated torsion has more particles in the velocity range between 0.1 and 0.2 m/s if compared to the other cases. This indicates that only an exaggerated torsion can enhance the motility of the particles staying the LV chamber after two cardiac cycles.

separation due to valve closure, as demonstrated in the study by Al-Azawy, is an important feature that will be useful when addressing the further development of our model, i.e., the inclusion of moving valve leaflets with valve motion obtained from fluid-structure interaction simulations.

Apart from the Chimera technique, we introduced the following modifications with respect to the Bavo et al. workflow to reduce the chances of getting mesh related problems: (i) the mesh motion, as creation of the 4D meshes with nodal correspondence and their temporal interpolation, is completely handled in PyFormex with the advantage that the mesh resolution can be tuned with built-in functions and the LV kinematics are assigned in Fluent by means of customized UDFs (2.0 version of the algorithm first presented in Ref. [130]; (ii) the elimination of the spatial interpolation, needed previously to translate the motion from the reference meshes to the mesh in Fluent, allows the user to have full control on all the nodes of the mesh; (iii) the quality check of the meshes is completely handled in PyFormex with the chance of intervening on the critical elements, if necessary, with customized scripts without manually repositioning the vertices with 3-matic (Materialise); (iv) the generation of multi-block structured boundary layer meshes, with respect to tetrahedral meshes, allows to have a finer control of the mesh resolution perpendicular to the LV endocardial wall.

To test the new workflow, while also addressing a valid research question, we set up a case study to assess the impact of torsional motion on the fluid dynamics inside the left ventricle, to evaluate if patient-specific CFD modeling can be used to early detect cardiomyopathies which induce a lack of or reduction in torsion. This was accomplished by applying our framework to three CFD cases characterized by different degrees of torsional motion (i.e. a simulation without, with physiological and with amplified torsion). A mesh sensitivity study (reported in the Appendix 4.8) was performed to choose the appropriate mesh density and the coupling between background (edge length= 0.5 mm) and component grid (300k cells). The physiological torsion was measured from the cine-MRI dataset (13° in our dataset) and, then, it was imposed on the mapped shapes used to generate the 4D boundary layer LV meshes by means of a ramp-like function. To better understand the role of the mapped shapes the reader is referred to the paper [130]. The value of 13° is consistent with the one found by Conti et al. [54], which proposed a method to compute the local myocardial strains and torsion based on nearest neighbor tracking and finite-element theory.

The new workflow turned out to be effective and robust for all three CFD cases, allowing the user to overcome the convergence problems and negative volume errors encountered with the previous methodology. Thanks to the newly reached robustness, it was also possible to simulate multiple cardiac

cycles, allowing us to study cycle-to-cycle variability of the calculated flow field and derived parameters. From our CFD simulations, we observed a significant difference between the flow field of the first cardiac cycle with respect to the following ones. Even though we chose a hybrid initialization - which solves the Laplace's equation to determine the velocity and pressure fields - over the standard one to start with conditions closer to the real operational conditions of the LV, the differences between the first and the following cycles suggest that at least one cardiac cycle is needed to limit these transitional effects. Nonetheless, some minor cycle-to-cycle fluctuations still occur in the successive cardiac cycles, indicating that the results obtained with the previous method - in which only one cardiac cycle was simulated - need to be interpreted cautiously. Chnafa et al. [117] earlier reported these cycle-to-cycle variations of the LV fluid dynamics; in their study, 5 cycles were simulated to washout the initial conditions and results were reported based on the phase-average over 30 additional cycles. We are aware that our analysis is based on the 5^{th} and 6^{th} cycle, but limitations in computational resources prevented us to calculate more cycles. Comparing the last cardiac cycle of the three simulated cases, we noticed minor differences regarding the contours of velocity and vorticity patterns, affecting only the extent of the spots associated with the peak values but not the magnitude of the maximum values. The extension of the areas associated with velocity > 0.1 m/s drops (more than 70%) in the No Torsion case in comparison to the cases with torsion in the medial plane, whereas it increases (by +69.7%, and +34.1%) in the Torsion X2 case, with respect to the reference solution, in the basal and apical plane. The vorticity magnitude decreases moving towards the apical zone in all three simulated cases. In the basal and apical plane it increases with the torsion degree whereas in the medial plane the No Torsion case is lower by more than 30% in comparison with the cases with torsion. The energy and power loss due to viscous dissipation were not affected by the different torsion degree, and resulted to be within the physiological range [132].

Several studies proposed different approaches to quantify the washout inside the left ventricle, but a direct comparison with those studies is complicated because their analysis is not based on residence time. Among these studies, Zheng et al. [133] computed the degree of mixing between atrial and ventricular blood cells and Seo et al. [100] simulated the transport and mixing of a contrast agent released in the apical region. Lastly, Selmi et al. [95] quantified the WSS at the LV apex to assess the thrombus formation inside the LV after implantation of a left ventricular assist device, imposing both perpendicular and torsional motion components by means of customized UDF in the Fluent software environment. Of those studies allowing for a direct comparison of residence time inside the left ventricle, both Hendabadi

et al. [121] and Mangual et al. [122] compared the washout of the left ventricle in patients with dilated cardiomyopathy compared to controls. The former based the computation on Lagrangian coherent structures starting from the 2D velocity field of color-Doppler echocardiography; the latter reported a blood transit curve that measures the percentage of stroke volume ejected after a number of heartbeats. In both studies, dilated cardiomyopathy induced a delayed ejection. In Hendabadi et al., the particles with a residence time ≥ 2 cycles are concentrated in the medial zone, similarly to the particles with velocity < 0.1 m/s of our simulated cases. In the study of Hendabadi et al., the direct flow percentage of the total diastolic inflow is significantly higher in the healthy cases than the pathological cases ($P < 0.01$). In Mangual et al., about 80% of the virtual tracer is ejected within two beats in the healthy cases (mean ejection fraction and stroke volume equal to 55% and 74 mL, respectively), while this value lowers to approximately 20% in the cases with DCM (mean ejection fraction and stroke volume equal to 17.8% and 41 mL, respectively). In our case study, all the three simulated cases have a percentage of direct flow comparable to the healthy cases of Mangual et al., so that the blood turnover in the cases with no and augmented torsions are not comparable with DCM cases of Mangual et al. Moreover, in our case the main difference occurs in the first systole, whereas the amount of particles ejected after two beats becomes comparable between the three cases.

To the best of our knowledge, no other studies investigated RT in the LV chamber in relation to ventricular torsion. We found that torsion reduces the number of particles staying less than 1 cardiac cycle at the expense of an increased number of particles residing in the LV with $T < t < 2T$, with no significant effect of the degree of torsion on the number of particles with $t > 2T$. When only considering residence time, one could conclude from these data that torsion reduces the washout of the LV chamber. Nevertheless, we believe that to fully understand the clinical relevance of the residence time in function of the torsion degree, it is important to take into account both the number of the particles remaining in the ventricle after a certain time (taken here 2 cardiac cycles) as well as their velocity distribution (which may actually play a more important role in the assessment of the risk of stasis).

The velocity distribution between the No Torsion and Torsion X1 case is highly comparable and only the Torsion X2 case reduces the number of particles with $velocity < 0.1\ m/s$, which are considered to be the ones more prone to stasis (Table 4.3). In a clinical scenario, the RT and the velocity distribution of the particles could be used to detect the predisposition to stasis. Our data indicate that torsion will have a significance only for supra-physiological values of torsion, but results should be confirmed in simulations including the motion of the mitral valve leaflets. If so, the implementation

of torsion could be neglected when building patient-specific CFD models for cases with physiological torsion, significantly reducing the complexity of the simulations. Furthermore, it is important to note that the presented CFD model disregards the MV leaflets and the Trabeculae Carneae. Therefore, even though our results suggest a minor impact of torsional motion on intraventricular flow, we cannot rule out that the combined effect of torsion, MV kinematics and trabeculae might lead to different results, particularly for the residence time. The kinematics of the MV leaflets will be evaluated as further development of the current model in an FSI simulation framework.

4.5 Conclusion

We proposed a new robust workflow to build a patient-specific CFD model of the LV with moving boundaries based on the Chimera technique to overcome the convergence issues due to mesh-distortions of a previous model based on the ALE approach. The workflow allowed us to (i) simulate the intraventricular flow field in successive cardiac cycles and (ii) to assess whether different levels of torsion yield meaningful differences in the left intraventricular flow field. We found important transient effects on hemodynamics, implying that it is mandatory to simulate multiple cardiac cycles when addressing intraventricular hemodynamics. On the other hand, the degree of torsion was found to have a minor impact on velocity, vorticity, wall shear stress and a null impact on the energy loss. Based on our results, torsional motion in CFD modeling of the LV can be discarded for physiological torsion levels. Nonetheless, given that the current model does not include the mitral valve apparatus nor trabeculae, further model extensions are required to confirm the presented results, which at the current stage need to be interpreted with caution.

4.6 Acknowledgment

This work was supported by the European Commission within the Horizon 2020 Framework through the MSCA-ITN-ETN European Training Networks (project number 642458).

4.7 Appendix: Supplementary material

Supplementary data to this article can be found online at Supplementary material.

4.8 Appendix: Mesh sensitivity analysis

A mesh sensitivity analysis was performed to choose the best coupling between background and component mesh for our CFD case study. The background grid (bg), perfectly isotropic, is named according to the edge length in mm, while for the component grid (cg) the number of cells is reported.

Four different mesh combinations were tested (bg0.7-cg100k, bg0.7-cg300k, bg0.5-cg100k, bg0.5-cg300k) by simulating 1 cardiac cycle with a time step of 3 ms with the CFD case which disregards torsion. The following variables were investigated to compare the results of the different meshes: (i) The distribution of the mean and maximum Wall Shear Stress (WSS) during the end-systolic configuration; (ii) The 95^{th} percentile of both the WSS and the endocardial pressure during the whole cardiac cycle; (iii) Pressure and velocity along a vertical and horizontal line during the end-systolic configuration.

In order to evaluate the best mesh coupling, the finest grid combination (bg0.5-cg300k) was taken as reference solution to evaluate the studied variables (see Figure 4.7. In terms of WSS distribution, it is visible how the mesh combination (bg0.7-cg300k) has a closer similarity to the reference solution, suggesting that the accuracy of the WSS evaluation relies upon a finer component mesh rather than a finer background mesh. The importance of the WSS in biomedical applications to determine zones prone to thrombus formation (low WSS) and to cell damage (high WSS), would lead us to choose the finest component grid (cg300k). From the temporal evolution of the variables on the LV endocardial wall, we observed two different trends: a good match between all the meshes if considering the pressure, while from the WSS perspective once more the mesh combination (bg0.7-cg300k) has a closer similarity to the reference solution.

Regarding the pressure and the velocity along lines, the mesh combination (bg0.5-cg100k) is the most similar to the reference solution in 3 out 4 cases, with the only exception being the velocity along the vertical line where the mesh combination (bg0.7-cg300k) is closer. Without having a unanimous sign that suggests the best mesh combination for all the evaluated variables, we decided to choose the finest grid combination (bg0.5-cg300k).

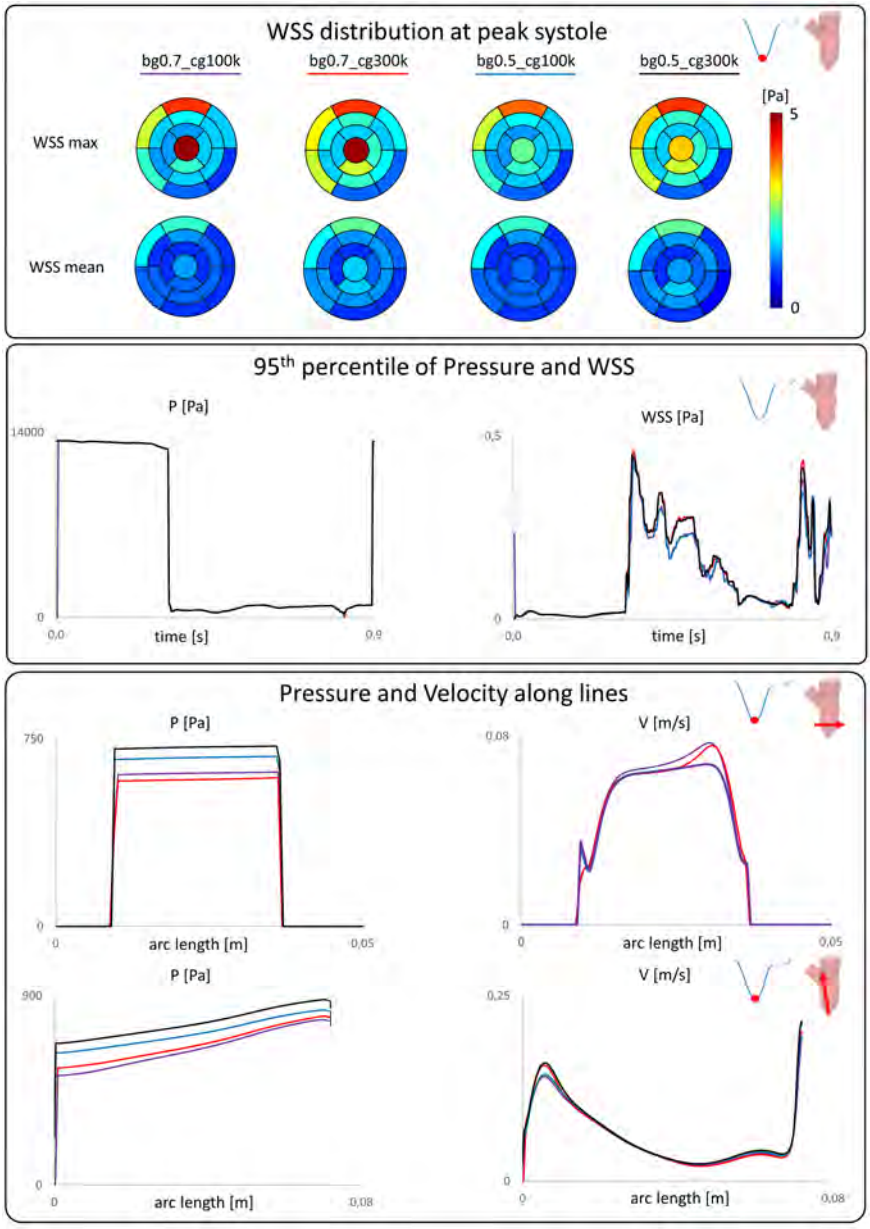

Figure 4.7: The mesh sensitivity study - performed on four mesh combinations - shows a different behavior for the investigated quantities. The accuracy of the WSS is affected more by the density of the component grid (cg) rather than the background grid (bg), whereas the accuracy of the quantities computed inside the fluid region (pressure and velocity) relies more on the bg. WSS and the Residence Time (which is computed from the velocity field) are equally important for our analysis, therefore we chose the mesh combination with the highest density for both the cg and bg.

Chapter 5

A CFD study on the interplay of torsion and vortex guidance by the mitral valve on LV wash-out

This chapter introduces the methodology used to assess the impact of the mitral valve kinetics and torsional movement on a patient-specific Computational Fluid Dynamics (CFD) model of the Left Ventricle (LV) hemodynamics. The CFD study was conducted by using the semi-automatic meshing tool and the Chimera methodology previously reported in chapters 3 and 4, respectively. The strategy used to implement the kinematics of the mitral valve is reported in the following sections. The contents of this chapter is in preparation for submission to a scientific journal.

5.1 Introduction

Cardiovascular disease is the main cause of death worldwide, accounting for 17.8 million deaths expected to increase up to 23.6 million by 2030 [3]. Most often, this entails a chronic process whereby pathophysiological changes in cardiac function progress slowly (e.g. development of cardiac hypertrophy, cardiac dilatation, valvular dysfunction) and unnoticed, until reaching a point of no return with the development of symptoms, or occurrence of a fatality as myocardial infarction or stroke. In many cardiovascular pathologies, unphysiological intraventricular hemodynamics is a consequence and/or direct cause of the pathology (e.g. valve dysfunction), leading to flow disturbing

and energy dissipating jets, altered intraventricular swirling patterns with less energy-efficient filling and emptying of the ventricular chamber, and effects on blood residence times within the cardiac cavity. Furthermore, therapeutic interventions – especially those related to resting valve function, may drastically alter flow patterns within the heart cavities. A fundamental understanding of intraventricular hemodynamics should lead to an improved assessment of deviations from normal physiological flow, earlier detection of chronic abnormalities, better assessment of therapeutic efficacy, and further refinements in surgical techniques or cardiovascular medical device design.

Among the techniques used to investigate the intraventricular flow field, Computational Fluid Dynamics (CFD) modeling outstands over the in-vivo imaging modalities and the in-vitro benchmarks to perform fast parametric and comparative studies, thanks to the relentless improvement of computational power and the growth of computational models. Therefore, it would be paramount if patient-specific CFD simulations could finally reach the development to be used as a clinical support tool in cardiovascular surgical planning and diagnostics. CFD modeling has been used extensively to study several cardiovascular applications, among which: the investigation and early detection of numerous cardiovascular diseases (heart failure conditions, pulmonary hypertension, aortic and cerebral aneurysms, aortic dissection, cardiac valve pathologies), the assessment of cardiovascular devices and therapies (prosthetic valves, stent and ventricular assist device placement, cardiac resynchronization therapy) [134].

Computational modelling of intracardiac hemodynamics faces multiple challenges intrinsic for the cardiac physiology including the large motion of the endocardium, the superficial irregularities due to the trabeculae and papillary muscles, the transitional-to-turbulent flow state and especially the impulsive kinematics of the cardiac valve leaflets. It is, for instance, well known that the configuration and kinematics of the mitral valve (MV) leaflets are crucial for the development of the diastolic asymmetric vortex ring within the left ventricle (LV), which is a key feature in terms of wash-out of the ventricular chamber and ventricular energetics [135]. Furthermore, they reduce the effective orifice area and increase the vortex formation length, with the vortices developed from the free edge of MV leaflets instead of the annulus [100]. The MV leaflets motion can be computationally replicated via a kinematic model, preferably based on measurements from 4D medical images, or a Fluid-Structure Interaction (FSI) model [67].

The first generation of kinematic models considered the MV using an on-off approach [92], [97], [136] or as a time-varying planar orifice [91], [92], [99], which both neglected the MV leaflets' configuration and kinematics. Later models implemented both the morphology and the motion of the leaflets with

different degrees of accuracy and they can be classified in the patient-inspired or patient-specific MV models. Among the patient-inspired MV models: (i) Chnafa et al [57], [58], [117] segmented the moving MV annulus from 4D CT scans and modeled the MV leaflets as a continuous elliptical shape with a given thickness, which instantaneously switches between the open and the closed configuration, thus neglecting the opening and closing phases; (ii) Seo et al [71] defined the MV morphology based on the anatomical measurements by Ranganathan et al [101] with the Anterior (AL) and Posterior (PL) leaflets following rigid rotations with different angular profiles. Contributions among patient-specific MV models are: (i) Mihalef et al [90] modeled the whole heart using machine-learning algorithms to robustly estimate the patient's morphological and functional parameters from multiple 4D CT datasets with claimed precision of 90%; (ii) Bavo et al [1] segmented the LV and MV kinematics from 4D transesophageal echocardiographic images.

Even though patient-specific MV models based on 4D medical images can account for the fluctuations and curvature changes, the limited thickness and highly impulsive kinematics of the leaflets pose substantial obstacles to overcome in terms of imaging modalities with adequate spatial and temporal resolution able to capture the opening/closing phases. A whole branch of research is dedicated to combining the different imaging techniques to enhance their advantages [137]. Among recent cardiac imaging techniques, 4D flow MRI looks promising in the quantification of the flow directly from clinical images but still suffers from a coarser spatial and temporal resolution in comparison with CFD and FSI simulations [138].

On the other hand, FSI modeling requires: (i) the definition of the constitutive and structural properties, which is more straightforward for materials composing prosthetic mechanical valves rather than the natural leaflets; (ii) a finer description of the MV anatomy including the details, such as the chordae tendinae and papillary muscles, not essential in kinematic models. For these reasons, patient-specific FSI models coupling the LV and MV rarely succeeded to combine simultaneously multiple features: the patient-specific LV model with both mitral and aortic valves by Su et al [123] is limited to a 2D geometry, otherwise the 3D MV is placed within a fixed tube [139] or limited to the filling phase [140]. Recently, there have been few breakthroughs in coupling patient-specific MV and LV models with FSI and they have been used to study the effects of impaired myocardial active relaxation [141] or the transapical neo-chordae implantation [142], [143].

Regardless of whether the MV kinematics is prescribed in CFD simulations or calculated in FSI simulations, the computational approaches typically used to solve the flow (and structural) equations of problems involving moving meshes can be boundary-conforming, such as the Arbitrary Lagrangian-Eulerian (ALE) approach, or non-boundary conforming, such the Immersed

Boundary Method (IBM). In the former, the boundary mesh deforms accordingly to the motion of valves in providing an accurate WSS computation on their surface. In the latter, the effect of the moving immersed body on the fluid is taken into account by adding a source term in the Navier–Stokes equations resulting in a more suitable approach for complex geometries. In addition to these most common techniques, one has to mention: the smoothed particles hydrodynamics, which is a meshless approach used successfully to overcome the lack of complete valve coaptation during systole [144], [145]; the Chimera (or overset) technique, which is particularly suitable in handling problems with different components in motion, used to investigate the hemodynamics within a pulsatile left ventricular assist device [131]. The Chimera technique has the advantage over ALE that it allows tackling the separation of the fluid domain that occurs during the valve coaptation without a local fictitious increase of viscosity or added source term in the Navier-Stokes equations, whereas, over the IBM approach, complex geometries can be represented with boundary layer meshes resulting in a more accurate computation of interface wall shear stress.

In previous work, we built a patient-specific CFD model of the LV chamber based on the Chimera technique. Firstly, we generated a semi-automatic algorithm to generate 4D meshes of the LV with 1-to-1 vertex correspondence to replicate the patient-specific cardiac motion [130]. Secondly, we investigated the impact of the LV torsion on the fluid dynamics using the Chimera technique [42]. A major limitation of that study, however, was the absence of the mitral valve in the model, known to highly impact the intraventricular flow field and a key structural element in the formation of the ventricle-filling vortex ring in diastole. Therefore, the aim of this study is to test the Chimera technique in a patient-specific CFD model of the LV in combination with a kinematic model of the MV. Bearing in mind that many cardiac pathologies (cardiomyopathies, hypertrophy, diabetes, hypertension, ischemia, normal aging) have an effect on ventricular torsion, simulations are performed in a model with and without physiological torsion.

5.2 Materials and Methods

5.2.1 Medical imaging dataset segmentation

The heart of a 27 years old healthy male volunteer was scanned using a cine-MRI short-axis dataset and a cine-MRI radial dataset at the Policlinico San Donato using a Gradient Recalled Echo (GRE) sequence within 30 time-instants spanning 1 cardiac cycle. The study was performed with the ethical approval of the hospital and the informed consent of the subject. The short axis dataset had an in-plane resolution of 1.17 mm and a through-plane resolution of 8 mm, whereas the radial dataset shared the same in-plane resolution

and was acquired every 10° along the rotation axis passing through the LV apex and MV centroid. The 4D geometries of the LV were manually segmented using Materialise Mimics 18.0 from the cine-MRI short-axis dataset, while the 4D annulus and one configuration of the leaflets at the A-wave peak, due to high uncertainty linked with the highly impulsive leaflets and motion artifacts, were segmented from the cine-MRI radial dataset within an in-house Matlab-code developed by the Biomechs groups of Politecnico di Milano (Figure 5.1A).

5.2.2 Mesh generation

With the Chimera technique, the shape of the fluid domain is described with one or multiple component Boundary Layer (BL) grids attached to the moving walls that are overlapping a 3D Cartesian grid. This feature is particularly helpful to represent complex deforming geometries. In this section, we describe the steps taken to generate three component grids (Figure 5.1C, right): (i) one anterior MV mesh connected conformally to the anterior part of the LV mesh; (ii) one posterior MV mesh connected conformally to the posterior part of the LV mesh (posterior LVMV mesh, shown in green) and (iii) an inlet plug mesh overlapping with both LVMV meshes to close the fluid domain.

The surface mesh of the MV leaflets is generated by connecting the MV annulus, modeled in a static configuration defined from the averaging of its 4D configurations over a cardiac cycle, with the profile of the MV free edge of the valve at the A-wave peak (Figure 5.1A). The anterior and posterior BL MV meshes were created around the MV surface, bearing in mind that they represent the fluid region in contact with the MV surface mesh, and the steps are thoroughly reported in the Mesh generation section of the Supplementary Material 5.7.

We enabled manual cut-control and ensured that the overset interface occurred along a vertical between the anterior and posterior LVMV meshes wall and along a horizontal between the inlet plug and the anterior and posterior LVMV meshes. The overlapping between the component grids was conformal on the external surface of the three boundary layer meshes. The final three component grids are displayed in Figure 5.1C (anterior LVMV mesh in red; posterior LVMV mesh in green and an inlet plug mesh overlapping with both LVMV meshes to close the fluid domain in blue).

The rotation angles were not assigned homogeneously to the leaflets, but via a shaping function that divided the MV into four zones (anterior and posterior leaflet, front and posterior commissure) (Figure 5.2). The finer control was essential to leave more space during early diastole between the MV leaflets and the LV wall in correspondence of the commissures, which

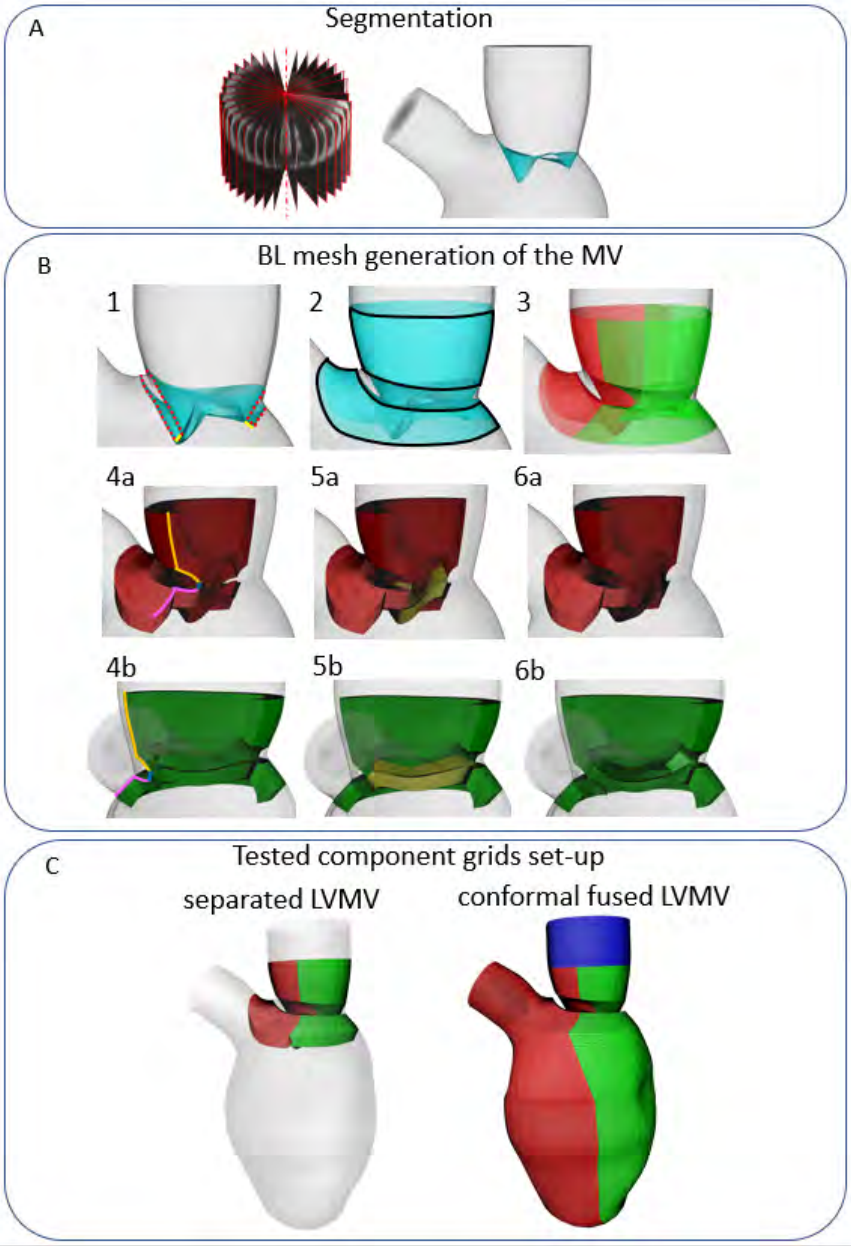

Figure 5.1: (Panel A) Mitral valve segmentation from cine-radial MRI images; (Panel B) Creation of the mitral valve mesh; (Panel C) Tested meshes configurations: not-working separated LV-MV configuration on the left, working conformally connected fused LV-MV on the right.

otherwise would have been too narrow to fit the valve. The quality criteria used for the 4D generated meshes are a maximum skewness of 0.9 and a minimum scaled Jacobian of 0.02. The number of mesh elements are 737 k, 496 k, 346 k, 2.5 M for the anterior LVMV grid, the posterior LVMV grid, the inlet plug, and the background grid, respectively.

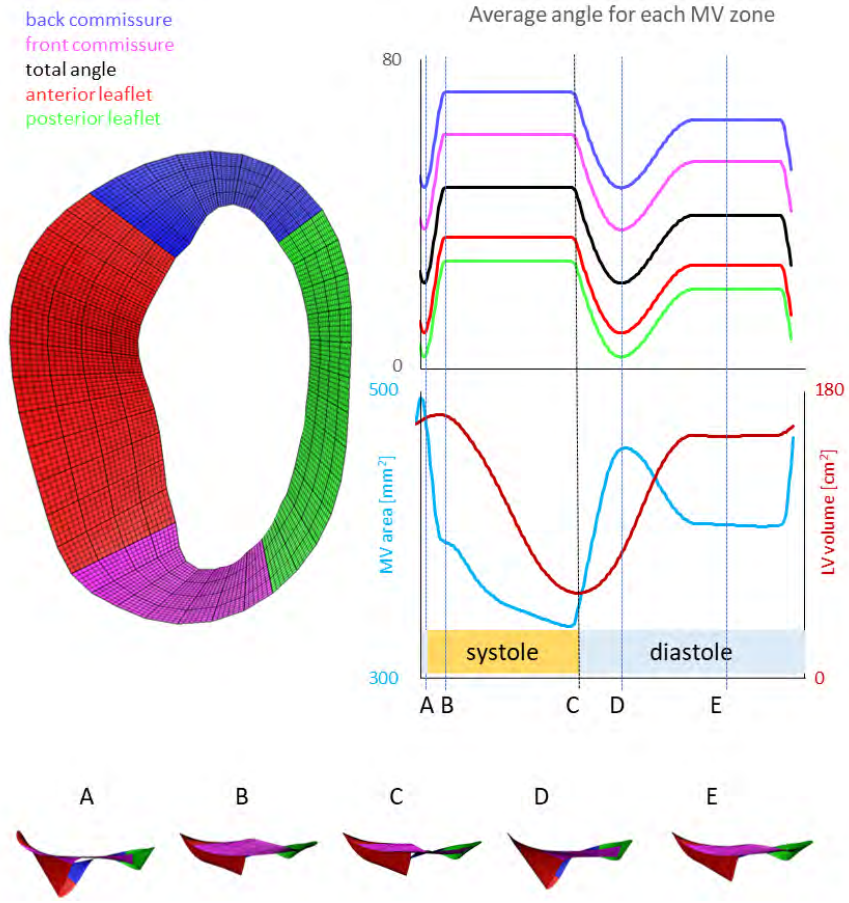

Figure 5.2: Kinematic model of the mitral valve reporting the average angle for each zone of the valve. (left) Parts composing the MV mesh are reported with different colors; (right, above) Opening angle of each part composing the MV; (right, bottom) MV orifice area and LV volume

5.2.3 Torsional implementation

Torsion was implemented on the anterior and posterior 4D BL LV split mesh as in [130]. We simulated physiological torsion (referred to as *Torsion*) with a maximum torsion angle $\gamma = 13^{\circ}$ as derived from medical images (angle encompassed by the centroid of the papillary muscles between end-systole and end-diastole, see [130]). In a second simulation, torsion was omitted (referred to as *No Torsion*).

5.2.4 Temporal interpolation

The anterior and posterior LVMV meshes were generated on the existing and already interpolated 4D BL meshes of the LV using a Natural Cubic spline, resulting in 290 temporal configurations spanning one cardiac cycle and a time step of 3 ms. For more details on the temporal interpolation method, the reader is referred to [130] reported in Chapter 3.

5.2.5 CFD setup

Our Chimera-based CFD model was defined in Fluent 2019 R3, with the fluid domain represented by three BL component grids (anterior LVMV, posterior LVMV, inlet plug) embedded in a 3D Cartesian grid. The initialization of the overset interface subdivided the cells of the meshes into four categories (dead, solve, receptor, donor) and established the connectivity between the participating zones to exchange variables during the computation of the Navier-Stokes equations. The cut-control feature was required for finer control on the cells to disable (dead cells), allowing to specify the wall zones not to be cut by the fluid zones. In our case, the wall zones of the anterior and posterior LVMV meshes were excluded from the cutting of the posterior and anterior fluid zones, respectively.

As in [42], a coupled solver scheme was used for the pressure-velocity coupling, together with a 2nd order upwind scheme for the convective terms and a 1st order implicit scheme for the time discretization. Blood was modeled as a homogeneous and Newtonian fluid ($\rho = 1060 \frac{kg}{m^3}$, $\mu = 0.003 \ \frac{kg}{m \cdot s}$).

Alternating on-off boundary conditions were imposed as follows: inlet pressure set at 7 mmHg and outlet as a wall during diastole; outlet pressure set at 120 mmHg and inlet as a wall during systole. Six cardiac cycles were simulated on a Dell PowerEdge R620 server (2×Intel Xeon E5-2680v2 CPUs at 2.8 GHz) and the HPC-UGent cluster system. In the former, one cardiac cycle was computed in about 24 hours using eight cores. In the latter, the computation time depended on the number of nodes and architecture of the available cluster unit.

5.2.6 Post-processing

The comparison of the fluid dynamics in the simulated cases was based on the computation of the velocity and vorticity magnitude, the energy loss (EL), the wall shear stress (WSS) distribution, and the Residence Time (RT). The velocity and vorticity are separated into classes (reported in Tables 5.1 to 5.6 in the supplementary material 5.7) in ascending order according to the magnitude to quantitively assess the differences of the contours and are evaluated in three short-axis planes (SA1, SA2, SA3, from top to bottom) and one long axis plane (LA). The EL is computed from the viscous term of the incompressible Navier-Stokes, as reported in equations 5.1 and 5.2, where $\frac{1}{2}\left(\frac{\partial \boldsymbol{u}_i}{\partial \boldsymbol{x}_j} + \frac{\partial \boldsymbol{u}_j}{\partial \boldsymbol{x}_i}\right)$ represents the strain deformation rate in the fluid domain, V_i the volume cell of the background grid ($V_i = 0.343 mm^3$), and μ the blood dynamic viscosity ($\mu = 0.003 \frac{kg}{m \cdot s}$).

$$\phi_V = \frac{1}{2}\mu \sum_{i=1}^{3}\sum_{j=1}^{3}\left[\left(\frac{\partial \boldsymbol{u}_i}{\partial \boldsymbol{x}_j} + \frac{\partial \boldsymbol{u}_j}{\partial \boldsymbol{x}_i}\right)\right]^2 \tag{5.1}$$

$$E_L = \int_{to}^{t1} \sum_{i=1}^{num\ \text{voxels}} \phi_V V_i \tag{5.2}$$

Regarding the RT, 4500 massless particles were seeded in the inlet and moved along the velocity field of every time step during the last two cardiac cycles, using the particle paths computation in Tecplot 360 EX 2019 R1. For the RT computation, the particles were classified into three categories: (i) ejected within the 1st beat (direct flow); (ii) ejected within the 2^{nd} beat; (iii) residing in the LV after 2 beats.

Both the EL and the RT were evaluated during the 5^{th} and 6^{th} cardiac cycles, whereas the remaining variables during characteristic time-points of the 6^{th} cardiac cycle. The chosen characteristic time-points were the diastolic E-peak and A-peak and end-systole.

The cycle-to-cycle variation was estimated by computing the median, 5^{th}, and 95^{th}percentile of velocity and vorticity magnitude, pressure, and velocity components, within three spherical cloud points (N_{points} = 1000 points, radius = 5 mm) distributed along the axis passing through the MV centroid and the LV apex.

In addition to studying the impact of torsion, we also compared results to a case without the presence of the MV.

In the bulls' eye representation, which divides the LV endocardium into 17 sectors, we reported the mean and maximum WSS as the difference in every

sector between the investigated cases (Torsion – No Torsion, LVMV - LV) to highlight visually the zones impacted by Torsion and the MV. Visually, the first case (Torsion, LVMV) dominates in the red zones, whereas the second case (Torsion, LV) in the blue zones.

5.3 Results

5.3.1 Influence Of Torsion On Intraventricular Hemodynamics

Figure 5.3 displays median values of velocity (components), pressure, and vorticity as a function of time within the three control volumes for the reference case with physiological torsion and the presence of the mitral valve. Cycle-to-cycle variation is still prominent after six cardiac cycles, especially for vorticity and y and z components of velocity.

At the E-peak of diastole (Figure 5.4, upper panel), the inlet jet reaches the peak velocity magnitude of 2.0 m/s with the formation of two vortical structures that impinge the posterior endocardial wall in every simulated case. Both the velocity and vorticity distributions are highly comparable between the Torsion and No torsion case (Tables 5.1 and 5.2, respectively). Omitting torsion leads to a slight increase in velocity magnitude in the long axis (LA) and SA1 planes and a mild decrease in the SA3 plane; a slight increase in vorticity is found in the SA1 plane. Torsion increases the maximum WSS in the apical region by 2-3 Pa, whereas it lowers it with the same intensity in the basal and medial sectors, and by 0.9 Pa in the apex. WSS increases in the No Torsion case in the anterior medial sectors (around 1 Pa), while it decreases (-0.6 Pa) in the lateral apical sectors.

At the diastolic A-peak (Figure 5.4, bottom panel), two main features can be noted regardless of the torsional degree: (i) both the peak of velocity (0.7 m/s) and vorticity (800 s^{-1}) lost intensity; (ii) the two main E-peak vortex structures dissipated into smaller vortices more uniformly distributed in the LV domain. Disregarding torsion induces a mild increase in velocity magnitude in the LA, SA1 and a moderate increase in the SA3 plane (Tables 5.3 and 5.4, respectively). The WSS max increases when disregarding torsion in the apex by 1.2 Pa, whereas it mildly reduces in the basal and medial sectors. Discarding torsion has a dual effect on the apical region, increasing by 2-3 Pa in the septal and posterior sectors and decreasing of the same intensity in the remaining apical sectors. Regarding the mean WSS, the basal septal-posterior sectors and the apical septal sector increases by 1 Pa.

At the end-systolic configuration (Figure 5.5, upper panel), the maximum velocity magnitude is around 0.65 m/s and 0.43 m/s, whereas the vorticity magnitude reaches 680 s^{-1} and 520 s^{-1} in the No Torsion and Torsion case, respectively. Omitting torsion leads to a mild increase of velocity and vorticity

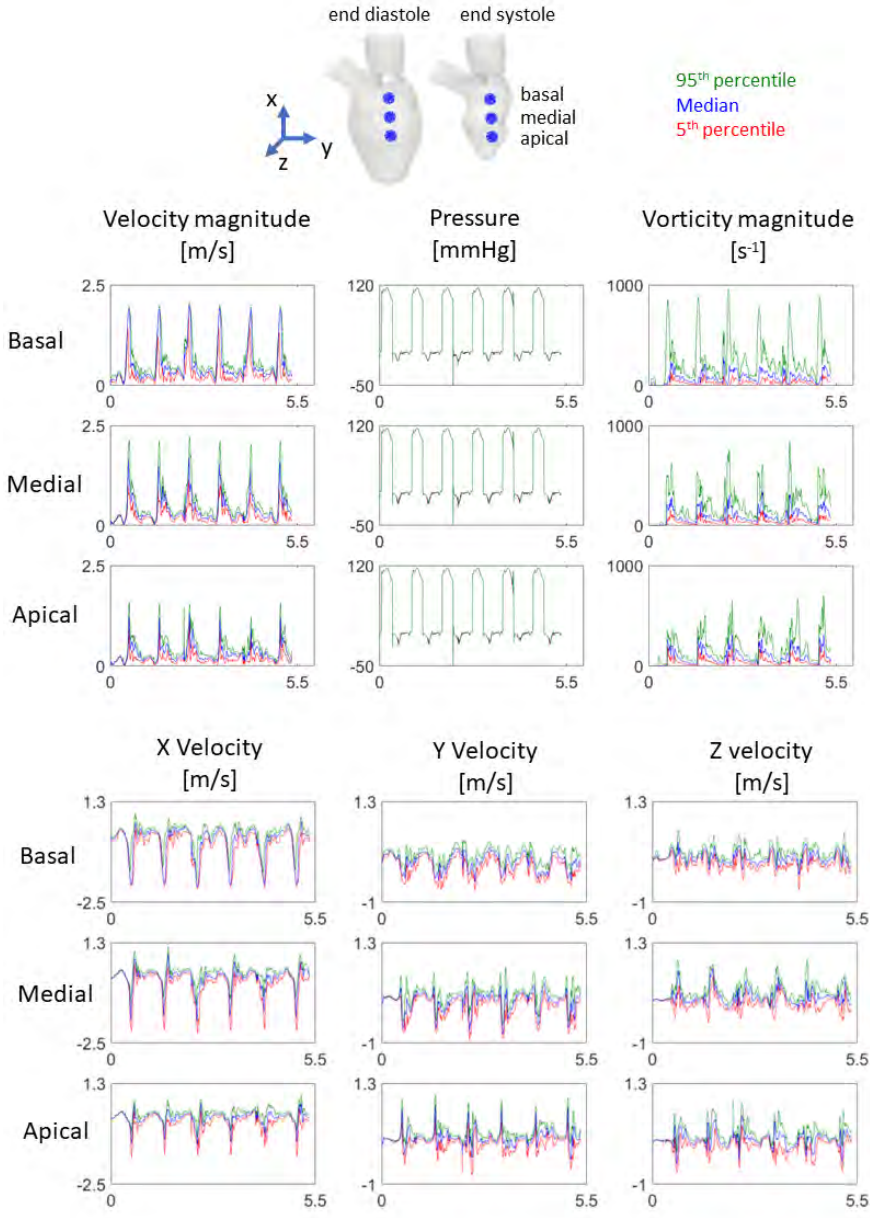

Figure 5.3: Cycle-to-cycle variation (reported for the velocity magnitude, pressure, vorticity magnitude, and velocity components) in the investigated cloud points shows that the transitional effects are still relevant.

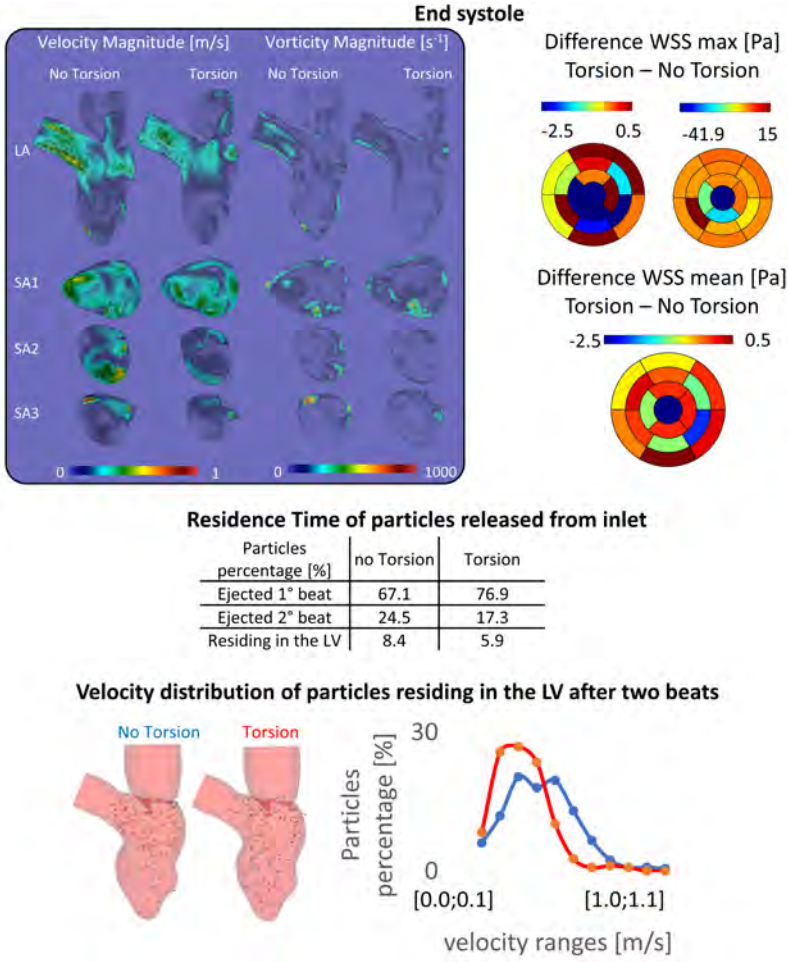

Residence Time of particles released from inlet

Particles percentage [%]	no Torsion	Torsion
Ejected 1° beat	67.1	76.9
Ejected 2° beat	24.5	17.3
Residing in the LV	8.4	5.9

Figure 5.4: Velocity, vorticity and wall shear stress at the diastolic peaks (Epeak above and Apeak below) show a marginal impact of torsion on the investigated variables.

magnitude in all the investigated planes, but confined to small areas (Tables 5.5 and 5.6). The lack of torsion, even if highly localized, increases the max WSS by 41.9 Pa in the apex, decreases it by 15 Pa and 7 Pa in the medial posterior-septal sector and in the remaining sectors, respectively. In terms of mean WSS, torsion decreases it by 2.5 Pa in the apex whereas increases it mildly (0.5 Pa) in the remaining. Energy dissipation (EL) is about 14% higher for physiological torsion (9.7 mJ) over cycle 5 (4.8 mJ) and 6 (4.8 mJ) than when torsion is omitted (8.4 mJ), with 4.1 mJ in cycle 5 and 4.3 mJ in cycle 6.

Figure 5.5 encompasses the results that were obtained on particle residence times. When particles are released from the inlet, discarding torsion leads to a reduction of the particles ejected within the 1st beat of -9.8% (= 76.9% - 67.1%) with a consequent increase of both the particles ejected during the 2nd beat (+7.2%) and residing in the LV after two beats (+2.5%) (see Table 5.1). Within two beats, 91.6% of the particles left the LV without torsion, while this becomes 94.1% when torsion is present. Looking at the velocity of the particles residing after 2 beats, 287 (out of 378) have a velocity lower than 0.5 m/s without torsion; with torsion, this applies to 250 (out of 264) particles.

5.3.2 Influence Of the Mitral Valve On Intraventricular Hemodynamics

At the E-peak (Figure 5.7), the MV increases the maximum velocity magnitude from 1.0 m/s to 2.0 m/s, and extends the areas with velocity beyond 1 m/s by 14%, 3.5%, 23.8% and 71.5% in the LA, SA1, SA2, SA3 planes, respectively. With the MV, the vortices originate at the tip of the MV leaflets instead of the annulus, resulting in enlarged vortices in the SA1 (the vorticity within 0-250 ss^{-1} and beyond 750 ss^{-1} increased by 5.3% and by 0.6%, respectively) and in the SA2 plane (the vorticity over 250 s^{-1} increased by 20.8%). The maximum WSS increases by 33 Pa and 11 Pa in the basal and medial sectors, respectively, whereas the average WSS increases by 5 Pa in the basal and medial posterior sectors.

At the A-peak (Figure 5.7), the MV increases the maximum velocity magnitude from 0.5 m/s to 0.8 m/s, and the areas with velocity beyond 0.25 m/s enlarge by 37.9%, 29.3%, 45.5%, 52% in the LA, SA1, SA2, SA3 planes, respectively. The MV slightly enhances the vorticity above 250 s^{-1} by 1.1%, 4.8%, 0.9%, in the LA, SA1, SA3 planes, respectively. The maximum WSS increases by 10-11 Pa in the posterior and posterior-lateral basal sectors, whereas the average WSS increases by 3 Pa in the posterior, posterior-lateral, and anterior-lateral sectors of the basal ring.

Focusing on the influence induced by the presence of the mitral valve leaflets in washing out the LV (Figure 5.6), we studied clearance of particles released from the apex for a simulation with and without valve (and with

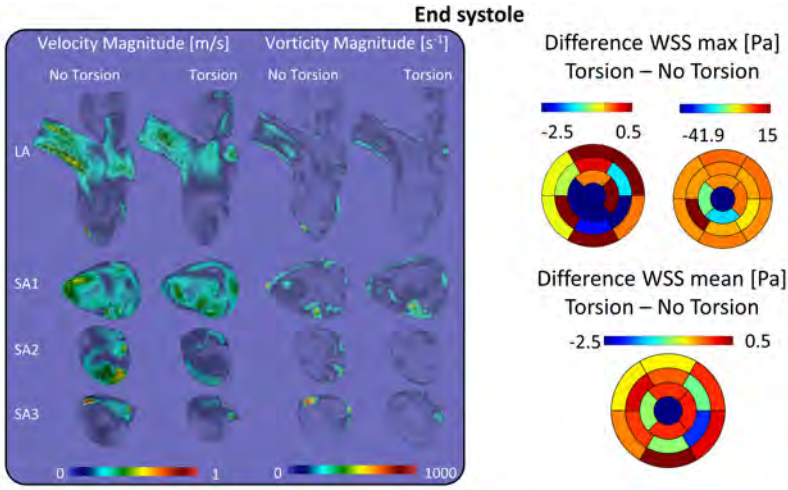

Residence Time of particles released from inlet

Particles percentage [%]	no Torsion	Torsion
Ejected 1° beat	67.1	76.9
Ejected 2° beat	24.5	17.3
Residing in the LV	8.4	5.9

Velocity distribution of particles residing in the LV after two beats

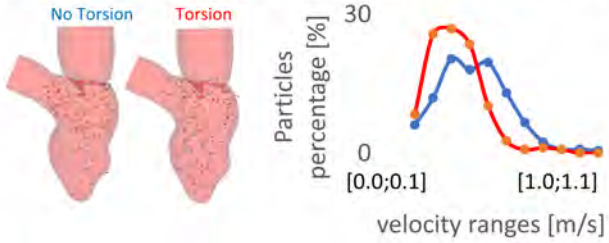

Figure 5.5: (Top) Velocity, vorticity, wall shear stress contours during end systole show a slight increase of these variables in the case disregarding torsion; (Middle) the percentage of particles ejected is higher in the Torsion case (+9.8%), nonetheless after two beats the difference decreases below 3%; (Bottom) the case without torsion induces a better motility of the particles residing in the left ventricle.

torsion applied to both cases). With the valve present, 67.9% and 21% of the particles released from the apical region are ejected during the 1^{st} and 2^{nd} beat, respectively, with the remaining 11.1% of the particles residing in the LV after two beats. In absence of the valve, 44% and 27.2% of the particles were ejected during the 1^{st} and 2^{nd} beat, respectively, with 28.4% residing in the LV.

Residence Time of particles released from apex

Particles percentage [%]	without valve	with valve
Ejected 1° beat	44.4%	67.9%
Ejected 2° beat	27.2%	21%
Residing in the LV	28.4%	11.1%

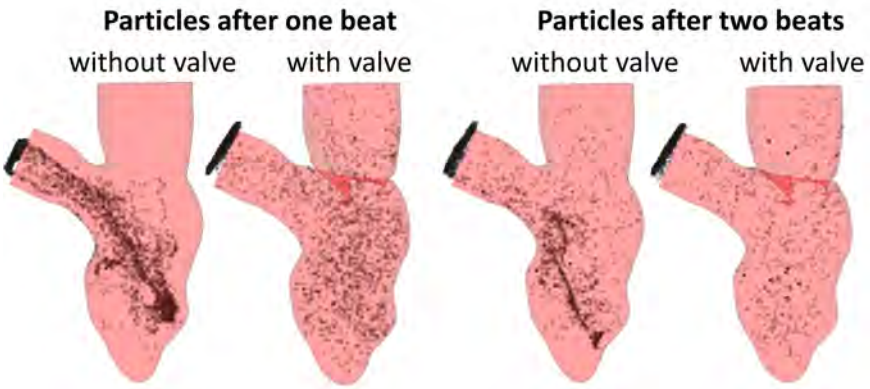

Figure 5.6: Residence time of the particles released from the apex show how the mitral valve enhances the apical wash-out.

5.4 Discussions

In this manuscript, we developed a Chimera-based patient-specific model of the LV coupled with a patient-inspired moving MV, and showcased the model to assess the impact of torsion and the presence of the mitral leaflets

on intraventricular hemodynamics. The open MV was segmented from cine-radial MRI images and leaflet motion was defined using a kinematic model. We tested the Chimera technique because it is particularly suited to combine the large motion of the LV endocardium with the impulsive kinematics of the MV leaflets. The Chimera technique allowed us to overcome the main limitations faced in previous work based on the ALE approach where CFD simulations in a deforming LV with mitral valve limited to one cardiac cycle [1], due to excessively distorted mesh resulting in negative volumes errors, or even to the diastolic phase [2].

Despite the obvious advantages of the Chimera technique over ALE for the given study case, we did experience unexpected technical difficulties while setting up the problem. Initially, the BL meshes of the MV leaflets were separated from the BL mesh of the LV (Figure 5.1C: separated LVMV): one anterior MV mesh; one posterior MV mesh; one LV mesh, whose generation is described in [42], [130]. With this mesh configuration, however, we experienced sudden vanishing of some component zones during the CFD calculation, regardless of several attempts involving the definition of customized cut-control, the BL thickness, the mesh densities, the temporal interpolation, and smooth connecting angles. This unforeseen dead zone error forced us to include the MV leaflets directly into the moving LV mesh resulting in limitations for the MV opening angles to preserve the mesh quality. Therefore, despite the claimed advantages of the Chimera technique in terms of handling mesh motion, the software version used in this study should be further optimized.

We experienced a significant and unexpected cycle-to-cycle variation even after six cardiac cycles, probably due to the high flow conditions induced by the large LV volume derived from the segmented geometries (SV = 109 mL) or the limited opening angle of the MV (around 25°) to preserve the mesh quality. Simulating multiple cardiac cycles is a good practice to get rid of the transitional effects, as confirmed by several studies: Long et al [97], Vasudevan et al [96], Seo et al [100], Mangual et al [122], Chnafa et al [59] simulated 4, 4, 5, 10, 35 cycles, respectively. Among these, it is worth noticing that only Chnafa et al [59] reported the cycle-to-cycle variations in the wall shear stress of the diastasis during the 20^{th} and 21^{st} cycles. In the referred case, five cycles were simulated to washout the initial conditions, and the results were reported based on phase-averaging over 30 additional cycles. In the other reported studies, even if multiple cycles were simulated, the analysis is often limited to the last cycle without reporting additional checks about the vanishing of the transient effects [96], [97], [100], [122]. More precise recommendations to objectively assess when a CFD calculation has reached a regime state may be helpful to the community. In this context, it is

worth remembering that the multi-laboratory study promoted by the Food and Drugs Administrations (FDA) to support the use of CFD simulations from a regulatory perspective is at a standstill [146], with CFD-use limited to the design stage and considered appropriate for evaluating relative design changes rather than assessing absolute quantities [147] (ISO 14708-5). We are aware that our simulations have not yet reached a regime state with cycle-to-cycle repeatability. At the same time, there is no guarantee that such solution would exist in high Reynolds number trans-mitral flows (peak Re in the order of 10.000) with a narrow high velocity jet in an expanding chamber. Nonetheless, it was especially the high computational cost (one cycle taking 24 hours on 2×Intel Xeon E5-2680v2 CPUs at 2.8 GHz) that restrained us from computing more cycles. Therefore, we simulated six cardiac cycles and reported the results of the 5^{th} (needed only for the EL and RT computation) and 6^{th} cardiac cycle.

Overall, we noticed only minor differences in velocity, wall shear stress, and vorticity contours in the simulations with and without torsion (Figures 5.4 and 5.5, and Tables 5.1 to 5.6). Interestingly, energy dissipation was found about 14% higher in the physiological torsion case compared to the simulation discarding torsion during the last two cardiac cycles. Nonetheless the impact of torsion on the energy loss is considered marginal being on the order of one thousand of the total cardiac energy (order of a few J) in both simulated cases. Vasudevan et al [96] recently investigated the effects of torsional motion on the LV in the fluid dynamics of five healthy human fetal and two healthy adult porcine hearts. The MV geometry was based on detailed anatomical measurements from a database of 10 adult porcine specimens [148] and the opening angles of the leaflets were derived from the three-chamber view of MRI data. Flow and energy dynamics were evaluated varying the torsional degree ($0^\circ, 5^\circ, 15^\circ$), with and without the mitral valve and the papillary muscles, and under a diseased condition. They found that the impact of ventricular torsion was minor and irrelevant on flow patterns, energy losses, ejection work, and wall shear stress, and the impact on the residence time was not evaluated. In our case, the effects of torsion on velocity, vorticity magnitude were negligible, whereas energy loss increased by 14% when considering torsion. It is hard to assess the physiological significance of this finding; as discussed further, torsion has a meaningful impact on the residence time and particle clearing from the left ventricle, of which the beneficial effects on reducing the risk of blood stasis and thrombus formation may outweigh the energy cost. Indeed, physiological torsion was found to have a favorable effect on removing particles from the LV at the first beat (+9.8%) that reduces up to 2% after two beats. On the other hand, the motility of the particles residing in the LV chamber was reduced by torsion.

To the best of our knowledge, there are no other studies that evaluated the particle residence time in function of the LV torsion, other than our previous study without the MV [42]. In that study, however, the mitral valve leaflets were not considered, and given the huge impact of the leaflets on intraventricular hemodynamics (see further), results should not be compared. Mangual et al [122] injected a virtual tracer inside the LV, of which about 80% is ejected within two beats in the healthy cases (mean ejection fraction and stroke volume equal to 55% and 74 mL, respectively), while this dropped to 20% in the cases with dilated cardiomyopathy (mean ejection fraction and stroke volume equal to 17.8% and 41 mL, respectively). Therefore, the flow after two beats is higher in our case (94.2%). A likely factor leading to this higher value are the high ejection fraction of 67% and stroke volume of 109 mL for this case. Also, the implementation of the MV into the LV mesh limited the opening angle of the valve (to preserve the mesh quality), which may have led to a more energetic incoming jet, generating more swirling flow and enhancing particle evacuation.

Beyond the study on the torsional effects, we also performed simulations (including torsion) without the MV, well known to have a dramatic impact on intraventricular hemodynamics. Starting from the contours of velocity, vorticity, and WSS, the presence of the mitral valve induced several effects, among which: (i) the formation of the vortical structures at the free edge of the valve instead of the annulus, resulting in a more central position of the vortices with respect to the long axis of the ventricle; (ii) an increased velocity peak of the inlet jet induced by the narrowing of the mitral orifice area; (iii) as a result of the combination of (i) and (ii), the jet and the vortical patterns better penetrate towards the apex, with enhanced local washout, as can be seen by the vorticity and wall shear stress (Figure 5.7).

Our findings about the influence of the valve in the flow field agree with the ones of Bavo et al [1] and Seo et al [71]. In our case, the apical washout was also assessed by releasing the particles in the apical region and computing their residence time with and without the mitral valve (Figure 5.6). In this regard, we found out that the valve enhances the direct flow (67.9% versus 44.4%) and the particles ejected in two beats (88.9% versus 71.6%). The presence of the valve also has an impact on the faith of particles released from the inlet. In previous work that did not include the mitral valve, physiological torsion decreased the direct flow and the particles ejected within two beats. Conversely, in the current study, torsion enhances the direct flow and the particles ejected within two beats increase. From a clinical perspective, we strongly believe that the residence time and the velocity distribution of the residing particles provide more significant insights to assess the predisposition to stasis rather than velocity, vorticity, or wall shear stress. Torsion does

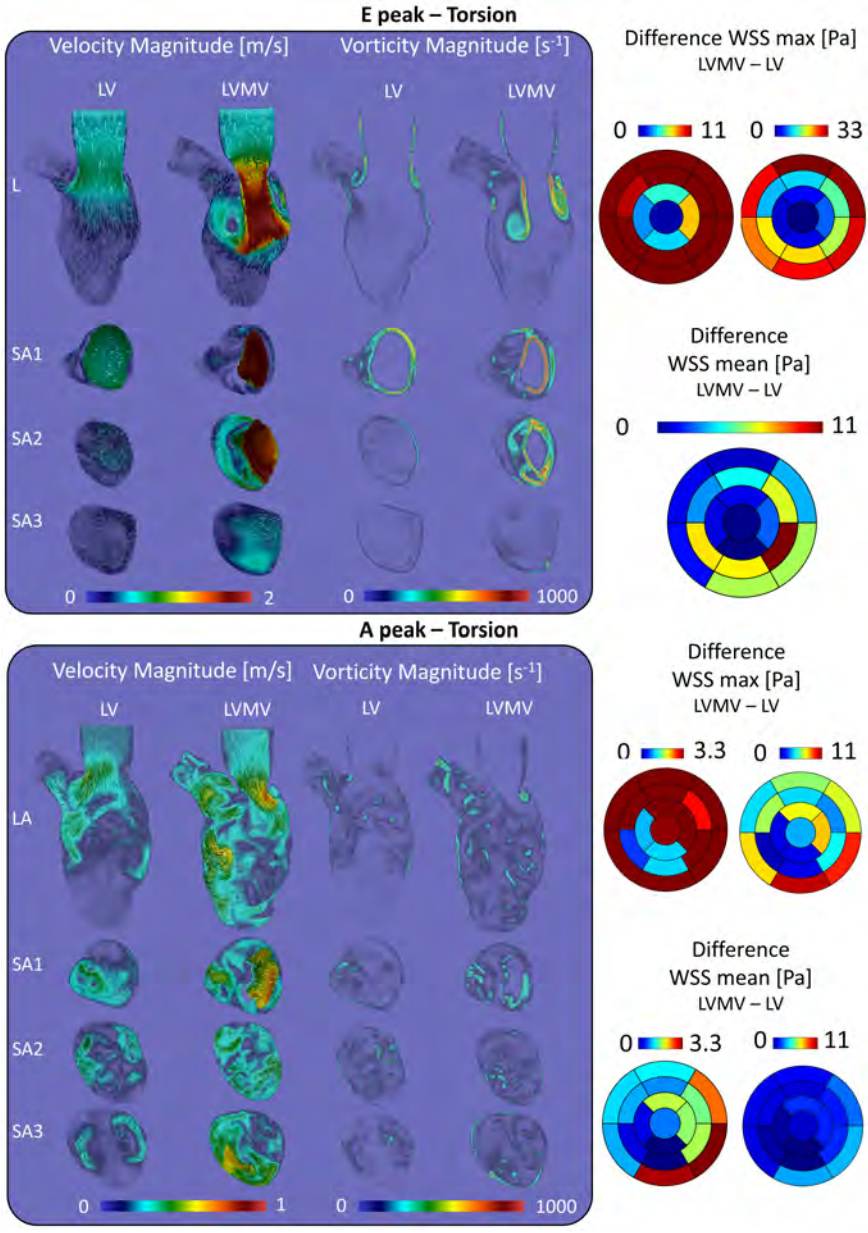

Figure 5.7: Impact of the mitral valve in the Torsion case on the velocity, vorticity and wall shear stress at A-peak and E-peak.

seem to have an impact on these parameters. It may therefore be safe to consider torsion in patient-specific CFD models, especially when these studies target stasis and residence time. In that context, future studies should also evaluate the impact of the Trabeculae Carneae. This will, however, require more advanced mesh handling methods that can cope with small cavities that compress and expand as the ventricle contracts and relaxes.

Our study has some important limitations. The patient-specific LV model resulted to have a stroke volume (109 mL) somewhat beyond the physiological range (55-100 mL), which induced a flow field (peak velocity = 2 m/s at the E-peak) more intense than a typical physiological case, that induces instabilities at the tip of the MV at the E-peak. We strongly believe that the 8 mm slice thickness of our cine-MRI short-axis imaging dataset considerably limited the accuracy of the segmentation of our patient-specific LV model. Therefore, the proposed workflow should be tested on imaging datasets with higher resolution. Moreover, also the assumption of a null or minimal reverse flow across the mitral valve during systole, due to the constant volume of the atrial chamber and the imposed boundary conditions, was affected by the enhanced flow conditions resulting in a reverse peak velocity of 0.4 m/s during systole. Furthermore, we could not overcome some important technical difficulties related to the Chimera technique, among which the imcompatibility with particular settings of the flow solver in Fluent 2019 R3 (e.g. a 2^{nd} order temporal discretization with mesh motion) and with particle tracking methods available in Fluent).

5.5 Conclusions

In this study, we presented a Chimera-based patient-specific model of the LV coupled with a patient-inspired kinematic model of the MV. We assessed the impact of torsion in the LV fluid dynamics by simulating multiple cardiac cycles with and without physiological torsion. Our results indicate that torsion has a minimal effect on velocity, vorticity, wall shear stress, and energy loss. With the implementation of the mitral valve, torsion enhanced both the direct flow and (minorly) the particles ejected within two beats, while it reduced the motility of the particles. The MV enhanced the propagation of the inlet jet, and promoted both the general and apical washout.

5.6 Acknowledgements

This work was supported by the European Commission within the Horizon 2020 Framework through the MSCA-ITN-ETN European Training Networks (project number 642458).

5.7 Supplementary material

5.7.1 Mesh generation

The Boundary Layer (BL) mesh of the MV is generated following these steps:

1. Two copies of the MV surface mesh (represented in cyan) were generated and translated, sliding along the LV endocardial mesh, so that the space encompassed between the two copies (shown with the dotted red line in Figure 5.1B.1) represents the MV, with a thickness of 2 mm. Subsequently, the lower edges of the copies are connected (shown with the yellow line, Figure 5.1B.1);

2. A collar mesh (shown with a black line in Figure 5.1B.2) overlapping with the LV endocardial surface mesh at the upper and lower part of the leaflets is created and fused with the surface leaflet meshes, generated in the previous step;

3. The resulting mesh is divided into the anterior and the posterior leaflets (shown in red and green, respectively, in Figure 5.1B.3), sharing six overlapping layers, with the following steps performed both for the anterior and posterior leaflets;

4. As preparation to build the three-blocks BL mesh for each leaflet, the surface mesh of this region is divided into three surfaces: the upper mesh, which is composed of the upper collar and upper leaflet grids (shown in orange, Figure 1B.4a, Figure 1B.4b), the free edge (shown in blue, Figure 5.1B.4a, Figure 5.1B.4b), the lower mesh (composed of the lower collar and lower leaflet, shown in magenta, Figure 1B.4a, Figure 1B.4b). Separately for the anterior and posterior leaflet (Figure 5.1B.4a, Figure 5.1B.4b), the upper and lower surface meshes are extruded with a thickness of 4 mm to build the first two blocks of each leaflet (shown in red and green, in Figure 5.1B.4a, Figure 5.1B.4b);

5. The third block is generated by extruding the surface shown in yellow (Figure 5.1B.5a, Figure 5.1B.5b), resulting from the fusion between the free edge surface and the contiguous surfaces created at step 5, towards the inner direction with a thickness of 4 mm (Figure 5.1B.6a, Figure 5.1B.6b).

The mesh separation between the anterior and posterior leaflet (step 3) is fundamental during valve closure because the Chimera technique allows the intersection between different component grids, but not self-intersection, which may become problematic during valve closure.

5.7.2 Additional tables

E-peak	vel $[m/s]$	[0.00, 0.25]	[0.25, 0.50]	[0.50, 0.75]	[0.75, 1.00]	[1.00, 1.25]	[1.25, 1.50]	[1.50, 1.75]	[1.75, 2.0]
LA	NoT	684.6	1022.9	888.3	192.2	90.3	72.5	114.0	185.6
	T	1055.3	705.8	850.3	182.3	91.0	71.4	131.9	162.3
SA1	NoT	493.7	363.7	5.2	0.0	0.0	0.0	173.7	123.0
	T	596.8	280.9	0.2	0.0	0.0	0.0	200.5	80.7
SA2	NoT	23.0	321.0	514.9	192.2	17.5	127.6	187.9	31.6
	T	7.7	357.6	579.3	134.5	8.5	60.2	217.7	50.2
SA3	NoT	148.0	1030.3	54.9	0.0	0.0	0.0	0.0	0.0
	T	188.0	889.6	155.7	0.0	0.0	0.0	0.0	0.0

Table 5.1: Contours extension $[mm^2]$ of velocity magnitude at E-peak, where *NoT* and *T* refer to the *No Torsion* and *Torsion* cases, respectively.

E-peak	vor $[s^{-1}]$	[0, 250]	[250, 500]	[500, 750]	[750, 1000]	[1000, 1250]	[1250, 1500]
LA	NoT	3103.8	113.6	31.8	0.2	0.0	0.0
	T	3117.7	114.3	17.2	0.0	1.1	0.0
SA1	NoT	1040.9	108.5	2.30	2.0	1.8	3.6
	T	1095.6	56.60	0.7	1.2	4.0	1.2
SA2	NoT	1067.2	295.9	49.8	2.8	0.0	0.0
	T	1117.0	228.0	70.1	0.7	0.0	0.0
SA3	NoT	1233.3	0.0	0.0	0.0	0.0	0.0
	T	1232.0	0.9	0.4	0.0	0.0	0.0

Table 5.2: Contours extension $[mm^2]$ of vorticity magnitude at E-peak, where *NoT* and *T* refer to the *No Torsion* and *Torsion* cases, respectively.

A-peak	velocity $[m/s]$	[0, 0.25]	[0.25, 0.5]	[0.50, 0.75]
LA	NoT	862.2	2238.5	149.6
	T	1349.1	1801.0	100.2
SA1	NoT	317.2	604.3	237.7
	T	409.6	532.7	216.9
SA2	NoT	461.4	949.0	5.5
	T	506.6	909.2	0.0
SA3	NoT	391.8	840.8	0.7
	T	495.1	638.3	99.9

Table 5.3: Contours extension $[mm^2]$ of velocity magnitude at A-peak, where *NoT* and *T* refer to the *No Torsion* and *Torsion* cases, respectively.

A-peak	vorticity $[s^{-1}]$	[0, 250]	[250, 500]	[500, 750]
LA	NoT	3176.3	73.9	0.2
	T	3206.1	44.2	0.0
SA1	NoT	1093.7	65.6	0.0
	T	1101.0	58.2	0.0
SA2	NoT	1045.1	10.7	0.0
	T	1411.7	4.0	0.0
SA3	NoT	1218.6	14.7	0.0
	T	1220.7	12.6	0.0

Table 5.4: Contours extension $[mm^2]$ of vorticity magnitude at A-peak, where *NoT* and *T* refer to the *No Torsion* and *Torsion* cases, respectively.

ES	velocity $[m/s]$	[0.00, 0.25]	[0.25, 0.50]	[0.50, 0.75]	[0.75, 1.00]	[1.00, 1.25]
LA	NoT	2071.8	764.6	12.9	0.0	0.0
	T	3074.9	0.0	0.0	0.0	0.0
SA1	NoT	485.8	580.0	13.8	0.0	0.0
	T	1295.2	0.0	0.0	0.0	0.0
SA2	NoT	623.8	258.6	20.2	0.0	0.0
	T	998.2	0.0	0.0	0.0	0.0
SA3	NoT	582.4	14.0	0.7	1.0	0.2
	T	640.1	0.0	0.0	0.0	0.0

Table 5.5: Contours extension $[mm^2]$ of velocity magnitude at end systole, where *NoT* and *T* refer to the *No Torsion* and *Torsion* cases, respectively.

ES	vorticity s^{-1}	[0, 250]	[250, 500]	[500, 750]	[750, 1000]
LA	NoT	2931.4	15.6	1.5	0.0
	T	3029.2	8.9	0.0	0.0
SA1	NoT	1111.6	50.0	2.7	0.0
	T	1147.1	63.6	1.0	0.0
SA2	NoT	955.4	14.3	0.0	0.0
	T	996.0	0.0	0.0	0.0
SA3	NoT	587.9	4.2	4.2	2.0
	T	627.8	2.5	0.0	0.0

Table 5.6: Contours extension $[mm^2]$ of vorticity magnitude at end systole, where *NoT* and *T* refer to the *No Torsion* and *Torsion* cases, respectively.

III

Conclusions

Chapters

Chapter 6

Conclusions

The developed workflow follows the typical steps to build a patient-specific CFD model, which are: segmentation from medical images, mesh generation, CFD setup and simulation, post-processing. This chapter begins with an overview of the workflow developed to overcome the challenges posed by the large and impulsive kinematics of the left ventricle endocardium and the mitral valve, respectively. Successively, this chapter provides the main CFD findings and achievements, followed by the limitations and the further developments, and concludes with the final remarks and potential applications.

6.1 Workflow

6.1.1 Segmentation and the semi-automatic meshing tool

The segmentation of the 4D LV configurations spanning one cardiac cycle was manually performed (gold standard) and provided the input – both as surfaces (from MRI, CT) or point clouds (from US) - to our meshing tool to build 4D structured grids. The semi-automatic meshing tool aimed to build 4D boundary layer grids with 1-to-1 vertex correspondence that could be used to assign the moving endocardial condition in a CFD simulation. The mapping tool relies on isoparametric transformations to project the desired meshed patches on the 4D segmented surfaces and allows to account for both the perpendicular (i.e dilation/contraction) and the tangential (i.e. torsion) motion components, with the latter that can be included with different degrees.

The 4D boundary layer meshes are built using a multi-block approach, which consists of the LV sac, the Y-junction (i.e. the inlet and the outlet parts), and the connecting part. The accuracy can be tuned by varying the number of control points to project onto the segmented surfaces, whereas the number of mesh elements can be increased ex-post via a fast operation that furtherly subdivides the 4D meshes. In case of the MRI short-axis dataset used to build the patient-specific CFD model of the LV, the accuracy of the meshing tool was assessed by evaluating the volume difference percentage between the generated 4D meshes and the segmented ones, which on average was less than 2%.

6.1.2 CFD setup: the Chimera technique

We based our CFD model on the Chimera (or overset meshes) technique to overcome the excessive distortion of the LV mesh experienced by Bavo et al., within our research group, using the Arbitrary-Lagrangian Eulerian (ALE) approach. The Chimera technique is suited for problems involving large and relative motion because it allows modeling the moving fluid domain via one or several overlapping boundary layer component grids embedded in a Cartesian grid. Furthermore, the boundary layer meshes guarantee a fine evaluation of the wall shear stress, which may be relevant to accurately assess when investigating problems that relate to the blood-endothelial interface such as the predisposition to thrombus formation. To the best of our knowledge, only Al-Azawy et al. [131] relied on the Chimera technique to investigate the hemodynamics in a cardiac application, a pulsatile left ventricular assist device. The overset mesh approach was adopted in the referred study to handle the motion of the pusher plate and the valve to gain more insight into the wall shear stress and strain rate near the valves. Moreover, Al-Azawy et al. [131] used the Chimera technique to handle the separation of the fluid domain induced by the valve closure.

6.2 CFD findings

Both the new meshing tool and the Chimera technique allowed us to simulate multiple cardiac cycles in a patient-specific LV model with different degrees of torsion, with and without the mitral valve.

6.2.1 Cycle-to-cycle variation

Simulating multiple cardiac cycles allowed us to notice cycle-to-cycle variability, mentioned also by Chnafa [59], and the wash-out inside the LV chamber by computing the residence time of particles injected into the LV. Chnafa et al. found minor cycle-to-cycle variation also after 35 cycles, suggesting that these variations are not only induced by the transitional effects to accelerate the

flow at the start of the CFD simulation but that they are rather a consequence of the transitional-to-turbulent flow state that occurs inside the LV chamber. Therefore, these fluctuations would not vanish by simulating more cycles and the variance of the computed flow quantities should be monitored to determine when to end a simulation. In this regard, the use of several component grids allow the Chimera technique to easily refine the inner fluid region of the LV where the vortex ring forms rather than at the endocardium, resulting in fewer meshing constraints in comparison with other approaches. This application could provide undiscovered 3D flow details in terms of temporal and spatial resolution, otherwise not achievable using the typical cardiac flow imaging techniques, whether in vivo (4D flow MRI) or in vitro (Particle Imaging Velocimetry). In our simulated cases, the cycle-to-cycle variation after six cycles was minor without the mitral valve (MV), whereas it was still prominent with the MV, enhanced by the turbulent flow regime (Re = 10.000) at the E_{peak}.

6.2.2 Impact of torsion and MV on the LV fluid dynamics

In the CFD model without the MV, torsion had no impact on velocity, vorticity, WSS, and energy loss, impaired the direct flow (i.e. particles ejected within the first beat) while maintaining better motility of the particles residing in the LV after two cycles for supraphysiological values.

Interestingly, with the implementation of the MV, torsion slightly affected velocity, vorticity, WSS, and energy loss. Even though torsion increased the energy loss by 7% during one cardiac cycle, the impact is considered marginal because it is only one thousand of the total cardiac energy. In addition, although we mainly focus on relative differences between the different simulations, the incompatibility of the used Ansys Fluent version with overset meshing and limitation to the use of a first order discretization scheme adds uncertainty to the derived absolute values of energy losses. Torsion increased the direct flow by 14% and 9.8%, respectively, whereas it impaired the motility of the particles residing in the LV after two beats, showing that the MV has a paramount effect on the LV fluid dynamics and it should be included in CFD models that aim to assess ventricular residence time. Vasudevan et al. [96] investigated the effects of torsion on the porcine LV fluid dynamics without finding relevant differences induced by torsion, however, without evaluating the residence time. Among other testing conditions, Vasudevan et al. [96] evaluated whether including the MV impacted the ventricular flow field with different degrees of torsion. The MV geometry was based on detailed anatomical measurements from a database of 10 adult porcine specimens [148] and the motion was derived from measurements of the opening angles [149]. In their case, including or not the MV did not induce different considerations about the effects of torsion on the intraventricular flow. Given our

different conclusions about the impact of torsion on the residence time with and without the mitral valve, we strongly believe that a CFD modeling of the LV that aims to assess the intraventricular flow should not disregard the MV. In the comparison between the physiological torsion case with and without the valve, we found that the MV enhances the propagation of the vortex ring towards the apex with the MV and the apical washout. This is in agreement with the findings of Bavo et al. [2] and Seo et al [71]. However, our CFD findings have to be considered cautiously due to the lack of phase-averaging data that might affect the patterns of our contours.

6.3 Limitations and further developments

The run-time of the meshing algorithm, which includes the multi-block approach and the temporal interpolation tool, is within 10-15 minutes if applied to a 4D segmented dataset with 30 configurations spanning one cardiac cycle. Nonetheless, at the current stage, also the time needed to segment a 4D imaging dataset should be taken into account. Under the assumption that the manual segmentation of one time-instant requires 10-15 minutes, the segmentation of the 4D dataset (composed of 30 time-instant configurations) could easily take 5-8 hours. Therefore, the projection of the control points directly based on the grey-scale levels of the medical images would considerably improve the time performance of the workflow, with the current mapping algorithm that could be used for both the segmentation and meshing. In our opinion, this represents the first development that could open the way of our workflow towards the clinical routine use. Conti et al. [54] developed a semi-automatic tool to detect the LV contours based on region-based image noise distribution (for endocardial detection) and edge-based image gradient (for LV epicardial detection), however, it provides an open moving mesh of the LV sac which disregards the Y-junction. As further developments of our meshing tool, the manual interaction still needed in some steps (the choice of the scaling factors for the mapping of the LV chamber, the selection of two points to build the Y-junction mesh, and the renumbering of the border nodes needed to connect the LV sac mesh and the Y-junction mesh) could be completely removed and some constraints based on the local morphology (e.g. curvature) could be added to allow a more faithful tracking of the material points. This would also lead to a more advanced model of ventricular torsion, which in this work was superimposed as a global uniform rotation onto the 4D meshes of the LV sac due to the inability to reliably detect torsional motion from the available CT and MRI scans. In this regard, shape-recognition methods based on deep learning methodologies are promising to automatically segment several cardiac structures (atria, ventricles, valves) and could lead to fully patient-specific cardiac models [150]. Recently,

Kong et al. [151] broke through this barrier by developing a fully automatic workflow to build CFD cardiac meshes starting from medical images based on 2D convolutional neural networks (for MR and CT images).

We experienced some technical difficulties which could be valuable further developments for the Chimera technique implemented in Fluent software. The first attempt to model the MV as two separate component (anterior and posterior) grids on top of the moving patient-specific LV grid and the Cartesian one resulted in an unforeseen dead zone error, even with enabling the cut-control. In this circumstance, we were forced to implement the anterior and the posterior MV valve grids directly into the LV mesh resulting in limitations of the MV opening angles to preserve the mesh quality. Therefore, some developments are still missing in the Chimera technique implemented in Fluent 2019 R3 to reach a relevant maturity and robustness, the flow solver is still incompatible with several settings, a.o. the 2^{nd} order temporal discretization with dynamic mesh motion, and with particle tracking methods available in Fluent. The compatibility with the 2^{nd} order temporal discretization would improve the accuracy of the CFD simulation, whereas the availability of the particles tracking method in Fluent would avoid the use of additional software in the post-processing. Furthermore, comparing the Chimera and the ALE technique on the same case study would allow to evaluate the accuracy in the computation of the flow variables (such as the WSS), and whether the improved robustness depends on the Chimera technique or solely on the meshing tool. The general validation of the Chimera technique against the ALE approach has been successfully performed in a CFD study about air-jet weaving looms by Delcour et al. [152], making it promising also for cardiac patient-specific modeling.

Furthermore, our MV model is not patient-specific but patient-inspired: the leaflets were segmented at the diastolic A-peak from a cine-radial MRI dataset, and the rotational angles defining the kinematics were adapted from literature [101]. We could not derive a patient-specific model of the MV from our cine-radial MRI dataset because the spatial resolution was not fine enough to accurately retrieve the whole impulsive motion of the leaflets.

Our patient-inspired MV model and our patient-specific LV model with stroke volume slightly beyond the physiological range pose other steps to be performed before proceeding with the validation of the model. The developed workflow should be applied to imaging datasets with a more refined slice thickness (1 mm) so that a more accurate patient-specific model then could be validated in vivo or in vitro, with a 4D flow MRI dataset or a PIV investigation of a transparent replica, respectively, even though the phase averaging would not allow to capture the cycle-to-cycle variations. In this regard, the phase-averaging of more simulated cardiac cycles represents a further development

of the current computational study. Furthermore, the use of an imaging technique with finer spatial resolution would also allow the implementation of the trabeculae carnae, which were found to have an impact on the LV fluid dynamics, and the left atrium, which was partially modeled as a stationary wall.

A patient-specific model of the MV takes into account the real kinematics, however, the temporal resolution of the available medical imaging modalities would still not be adequate to detect the high-frequency fluctuations of the leaflets, which might have an impact on the LV fluid dynamics. The fluttering of the leaflets, however, could have been computed if using a Fluid-Structure Interaction (FSI) model of the MV. However, FSI approaches require an increased computational time and a not trivial definition of the structural properties of the MV biological tissue.

6.4 Final remarks and potential applications

The proposed workflow allowed us to solve the excessive mesh distortion occurring in Bavo's model resulting in CFD simulations that encompass multiple cycles, thanks to the developed meshing tool and the CFD model based on the Chimera technique.

The current meshing tool could be applied to similar structures composed of a chamber, an inlet, and an outlet, that physiologically or pathologically undergo large deformations such as the right ventricle, the stomach, the bladder, and the gallbladder.

The finer spatial and temporal resolution of our CFD model, in comparison with the available clinical imaging modalities, allowed us to compute the energy loss and the residence time, which can become relevant in clinics to evaluate the flow energetics and the predisposition to stasis and thrombus formation inside the LV. This represents a current and a long-run advantage of CFD modeling in comparison with the 4D flow MRI as the spatial and temporal resolution of the latter is not expected to improve quickly enough to fill the gap in the upcoming years.

Within this research, we used our workflow to verify whether a patient-specific CFD model could be used to detect the onset of an altered torsion as a precursor of a pathological condition. However, this is intended only as a study case of our workflow, because the multi-scale level of pathologies requires a more accurate evaluation of the mechanisms that typically involve an electromechanical model. The patient-specific CFD modeling of the LV can be potentially used in clinics for the early detection of pathologies, to compare Pre-Post clinical data, and to predict the outcome of surgical procedures. The evaluation of Pre-Post clinical data regarding ventriculoplasty

could be assessed with the current workflow, whereas the mitral valvuloplasty (a.o. mitraclip, chordae replacement) would require further developments towards FSI modeling.

This workflow could be used or easily adapted also in other biomedical applications that involve components with large and impulsive kinematics, a.o. the CFD modeling of a right ventricle, a ventricular assist device, a blood centrifugal impeller, and similar non-biomedical applications.

Bibliography

[1] A. M. Bavo, A. M. Pouch, J. Degroote, J. Vierendeels, J. H. Gorman, R. C. Gorman and P. Segers, 'Patient-specific CFD simulation of intraventricular haemodynamics based on 3D ultrasound imaging', *BioMedical Engineering OnLine*, vol. 15, no. 1, p. 107, 2016.

[2] ——, 'Patient-specific CFD models for intraventricular flow analysis from 3D ultrasound imaging: Comparison of three clinical cases', *Journal of Biomechanics*, vol. 50, pp. 144–150, 2017.

[3] World Health Organization, 'World Health Organization cardiovascular disease risk charts: revised models to estimate risk in 21 global regions', *The Lancet Global Health*, vol. 7, no. 10, e1332–e1345, 2019.

[4] A. A. Pugovkin, A. G. Markov, S. V. Selishchev, L. Korn, M. Walter, S. Leonhardt, L. A. Bockeria, O. L. Bockeria and D. V. Telyshev, 'Advances in Hemodynamic Analysis in Cardiovascular Diseases Investigation of Energetic Characteristics of Adult and Pediatric Sputnik Left Ventricular Assist Devices during Mock Circulation Support', *Cardiology Research and Practice*, vol. 2019, 2019.

[5] D. Bluestein, 'Utilizing Computational Fluid Dynamics in Cardiovascular Engineering and Medicine—What You Need to Know. Its Translation to the Clinic/Bedside', *Physiology & behavior*, vol. 176, no. 3, pp. 139–148, 2017.

[6] C. A. Taylor, T. A. Fonte, J. K. Min, R. City and L. Angeles, 'Computational Fluid Dynamics Applied to Cardiac Computed Tomography for Noninvasive Quantification of Fractional Flow Reserve Scientific Basis', *Journal of the American College of Cardiology*, vol. 61, no. 22, 2013.

[7] P. De Jaegere, G. De Santis, R. Rodriguez-Olivares, J. Bosmans, N. Bruining, T. Dezutter, Z. Rahhab, N. El Faquir, V. Collas, B. Bosmans, B. Verhegghe, C. Ren, M. Geleinse, C. Schultz, N. Van Mieghem, M. De Beule and P. Mortier, 'Patient-Specific Computer Modeling to Predict Aortic Regurgitation after Transcatheter Aortic Valve Replacement', *JACC: Cardiovascular Interventions*, vol. 9, no. 5, pp. 508–512, 2016.

[8] E. Marieb and K. Hoehn, 'Human anatomy and Physiology 9th Edition'. 2013, pp. 692–698.

[9] Guyton and Hall, 'Textbook of Medical Physiology', 11th Editi, Elsevier Inc., Ed. 2006.

[10] D. Sánchez-Quintana, J. R. López-Mínguez, Y. Macías, J. A. Cabrera and F. Saremi, 'Left atrial anatomy relevant to catheter ablation', *Cardiology Research and Practice*, vol. 2014, 2014.

[11] R. Markham, S. Kyranis, N. Aroney, K. Lau, K. Poon, G. Scalia and D. Walters, 'Transcatheter mitral valve intervention: an emerging treatment for mitral regurgitation', *Internal Medicine Journal*, vol. 48, no. 4, pp. 382–390, 2018.

[12] A. D. Kaiser, D. M. McQueen and C. S. Peskin, 'Modeling the mitral valve', *International Journal for Numerical Methods in Biomedical Engineering*, vol. 35, no. 11, e3240, 2019.

[13] S. M. Adhyapak and V. R. Parachuri, 'Architecture of the left ventricle: insights for optimal surgical ventricular restoration.' eng, *Heart failure reviews*, vol. 15, no. 1, pp. 73–83, 2010.

[14] S. Y. Ho, 'Structure and anatomy of the aortic root', *European Journal of Echocardiography*, vol. 10, no. 1, pp. 3–10, 2009.

[15] L. J. Spreeuwers, S. J. Bangma, R. J. Meerwaldt, E. J. Vonken and M. Breeuwer, 'Detection of trabeculae and papillary muscles in cardiac MR images', *Computers in Cardiology*, vol. 32, pp. 415–418, 2005.

[16] K. Hanneman, F. P. Chan, R. Scott Mitchell, D. Craig Miller and D. Fleischmann, 'Pre- and postoperative imaging of the aortic root', *Radiographics*, vol. 36, no. 1, pp. 19–37, 2016.

[17] M. Loukas, A. Sharma, C. Blaak, E. Sorenson and A. Mian, 'The clinical anatomy of the coronary arteries', *Journal of Cardiovascular Translational Research*, vol. 6, no. 2, pp. 197–207, 2013.

[18] F. A. Gómez and L. E. Ballesteros, 'Evaluation of coronary dominance in pigs; a comparative study with findings in human hearts', *Arquivo Brasileiro de Medicina Veterinaria e Zootecnia*, vol. 67, no. 3, pp. 783–789, 2015.

[19] J. Pocock and C. Richards, 'Human physiology: the basis of medicine', O. U. Press, Ed., 10. Oxford: Oxford University Press, 2006, vol. 40, pp. 880–880.

[20] H. Saaid, 'Multimodality Analyses of 3D Flow in a Phantom Model of the Left Ventricle', March. 2019, p. 175.

[21] G. Pedrizzetti and F. Domenichini, 'Nature optimizes the swirling flow in the human left ventricle.' eng, *Physical review letters*, vol. 95, no. 10, p. 108 101, 2005.

[22] P. J. Kilner, G. Z. Yang, A. J. Wilkes, R. H. Mohiaddin, D. N. Firmin and M. H. Yacoub, 'Asymmetric redirection of flow through the heart.' eng, *Nature*, vol. 404, no. 6779, pp. 759–761, 2000.

[23] M. Gharib, E. Rambod, A. Kheradvar, D. J. Sahn and J. O. Dabiri, 'Optimal vortex formation as an index of cardiac health.' *Proceedings of the National Academy of Sciences of the United States of America*, vol. 103, no. 16, pp. 6305–6308, 2006.

[24] J. O. Dabiri, 'Optimal vortex formation as a unifying principle in biological propulsion', *Annual Review of Fluid Mechanics*, vol. 41, pp. 17–33, 2009.

[25] J. Bermejo, P. Martínez-Legazpi and J. C. del Álamo, 'The Clinical Assessment of Intraventricular Flows', *Annual Review of Fluid Mechanics*, vol. 47, no. 1, 2015.

[26] M. Cikes and S. D. Solomon, 'Beyond ejection fraction: An integrative approach for assessment of cardiac structure and function in heart failure', *European Heart Journal*, vol. 37, no. 21, pp. 1642–1650, 2016.

[27] H. B. Nguyen, D. P. Banta, G. Stewart, T. Kim, R. Bansal, J. Anholm, W. A. Wittlake and S. W. Corbett, 'Cardiac index measurements by transcutaneous doppler ultrasound and transthoracic echocardiography in adult and pediatric emergency patients', *Journal of Clinical Monitoring and Computing*, vol. 24, no. 3, pp. 237–247, 2010.

[28] A. Evangelista, D. Garcia-Dorado, H. G. Del Castillo, T. Gonzalez-Alujas and J. Soler-Soler, 'Cardiac index quantification by Doppler ultrasound in patients without left ventricular outflow tract abnormalities', *Journal of the American College of Cardiology*, vol. 25, no. 3, pp. 710–716, 1995.

[29] N. E. Haites, F. M. McLennan, D. H. Mowat and J. M. Rawles, 'Assessment of cardiac output by the Doppler ultrasound technique alone', *British Heart Journal*, vol. 53, no. 2, pp. 123–129, 1985.

[30] A. Schmidt, O. C. Almeida F, A. Pazin F, J. A. Marin-Neto and B. C. Maciel, 'Valvular regurgitation by color Doppler echocardiography', *Arquivos Brasileiros de Cardiologia*, vol. 74, no. 3, pp. 273–281, 2000.

[31] J. Jeong and F. Hussain, 'On the identification of a vortex', *Journal of Fluid Mechanics*, vol. 285, no. February 2015, pp. 69–94, 1995.

[32] B. Su, R. S. Tan, J. L. Tan, K. W. Q. Guo, J. M. Zhang, S. Leng, X. Zhao, J. C. Allen and L. Zhong, 'Cardiac MRI based numerical modeling of left ventricular fluid dynamics with mitral valve incorporated', *Journal of Biomechanics*, vol. 49, no. 7, pp. 1199–1205, 2016.

[33] E. E. Calkoen, M. S. Elbaz, J. J. Westenberg, L. J. Kroft, M. G. Hazekamp, A. A. Roest and R. J. Van Der Geest, 'Altered left ventricular vortex ring formation by 4-dimensional flow magnetic resonance imaging after repair of atrioventricular septal defects', *Journal of Thoracic and Cardiovascular Surgery*, vol. 150, no. 5, 1233–1240.e1, 2015.

[34] G. Pedrizzetti, F. Domenichini and G. Tonti, 'On the Left Ventricular Vortex Reversal after Mitral Valve Replacement', *Annals of Biomedical Engineering*, vol. 38, no. 3, pp. 769–773, 2010.

[35] J. Hunt, A. A. Wray and P. Moin, 'Eddies , streams , and convergence zones in turbulent flows', *Center for Turbulence Research Proceedings of the Summer Program*, no. November 1988, 1988.

[36] Q. Chen and Q. Zhong, 'Comparison of vortex identification criteria for planar velocity fields', *Physics of Fluids*, no. September, 2015.

[37] C.-M. Li, W.-J. Bai, Y.-T. Liu, H. Tang and L. Rao, 'Dissipative energy loss within the left ventricle detected by vector flow mapping in diabetic patients with controlled and uncontrolled blood glucose levels', *The international journal of cardiovascular imaging*, vol. 33, no. 8, pp. 1151–1158, 2017.

[38] Y. Cao, X.-Y. Sun, M. Zhong, L. Li, M. Zhang, M.-J. Lin, Y.-K. Zhang, G.-H. Jiang, W. Zhang and Y.-Y. Shang, 'Evaluation of hemodynamics in patients with hypertrophic cardiomyopathy by vector flow mapping: Comparison with healthy subjects', *Experimental and Therapeutic Medicine*, pp. 4379–4388, 2019.

[39] S. Yoshida, S. Miyagawa, S. Fukushima, Y. Yoshikawa, H. Hata, S. Saito, D. Yoshioka, S. Kainuma, K. Domae, R. Matsuura, S. Nakatani, K. Toda and Y. Sawa, 'Cardiac function and type of mitral valve surgery affect postoperative blood flow pattern in the left ventricle', *Circulation Journal*, vol. 83, no. 1, pp. 130–138, 2019.

[40] K. Nakashima, K. Itatani, T. Kitamura, N. Oka, T. Horai, S. Miyazaki, M. Nie and K. Miyaji, 'Energy dynamics of the intraventricular vortex after mitral valve surgery', *Heart and Vessels*, vol. 32, no. 9, pp. 1123–1129, 2017.

[41] L. E. Jacobs, M. N. Kotler and W. R. Parry, 'Flow Patterns in Dilated Cardiomyopathy: A Pulsed-wave and Color Flow Doppler Study', *Journal of the American Society of Echocardiography*, vol. 3, no. 4, pp. 294–302, 1990.

[42] F. Canè, M. Selmi, G. De Santis, A. Redaelli, P. Segers and J. Degroote, 'Mixed impact of torsion on LV hemodynamics: A CFD study based on the Chimera technique', *Computers in Biology and Medicine*, vol. 112, no. July, p. 103 363, 2019.

[43] G. Pedrizzetti, G. La Canna, O. Alfieri and G. Tonti, 'The vortex - An early predictor of cardiovascular outcome?', *Nature Reviews Cardiology*, vol. 11, no. 9, pp. 545–553, 2014.

[44] J. N. Cohn, R. Ferrari and N. Sharpe, 'Cardiac remodeling-concepts and clinical implications: A consensus paper from an International Forum on Cardiac Remodeling', *Journal of the American College of Cardiology*, vol. 35, no. 3, pp. 569–582, 2000.

[45] E. Kinova, N. Spasova, A. Borizanova and A. Goudev, *Torsion Mechanics as an Indicator of More Advanced Left Ventricular Systolic Dysfunction in Secondary Mitral Regurgitation in Patients with Dilated Cardiomyopathy: A 2D Speckle-Tracking Analysis*, 2018.

[46] V. M. Stoll, A. T. Hess, C. T. Rodgers, M. M. Bissell, P. Dyverfeldt, T. Ebbers, S. G. Myerson, C. J. Carlhäll and S. Neubauer, 'Left ventricular flow analysis novel imaging biomarkers and predictors of exercise capacity in heart failure', *Circulation: Cardiovascular Imaging*, vol. 12, no. 5, pp. 1–12, 2019.

[47] I. K. Rüssel, W. P. Brouwer, T. Germans, P. Knaapen, J. T. Marcus, J. Van Der Velden, M. J. Götte and A. C. Van Rossum, 'Increased left ventricular torsion in hypertrophic cardiomyopathy mutation carriers with normal wall thickness', *Journal of Cardiovascular Magnetic Resonance*, vol. 13, no. 1, p. 3, 2011.

[48] B. J. Maron, 'Hypertrophic cardiomyopathy: a systematic review.' eng, *JAMA*, vol. 287, no. 10, pp. 1308–1320, 2002.

[49] B. Iung and A. Vahanian, 'Epidemiology of acquired valvular heart disease', *Canadian Journal of Cardiology*, vol. 30, no. 9, pp. 962–970, 2014.

[50] G. Pacileo, L. Baldini, G. Limongelli, G. Di Salvo, M. Iacomino, C. Capogrosso, A. Rea, A. D'Andrea, M. G. Russo and R. Calabrò, 'Prolonged left ventricular twist in cardiomyopathies: A potential link between systolic and diastolic dysfunction', *European Journal of Echocardiography*, vol. 12, no. 11, pp. 841–849, 2011.

[51] S. Nakatani, 'Left ventricular rotation and twist: why should we learn?', eng, *Journal of cardiovascular ultrasound*, vol. 19, no. 1, pp. 1–6, 2011.

[52] I. Y. Tan, A. M. Demchuk, J. Hopyan, L. Zhang, D. Gladstone, K. Wong, M. Martin, S. P. Symons, A. J. Fox and R. I. Aviv, 'CT angiography clot burden score and collateral score: Correlation with clinical and radiologic outcomes in acute middle cerebral artery infarct', *American Journal of Neuroradiology*, vol. 30, no. 3, pp. 525–531, 2009.

[53] M. H. Bahreini Toosi, H. Zarghani, H. Poorzand, S. Na-Seri, A. Eshraghi and A. Golabpour, 'Sex-related left ventricle rotational and torsional mechanics by block matching algorithm', *Journal of Biomedical Physics and Engineering*, vol. 9, no. 5, pp. 541–550, 2019.

[54] C. A. Conti, E. Votta, C. Corsi, D. D. Marchi and G. Tarroni, 'Left ventricular modelling : a quantitative functional assessment tool based on cardiac magnetic resonance imaging', *Interface Focus*, vol. 1, no. March, pp. 384–395, 2011.

[55] Z. Arab-Baferani, M. Mokhtari-Dizaji and F. Roshanali, 'Extraction of left-ventricular torsion angle from the long-axis view by block-matching algorithm: Comparison with the short-axis view', *Ultrasonics*, vol. 53, no. 2, pp. 552–560, 2013.

[56] F. Domenichini, G. Pedrizzetti and B. Baccani, 'Three-dimensional filling flow into a model left ventricle', *Journal of Fluid Mechanics*, vol. 539, no. -1, p. 179, 2005.

[57] C. Chnafa, S. Mendez and F. Nicoud, 'Image-based large-eddy simulation in a realistic left heart', *Computers and Fluids*, vol. 94, pp. 173–187, 2014.

[58] C. Chnafa, S. Mendez, R. Moreno and F. Nicoud, 'Using image-based CFD to investigate the intracardiac turbulence', *Modeling, Simulation and Applications*, vol. 14, no. November, pp. 113–117, 2015.

[59] C. Chnafa, S. Mendez and F. Nicoud, 'Image-Based Simulations Show Important Flow Fluctuations in a Normal Left Ventricle : What Could be the Implications ?', *Annals of Biomedical Engineering*, vol. 44, no. 11, pp. 3346–3358, 2016.

[60] M. Germano, U. Piomelli, P. Moin and W. H. Cabot, 'A dynamic subgrid-scale eddy viscosity model with a global model coefficient', *Physics of Fluids*, vol. 18, no. 12, p. 125 109, 2006.

[61] V. Michelassi, J. Wissink and W. Rodi, 'Analysis of DNS and LES of Flow in a Low Pressure Turbine Cascade with Incoming Wakes and Comparison with Experiments', *Flow, Turbulence and Combustion*, vol. 69, no. 3-4, pp. 295–329, 2002.

[62] A. Monokrousos, L. Brandt, P. Schlatter and D. S. Henningson, 'DNS and LES of estimation and control of transition in boundary layers subject to free-stream turbulence', *International Journal of Heat and Fluid Flow*, vol. 29, no. 3, pp. 841–855, 2008.

[63] S. Hickel and N. A. Adams, 'Implicit LES applied to zero-pressure-gradient and adverse-pressure-gradient boundary-layer turbulence', *International Journal of Heat and Fluid Flow*, vol. 29, no. 3, pp. 626–639, 2008.

[64] S. B. Pope, 'A perspective on turbulence modeling', *Kluwer Acodemic Publishers*, pp. 53–54, 1999.

[65] J. Degroote, 'Partitioned Simulation of Fluid-Structure Interaction: Coupling Black-Box Solvers with Quasi-Newton Techniques', *Archives of Computational Methods in Engineering*, vol. 20, no. 3, pp. 185–238, 2013.

[66] C. S. Peskin, 'Flow Patterns Around Heart Valves: A Numerical Method', *Journal of Computation*, vol. 10, pp. 252–271, 1972.

[67] R. Mittal, J. H. Seo, V. Vedula, Y. J. Choi, H. Liu, H. H. Huang and S. Jain, 'Computational Modeling of Cardiac Hemodynamics : Current Status and Future Outlook', *Journal of Computational Physics*, vol. 305, pp. 1065–1082, 2016.

[68] G. Houzeaux, B. Eguzkitza, R. Aubry, H. Owen and M. Vázquez, 'A Chimera method for the incompressible Navier-Stokes equations', *International Journal for Numerical Methods in Fluids*, vol. 75, no. 3, pp. 155–183, 2014.

[69] M. Behr and T. Tezduyar, 'The Shear-Slip Mesh Update Method', *Computer Methods in Applied Mechanics and Engineering*, vol. 174, no. 3-4, pp. 261–274, 1999.

[70] G. Houzeaux and R. Codina, 'A Chimera method based on a Dirichlet/Neumann(Robin) coupling for the Navier-Stokes equations', *Computer Methods in Applied Mechanics and Engineering*, vol. 192, pp. 3343–3377, 2003.

[71] J. H. Seo, V. Vedula, T. Abraham, A. C. Lardo, F. Dawoud, H. Luo and R. Mittal, 'Effect of the mitral valve on diastolic flow patterns', *Physics of Fluids*, vol. 26, no. 12, 2014.

[72] K. B. Chandran, 'Role of Computational Simulations in Heart Valve Dynamics and Design of Valvular Prostheses', *Cardiovasc Eng Technololgy*, vol. 1, no. 1, pp. 18–38, 2010.

[73] S. K. Kadhim, M. S. Nasif, H. H. Al-Kayiem and R. Al-Waked, 'Computational fluid dynamics simulation of blood flow profile and shear stresses in bileaflet mechanical heart valve by using monolithic approach', *Simulation*, vol. 94, no. 2, pp. 93–104, 2018.

[74] V. Vedula, J. H. Seo, A. C. Lardo and R. Mittal, 'Effect of trabeculae and papillary muscles on the hemodynamics of the left ventricle', *Theoretical and Computational Fluid Dynamics*, vol. 30, pp. 3–21, 2016.

[75] F. Sacco, B. Paun, O. Lehmkuhl, T. L. Iles and P. A. Iaizzo, 'Left Ventricular Trabeculations Decrease the Wall Shear Stress and Increase the Intra-Ventricular Pressure Drop in CFD Simulations', *frontiers in Physiology*, vol. 9, no. April, p. 458, 2018.

[76] J. Lantz, L. Henriksson and A. Persson, 'Patient-Specific Simulation of Cardiac Blood Flow From High- Resolution Computed Tomography', *Journal of Biomechanical Engineering*, vol. 138, pp. 1–9, 2018.

[77] T. B. Le and F. Sotiropoulos, 'On the three-dimensional vortical structure of early diastolic flow in a patient-specific left ventricle', *European Journal of Mechanics, B/Fluids*, vol. 35, pp. 20–24, 2012.

[78] S. S. Khalafvand, L. Zhong and E. Y. Ng, 'Three-dimensional CFD/MRI modeling reveals that ventricular surgical restoration improves ventricular function by modifying intraventricular blood flow', *International Journal for Numerical Methods in Biomedical Engineering*, vol. 30, no. 10, pp. 1044–1056, 2014.

[79] C. Corsini, C. Baker, E. Kung, S. Schievano, G. Arbia, A. Baretta, G. Biglino, F. Migliavacca, G. Dubini, G. Pennati, A. Marsden, I. Vignon-Clementel, A. Taylor, T.-Y. Hsia and A. Dorfman, 'An integrated approach to patient-specific predictive modeling for single ventricle heart palliation', *Computer Methods in Biomechanics and Biomedical Engineering*, vol. 17, no. 14, pp. 1572–1589, 2014.

[80] M. Nakamura, S. Wada and T. Yamaguchi, 'Computational Analysis of Blood Flow in an Integrated Model of the Left Ventricle and the Aorta', *Journal of Biomechanical Engineering*, vol. 128, no. 6, pp. 837–843, 2006.

[81] M. S. Arefin and Y. S. Morsi, 'Fluid structure interaction (FSI) simulation of the left ventricle (LV) during the early filling wave (E-wave), diastasis and atrial contraction wave (A-wave)', *Australasian Physical & Engineering Sciences in Medicine*, vol. 37, no. 2, pp. 413–423, 2014.

[82] J. A. Vierendeels, K. Riemslagh, E. Dick and P. R. Verdonck, 'Computer simulation of intraventricular flow and pressure gradients during diastole', *Journal of biomechanical engineering*, vol. 122, no. 6, pp. 667–674, 2000.

[83] J. A. Vierendeels, E. Dick and P. R. Verdonck, 'Hydrodynamics of color M-mode Doppler flow wave propagation velocity V(p): A computer study', *Journal of the American Society of Echocardiography*, vol. 15, no. 3, pp. 219–224, 2002.

[84] X. Wang, V. Mihalef, Z. Qian, S. Voros and M. Dimitris, '3D Cardiac Motion Reconstruction from CT Data and Tagged MRI', *Conf Proc IEEE Eng Med Biol Soc*, vol. 19, no. 1, pp. 69–77, 2016.

[85] O. Skrinjar and A. Bistoquet, 'Generation of myocardial wall surface meshes from segmented MRI', *International Journal of Biomedical Imaging*, vol. 2009, 2009.

[86] M. Gao, J. Huang, S. Zhang, Z. Qian, S. Voros, D. Metaxas and L. Axel, '4D Cardiac Reconstruction Using High Resolution CT Images', in *Functional Imaging and Modeling of Heart*, 2011, pp. 153–160.

[87] W. Sun, M. Qetin, R. Chan, V. Reddy, G. Holmvang, V. Chandar and a. Willsky, 'Segmenting and tracking the left ventricle by learning the dynamics in cardiac images.' In *Information processing in medical imaging : proceedings of the ... conference*, Lv, G. E. Christensen and M. Sonka, Eds., vol. 19, Berlin, Heidelberg: Springer Berlin Heidelberg, 2005, pp. 553–65.

[88] Y. Zhu, X. Papademetris, A. J. Sinusas and J. S. Duncan, 'Segmentation of the left ventricle from cardiac MR images using a subject-specific dynamical model', *IEEE Transactions on Medical Imaging*, vol. 29, no. 3, pp. 669–687, 2010.

[89] A. Besbes, N. Komodakis and N. Paragios, 'Graph-based knowledge-driven discrete segmentation of the left ventricle', *Proceedings - 2009 IEEE International Symposium on Biomedical Imaging: From Nano to Macro, ISBI 2009*, no. 3, pp. 49–52, 2009.

[90] V. Mihalef, R. I. Ionasec, P. Sharma and D. Comaniciu, 'Patient-specific modelling of whole heart anatomy , dynamics and haemodynamics from four-dimensional cardiac CT images', *Interface Focus*, vol. 1, pp. 286–296, 2011.

[91] T. Schenkel, M. Malve, M. Reik, M. Markl, B. Jung and H. Oertel, 'MRI-Based CFD analysis of flow in a human left ventricle: Methodology and application to a healthy heart', *Annals of Biomedical Engineering*, vol. 37, no. 3, pp. 503–515, 2009.

[92] T. Doenst, K. Spiegel, M. Reik, M. Markl, J. Hennig, S. Nitzsche, F. Beyersdorf and H. Oertel, 'Fluid-Dynamic Modeling of the Human Left Ventricle: Methodology and Application to Surgical Ventricular Reconstruction', *Annals of Thoracic Surgery*, vol. 87, no. 4, pp. 1187–1195, 2009.

[93] C. W. Lim, Y. Su, S. Y. Yeo, G. M. Ng, V. T. Nguyen, L. Zhong, R. S. Tan, K. K. Poh and P. Chai, '4D Model Reconstruction of Patient-Specific Cardiac Mesh from Segmented Contour Lines', *APCOM & ISCM*, pp. 1–8, 2013.

[94] ——, 'Automatic 4D reconstruction of patient-specific cardiac mesh with 1-to-1 vertex correspondence from segmented contours lines', *PLoS ONE*, vol. 9, no. 4, 2014.

[95] M. Selmi, W.-c. Chiu, V. K. Chivukula, G. Melisurgo, J. A. Beckman, C. Mahr, A. Aliseda, E. Votta, A. Redaelli, M. J. Slepian, D. Bluestein, F. Pappalardo and F. Consolo, 'Blood damage in Left Ventricular Assist Devices : Pump thrombosis or system thrombosis ?', *The International Journal of Artificial Organs*, vol. 1, no. 12, 2018.

[96] V. Vasudevan, H. Wiputra and C. H. Yap, 'Torsional motion of the left ventricle does not affect ventricular fluid dynamics of both foetal and adult hearts', *Journal of Biomechanics*, vol. 96, p. 109 357, 2019.

[97] Q. Long, R. Merrifield, X. Y. Xu, P. Kilner, D. N. Firmin and G. Z. Yang, 'Subject-specific computational simulation of left ventricular flow based on magnetic resonance imaging', *Proceedings of the Institution of Mechanical Engineers, Part H: Journal of Engineering in Medicine*, vol. 222, no. 4, pp. 475–485, 2008.

[98] H. Watanabe, S. Sugiura and T. Hisada, 'The looped heart does not save energy by maintaining the momentum of blood flowing in the ventricle', *American Journal of Physiology - Heart and Circulatory Physiology*, vol. 294, no. 5, pp. 2191–2196, 2008.

[99] S. Krittian, U. Janoske, H. Oertel and T. Böhlke, 'Partitioned Fluid–Solid Coupling for Cardiovascular Blood Flow', *Annals of Biomedical Engineering*, vol. 38, no. 4, pp. 1426–1441, 2010.

[100] J. H. Seo and R. Mittal, 'Effect of diastolic flow patterns on the function of the left ventricle', *Physics of Fluids*, vol. 25, no. 11, p. 110 801, 2013.

[101] N. Ranganathan, J. H. Lam, E. D. Wigle and M. D. Silver, 'Morphology of the human mitral valve. II. The value leaflets.' *Circulation*, vol. 41, no. 3, pp. 459–467, 1970.

[102] S. N. Doost, L. Zhong, B. Su and Y. S. Morsi, 'The numerical analysis of non-Newtonian blood flow in human patient-specific left ventricle', *Computer Methods and Programs in Biomedicine*, vol. 127, pp. 232–247, 2016.

[103] A. M. Pouch, H. Wang, M. Takabe, B. M. Jackson, J. H. Gorman, R. C. Gorman, P. A. Yushkevich and C. M. Sehgal, 'Fully automatic segmentation of the mitral leaflets in 3D transesophageal echocardiographic images using multi-atlas joint label fusion and deformable medial modeling', *Medical Image Analysis*, vol. 18, no. 1, pp. 118–129, 2014.

[104] World Health Organization, 'Media Centre: Cardiovascular disease', *Who*, vol. 08, pp. 1–6, 2015.

[105] M. Nichols, N. Townsend, R. Luengo-Fernandez, J. Leal, A. Gray, P. Scarborough and M. Rayner, 'European cardiovascular disease statistics 2012', *European Heart Journal*, p. 129, 2012.

[106] E. Oost, P. Oemrawsingh, J. H. Reiber and B. Lelieveldt, 'Automated left ventricular delineation in x-ray angiograms: A validation study', *Catheterization and Cardiovascular Interventions*, vol. 73, no. 2, pp. 231–240, 2009.

[107] P. S. Douglas, B. De Bruyne, G. Pontone, M. R. Patel, B. L. Norgaard, R. A. Byrne, N. Curzen, I. Purcell, M. Gutberlet, G. Rioufol, U. Hink, H. W. Schuchlenz, G. Feuchtner, M. Gilard, D. Andreini, J. M. Jensen, M. Hadamitzky, K. Chiswell, D. Cyr, A. Wilk, F. Wang, C. Rogers and M. A. Hlatky, '1-Year Outcomes of FFRCT-Guided Care in Patients With Suspected Coronary Disease: The PLATFORM Study', *Journal of the American College of Cardiology*, vol. 68, no. 5, pp. 435–445, 2016.

[108] W. R. Henderson, Y. Molgat-Seon, W. Vos, R. Lipson, F. Ferreira, M. Kirby, C. V. Holsbeke, P. B. Dominelli, D. E. G. Griesdale, M. Sekhon, H. O. Coxson, J. Mayo and A. W. Sheel, 'Functional respiratory imaging, regional strain, and expiratory time constants at three levels of positive end expiratory pressure in an ex vivo pig model.' *Physiological reports*, vol. 4, no. 23, P1, 2016.

[109] C. Schultz, R. Rodriguez-Olivares, J. Bosmans, T. Lefvre, G. De Santis, N. Bruining, V. Collas, T. Dezutter, B. Bosmans, Z. Rahhab, N. El Faquir, Y. Watanabe, P. Segers, B. Verhegghe, B. Chevalier, N. Van Mieghem, M. De Beule, P. Mortier and P. De Jaegere, 'Patient-specific image-based computer simulation for the prediction of valve morphology and calcium displacement after TAVI with the Medtronic CoreValve and the Edwards SAPIEN valve', *EuroIntervention*, vol. 11, no. 9, pp. 1044–1052, 2016.

[110] B. Baillargeon, N. Rebelo, D. D. Fox, R. L. Taylor and E. Kuhl, 'The living heart project: A robust and integrative simulator for human heart function', *European Journal of Mechanics, A/Solids*, vol. 48, no. 1, pp. 38–47, 2014.

[111] G. De Santis, M. De Beule, K. Van Canneyt, P. Segers, P. Verdonck and B. Verhegghe, 'Full-hexahedral structured meshing for image-based computational vascular modeling', *Medical Engineering and Physics*, vol. 33, no. 10, pp. 1318–1325, 2011.

[112] G. De Santis, P. Mortier, M. De Beule, P. Segers, P. Verdonck and B. Verhegghe, 'Patient-specific Computational Fluid Dynamics: Structured mesh generation from coronary angiography', *Medical and Biological Engineering and Computing*, vol. 48, no. 4, pp. 371–380, 2010.

[113] G. De Santis, M. De Beule, P. Segers, P. Verdonck and B. Verhegghe, 'Patient-specific computational haemodynamics: generation of structured and conformal hexahedral meshes from triangulated surfaces of vascular bifurcations.' *Computer methods in biomechanics and biomedical engineering*, vol. 14, no. 9, pp. 797–802, 2011.

[114] P. Peng, K. Lekadir, A. Gooya, L. Shao, S. E. Petersen and A. F. Frangi, 'A review of heart chamber segmentation for structural and functional analysis using cardiac magnetic resonance imaging', *Magnetic Resonance Materials in Physics, Biology and Medicine*, vol. 29, no. 2, pp. 155–195, 2016.

[115] Y. Ishida, J. S. Meisner, T. Katsuhiko, J. I. Gallo, C. Yoran, R. W. M. Frater and E. L. Yellin, 'Left ventricular filling dynamics : influence of left ventricular relaxation and left atrial pressure', *Circulation*, vol. 74, no. 1, pp. 187–196, 1986.

[116] M. Courtois, S. J. K. Jr and P. A. Ludbrook, 'Transmitral Pressure-Flow Velocity Relation Importance of Regional Pressure Gradients in the Left Ventricle During Diastole', *Circulation*, vol. 78, no. 3, pp. 661–671, 1988.

[117] C. Chnafa, S. Mendez and F. Nicoud, 'Image-Based Simulations Show Important Flow Fluctuations in a Normal Left Ventricle: What Could be the Implications?', *Annals of Biomedical Engineering*, vol. 44, no. 11, pp. 1–13, 2016.

[118] J. V. Cauwenberge, S. Member, L. Lovstakken, S. Fadnes, A. Member, A. Rodriguez-morales, J. Vierendeels, P. Segers and A. Swillens, 'Assessing the Performance of Ultrafast Vector Flow Imaging in the Neonatal Heart via Multiphysics Modeling and In Vitro Experiments', *IEEE Trasnsaction on Ultrasonics, ferroelectrics, and frequency control*, vol. 63, no. 11, pp. 1772–1785, 2016.

[119] S. Kulp, M. Gao, S. Zhang, Z. Qian, S. Voros, D. Metaxas and L. Axel, 'Using High Resolution Cardiac CT Data to Model and Visualize Patient-Specific Interactions between Trabeculae and Blood Flow', in *Medical Image Computing and Computer-Assisted Intervention – MICCAI 2011*, G. Fichtinger, A. Martel and T. Peters, Eds., Berlin, Heidelberg: Springer Berlin Heidelberg, 2011, pp. 468–475.

[120] E. Kung, A. Baretta, C. Baker, G. Arbia, G. Biglino, C. Corsini, S. Schievano, I. E. Vignon-clementel, G. Dubini, G. Pennati, A. Taylor, A. Dorfman, A. M. Hlavacek, A. L. Marsden, T.-y. Hsia and F. Migliavacca, 'Predictive modeling of the virtual Hemi-Fontan operation for second stage single ventricle palliation : Two patient-specific cases', *Journal of Biomechanics*, vol. 46, no. 2, pp. 423–429, 2013.

[121] S. Hendabadi, R. Yotti, J. C. D. Alamo, S. Diego and S. C. Shadden, 'Topology of Blood Transport in the Human Left Ventricle by Novel Processing of Doppler Echocardiography Topology of Blood Transport in the Human Left Ventricle by Novel Processing of Doppler Echocardiography', *Annals of Biomedical Engineering*, vol. 41, no. 12, 2013.

[122] J. O. Mangual, E. Kraigher-krainer, A. D. Luca, L. Toncelli, A. Shah, S. Solomon, G. Galanti, F. Domenichini and G. Pedrizzetti, 'Comparative numerical study on left ventricular fl uid dynamics after dilated cardiomyopathy', *Journal of Biomechanics*, vol. 46, no. 10, pp. 1611–1617, 2013.

[123] B. Su, L. Zhong, X. K. Wang, J. M. Zhang, R. S. Tan, J. C. Allen, S. K. Tan, S. Kim and H. L. Leo, 'Numerical simulation of patient-specific left ventricular model with both mitral and aortic valves by FSI approach', *Computer Methods and Programs in Biomedicine*, vol. 113, no. 2, pp. 474–482, 2014.

[124] L. Lee and R. LeVeque, 'An Immersed Interface Method for Incompressible Navier-Stokes Equations', *SIAM Journal on Scientific Computing*, vol. 25, no. 3, pp. 832–856, 2003.

[125] E. A. Fadlun, R. Verzicco and P. Orlandi, 'Combined Immersed-Boundary Finite-Difference Methods for Three-Dimensional Complex Flow Simulations', *Journal of Computational Physics*, vol. 161, no. 1, pp. 35–60, 2000.

[126] R. Aarnes, T. Jin, C. Mao, N. E. L. Haugen, K. Luo and H. I. Andersson, 'Treatment of solid objects in the Pencil Code using an immersed boundary method and overset grids', *Geophysical & Astrophysical Fluid Dynamics*,

[127] A. A. Young and B. R. Cowan, 'Evaluation of left ventricular torsion by cardiovascular magnetic resonance', *Journal of Cardiovascular Magnetic Resonance*, pp. 1–10, 2012.

[128] A. A. Phillips, A. T. Cote, S. S. D. Bredin and D. E. R. Warburton, 'Heart disease and left ventricular rotation – a systematic review and quantitative summary', *BioMed Central Cardiovascular Disorders*, vol. 12, no. 46, 2012.

[129] L. Axel, A. Montillo and D. Kim, 'Tagged magnetic resonance imaging of the heart: A survey', *Medical Image Analysis*, vol. 9, no. 4 SPEC. ISS. Pp. 376–393, 2005.

[130] F. Canè, B. Verhegghe, M. De Beule, P. B. Bertrand, R. J. Van Der Geest, P. Segers and G. De Santis, 'From 4D Medical Images (CT, MRI, and Ultrasound) to 4D Structured Mesh Models of the Left Ventricular Endocardium for Patient-Specific Simulations', *BioMed Research International*, vol. 2018, 2018.

[131] M. G. Al-azawy, A. Turan and A. Revell, 'An Overset Mesh Approach for Valve Closure : An LVAD Application', *Proceedings of the 9th International Joint Conference on Biomedical Engineering Systems and Technologies (BIOSTEC 2016)*, vol. 1, no. Biostec, pp. 145–151, 2016.

[132] A. J. Barker, P. V. Ooij, K. Bandi, J. Garcia, M. Albaghdadi, P. Mccarthy, R. O. Bonow, J. Carr, J. Collins, S. C. Malaisrie and M. Markl, 'Viscous Energy Loss in the Presence of Abnormal Aortic Flow', *Magnetic Resonance in Medicine*, vol. 00, pp. 1–9, 2013.

[133] X. Zheng, J. H. Seo, V. Vedula, T. Abraham and R. Mittal, 'European Journal of Mechanics B / Fluids Computational modeling and analysis of intracardiac flows in simple models of the left ventricle', *European Journal of Mechanics B/Fluids*, vol. 35, pp. 31–39, 2012.

[134] P. D. Morris, A. Narracott, H. Von Tengg-Kobligk, D. A. S. Soto, S. Hsiao, A. Lungu, P. Evans, N. W. Bressloff, P. V. Lawford, D. Rodney Hose and J. P. Gunn, 'Computational fluid dynamics modelling in cardiovascular medicine', *Heart*, vol. 102, no. 1, pp. 18–28, 2016.

[135] F. Domenichini and G. Pedrizzetti, 'Asymptotic Model of Fluid–Tissue Interaction for Mitral Valve Dynamics', *Cardiovascular Engineering and Technology*, vol. 6, no. 2, pp. 95–104, 2015.

[136] H. Watanabe, S. Sugiura, H. Kafuku and T. Hisada, 'Multiphysics Simulation of Left Ventricular Filling Dynamics Using Fluid-Structure Interaction Finite Element Method', *Biophysical Journal*, vol. 87, no. 3, pp. 2074–2085, 2004.

[137] R. Rehman, V. S. Yelamanchili and A. N. Makaryus, 'Cardiac Imaging.' eng, in, 2020.

[138] V. M. Stoll, M. Loudon, J. Eriksson, M. M. Bissell, P. Dyverfeldt, T. Ebbers, S. G. Myerson, S. Neubauer, C. J. Carlhäll and A. T. Hess, 'Test-retest variability of left ventricular 4D flow cardiovascular magnetic resonance measurements in healthy subjects', *Journal of Cardiovascular Magnetic Resonance*, vol. 20, no. 1, pp. 1–10, 2018.

[139] X. Ma, H. Gao, B. E. Griffith, C. Berry and X. Luo, 'Image-based fluid-structure interaction model of the human mitral valve', *Computers and Fluids*, vol. 71, pp. 417–425, 2013.

[140] V. Govindarajan, J. Mousel, H. S. Udaykumar, S. C. Vigmostad, D. D. McPherson, H. Kim and K. B. Chandran, 'Synergy between Diastolic Mitral Valve Function and Left Ventricular Flow AIDS in Valve Closure and Blood Transport during Systole', *Scientific Reports*, vol. 8, no. 1, pp. 1–14, 2018.

[141] H. Gao, L. Feng, N. Qi, C. Berry, B. E. Griffith and X. Luo, 'A coupled mitral valve — left ventricle model with fluid – structure interaction', *Medical Engineering and Physics*, vol. 47, pp. 128–136, 2017.

[142] A. Caballero, R. McKay and W. Sun, 'Computer simulations of transapical mitral valve repair with neochordae implantation: Clinical implications', *JTCVS Open*, vol. 3, no. C, pp. 27–44, 2020.

[143] A. Caballero, W. Mao, R. McKay and W. Sun, 'Transapical mitral valve repair with neochordae implantation: FSI analysis of neochordae number and complexity of leaflet prolapse', *International Journal for Numerical Methods in Biomedical Engineering*, vol. 36, no. 3, pp. 1–16, 2020.

[144] B. Biffi, M. Gritti, A. Grasso, E. G. Milano, M. Fontana, H. Alkareef, J. Davar, P. Jeetley, C. Whelan, S. Anderson, D. Lorusso, E. Sauvage, G. Maria, S. Schievano and C. Capelli, 'A workflow for patient-specific fluid – structure interaction analysis of the mitral valve : A proof of concept on a mitral regurgitation case', no. xxxx, 2019.

[145] W. Mao, A. Caballero, R. McKay, C. Primiano and W. Sun, 'Fully-coupled fluid-structure interaction simulation of the aortic and mitral valves in a realistic 3D left ventricle model', *PLoS ONE*, vol. 12, no. 9, 2017.

[146] S. F. Stewart, P. Hariharan, E. G. Paterson, G. W. Burgreen, V. Reddy, S. W. Day, M. Giarra, K. B. Manning, S. Deutsch, M. R. Berman, M. R. Myers and R. A. Malinauskas, 'Results of FDA's First Interlaboratory Computational Study of a Nozzle with a Sudden Contraction and Conical Diffuser', *Cardiovascular Engineering and Technology*, vol. 4, no. 4, pp. 374–391, 2013.

[147] R. A. Malinauskas, P. Hariharan, S. W. Day, L. H. Herbertson, M. Buesen, U. Steinseifer, K. I. Aycock, B. C. Good, S. Deutsch, K. B. Manning and B. A. Craven, 'FDA Benchmark Medical Device Flow Models for CFD Validation', 2. 2017, vol. 63, pp. 150–160.

[148] K. S. Kunzelman, R. P. Cochran, E. D. Verrier and R. C. Eberhart, 'Anatomic basis for mitral valve modelling', *Journal of Heart Valve Disease*, vol. 3, no. 5, pp. 491–496, 1994.

[149] V. Vasudevan, A. J. J. Low, S. P. Annamalai, S. Sampath, C. L. Chin, A. A. B. Ali and C. H. Yap, 'Role of diastolic vortices in flow and energy dynamics during systolic ejection', *Journal of Biomechanics*, vol. 90, pp. 50–57, 2019.

[150] C. Chen, C. Qin, H. Qiu, G. Tarroni, J. Duan, W. Bai and D. Rueckert, 'Deep learning for cardiac image segmentation: A review', *Frontiers in cardiovscaular medicine*, vol. 7, no. March, 2019.

[151] F. Kong and S. C. Shadden, 'Automating Model Generation for Imagebased Cardiac Flow Simulation.' eng, *Journal of biomechanical engineering*, 2020.

[152] L. Delcour, J. Peeters and J. Degroote, 'Three-dimensional fluid-structure interaction simulations of a yarn subjected to the main nozzle flow of an air-jet weaving loom using a Chimera technique', 2. 2020, vol. 90, pp. 194–212.